Title
Spatio-Temporal Reconstruction Techniques for Optical Microscopy

Permalink
https://escholarship.org/uc/item/6nt319nb

Author
Chacko, Nikhil

Publication Date
2015

Peer reviewed|Thesis/dissertation

University of California
Santa Barbara

Spatio-Temporal Reconstruction Techniques for Optical Microscopy

A dissertation submitted in partial satisfaction
of the requirements for the degree

Doctor of Philosophy

in

Electrical and Computer Engineering

by

Nikhil Chacko

Committee in charge:

       Professor Michael Liebling, Chair
       Professor Shivkumar Chandrasekaran
       Professor Jerry D. Gibson
       Professor Bangalore S. Manjunath

December 2015

The Dissertation of Nikhil Chacko is approved.

_____

Professor Shivkumar Chandrasekaran

_____

Professor Jerry D. Gibson

_____

Professor Bangalore S. Manjunath

_____

Professor Michael Liebling, Committee Chair

September 2015

Spatio-Temporal Reconstruction Techniques for Optical Microscopy

To my nieces, Elleese and Rebekah.

Acknowledgements

Neither this thesis nor the past five years in graduate school would have been possible if it were not for the help and support of many others.

I'm indebted to my graduate advisor, Prof. Michael Liebling, for having given me the opportunity to work in Systems Bioimaging Lab (SYBIL) at University of California, Santa Barbara (UCSB) and for having proposed this subject to me. He has had a profound influence in shaping my outlook towards research, programming, teaching, and writing. Among everything, I'm unequivocally most grateful for his timely guidance and kind words of encouragement, which were sometimes all that kept me going.

I express my sincere gratitude to Prof. Shivkumar Chandrasekaran, Prof. Jerry D. Gibson, and Prof. Bangalore S. Manjunath for having kindly agreed to be on my thesis committee. Their classes have been among the best learning experiences I've had as a graduate student and have greatly facilitated my research interests in signal processing.

My deep appreciation goes out to Prof. Hua Lee for the comforting presence he has been over the years I've served as a teaching assistant at UCSB. Special thanks are also due to the enthusiastic students whom I've had the fortune to know through these classes.

I thank Prof. Thierry Blu at The Chinese University of Hong Kong, Dr. Julien Vermot, Dr. Emily Steed, and Dr. Francesco Boselli at Institut de Génétique et de Biologie Moléculaire et Cellulaire, and Dr. Sebastian Streichan at The Kavli Institute of Theoretical Physics, UCSB, for all the insightful discussions shared during our collaborations.

I gratefully acknowledge the kind assistance of Dmitry Federov and Kristian Kvilekval at the Center of Bio-Image Informatics, UCSB, during the development of image processing tools for Bio-Image Semantic Query User Environment (Bisque).

I thank the image processing group at Karl Storz Imaging, Inc., especially Bryan Kennedy, Gaurav Sharma, Kamal Agarwal, and Jonathan Bormet, for their warm sup-

Department of Electrical & Computer Engineering
University of California, Santa Barbara
Santa Barbara, CA 93106-9560, USA
℘ *+1 (805) 455 2850*
✉ *nchacko@ece.ucsb.edu*
Last updated: September 2, 2015

Nikhil Chacko

Education

2012–15 **Doctor of Philosophy in Electrical & Computer Engineering**.
University of California, Santa Barbara (USA)
- Thesis: Spatio-temporal reconstruction techniques for optical microscopy
- Thesis Advisor: Prof. Michael Liebling
- Thesis Committee: Prof. S. Chandrasekaran, Prof. J. Gibson, Prof. B. S. Manjunath
- GPA: 3.97/4.00

2010–12 **Master of Science in Electrical & Computer Engineering**.
University of California, Santa Barbara (USA)
- Major: Signal Processing, Minor: Communication
- Course Projects: Face recognition via sparse representation (image processing), Hand tracking and gesture recognition for system interface (computer vision), Speaker recognition and verification (speech processing)
- GPA: 3.97/4.00

2006–10 **Bachelor of Technology in Electronics & Communication Engineering**.
National Institute of Technology, Calicut (India)
- Degree Project: Fingerprint recognition and authentication system on a BeagleBoard
- GPA: 9.13/10.00 (Distinction)

Experience

Research/Internship

2011–15 **Graduate Student Research**, *Systems Bioimaging Lab, UC Santa Barbara*.
- Designed a fast and non-redundant temporal registration algorithm for the synchronization of quasi-periodic time sequences, as in cardiac and pulmonary imaging, using wavelet analysis and dynamic programming[1,2].
- Designed a pyramid-based spatial registration algorithm for aligning anisotropically blurred volumetric datasets related via a rigid-body transform[3]. This is instrumental for multi-view spatial registration, fusion, and deconvolution in optical microscopy.
- Designed a sparsity-based iterative-shrinkage-thresholding shift-variant 3D deconvolution method that uses depth-dependent point-spread-functions[4]. This is to mitigate spherical aberrations that arise while imaging thick samples in optical microscopy.
- Designed an algorithm for the accurate discretization of continuous convolution operators, based on generalized sampling theory and demonstrated its use for modeling wave propagation as defined in scalar diffraction theory[5].
- Designed a fast and sparsity-based iterative-shrinkage-thresholding algorithm for deconvolving 3D microscopic volumes acquired from mutually tilted multiple views obtained by rotating the sample about a lateral axis orthogonal to the optical axis[6]. This is to mitigate the axial blur present in each of the acquired multi-view volumes by leveraging information from other views.
- Jointly developed an HDR technique for fluorescence microscopy to fuse movies depicting a repeating biological process acquired at different illumination settings[7].

Summer, **Image Processing Engineer Intern**, *Karl Storz Imaging, CA*.
2011
- Assisted in measurement, design, simulation, and testing of image processing routines for camera processors, video display, and image compression.
- Designed test procedures and fixtures for color correction in endoscopic equipments.
- Provided support for imaging systems to product development teams.

Teaching (UC Santa Barbara)

Spring, **Teaching Assistant**, ECE 148, *Applications of Signal Analysis and Processing*,
2015 Prof. H. Lee.
Engineering applications of signal analysis and processing techniques in communications, image processing, analog and digital filter design, signal detection and parameter estimation, holography and tomography, Fourier optics, microwave, and acoustic sensing.

Winter, **Teaching Assistant**, ECE 130B, *Signal Analysis and Processing*,
2015 Prof. H. Lee.
Sampling theory, discrete time systems, convolution, z-transform, and Fourier analysis.

Fall, **Teaching Assistant**, ECE 178, *Introduction to Image and Video Processing*,
2014 Prof. M. Liebling.
Image formation and sampling, image transforms, image enhancement, interpolation, multi-variate gradients, morphological operations, tomography, color processing and correction, and image compression using JPEG and MPEG coding standards.

Winter, **Teaching Assistant**, ECE 148, *Applications of Signal Analysis and Processing*,
2014 Prof. H. Lee.
Similar topics as in Spring, 2015.

Fall, **Teaching Assistant**, ECE 178, *Introduction to Image and Video Processing*,
2013 Prof. M. Liebling.
Similar topics as in Fall, 2014.

Summer, **Research Mentor**, *Internships in Nanosystems Science, Engineering, and Technology* (INSET), Center for Science and Engineering Partnerships, UCSB.
2013
Organized a summer research project, designed for undergraduate students, about point-spread-function analysis and their significance in deconvolution.

Spring, **Teaching Assistant**, ECE 148, *Applications of Signal Analysis and Processing*,
2013 Prof. H. Lee.
Similar topics as in Spring, 2015.

Spring, **Reader**, ECE 258B, *Multi-rate Digital Signal Processing*,
2012 Prof. M. Liebling.
Multi-rate digital filter theory, polyphase decomposition, decimator and interpolator design, efficient filter implementations, orthogonal transforms, wavelet transforms, analysis and synthesis filter banks, quadrature mirror filter banks, transmultiplexers, and sub-band decompositions.

Computer Skills

OS Windows, Mac OS, Linux

Prog. Matlab, C, C++, Java, VHDL

Publish LaTeX, HTML, Adobe After Effects, Illustrator

Software ImageJ, Bitplane Imaris, Mathematica, SVN

Publications

1. **N. Chacko**, K. Chan, S. Bhat, J. Ohn, M. Liebling, "Quasi-periodic dynamic time warping for temporal registration of cardiac signals," IEEE Transactions on Medical Imaging (submitted).
2. C. Ramspacher, E. Steed, F. Boselli, R. Ferreira, N. Faggianelli, S. Roth, C. Spiegelhalter, N. Messaddeq, L. Trinh, M. Liebling, **N. Chacko**, F. Tessadori, J. Bakkers, J. Laporte, K. Hnia, J. Vermot, "Developmental alterations in heart biomechanics and skeletal muscle function in desmin mutants suggest an early pathological root for desminopathies," Cell Reports, Vol. 11, Iss. 10, pp. 1564–1576, June 2015.
3. **N. Chacko**, K. Chan, M. Liebling, "Intensity-based point-spread-function-aware registration for multi-view applications in optical microscopy," Proceedings of the IEEE International Symposium on Biomedical Imaging (ISBI), New York, April 16–19, 2015.
4. **N. Chacko**, M. Liebling, "Fast spatially-variant deconvolution for optical microscopy via iterative shrinkage thresholding," Proceedings of the IEEE International Conference on Acoustics, Speech, and Signal Processing (ICASSP), Florence, Italy, May 4–9, 2014.
5. **N. Chacko**, M. Liebling, T. Blu, "Discretization of continuous convolution operators for accurate modeling of wave propagation in digital holography," Journal of the Optical Society of America A, vol. 30, no. 10, October 2013.
6. **N. Chacko**, M. Liebling, "Fast thresholded multi-channel Landweber algorithm for wavelet-regularized multi-angle deconvolution," Proceedings of the SPIE Conference Optics & Photonics: Wavelets and Sparsity XV, San Diego CA, USA, August 26–29, 2013, vol. 8858.
7. K. Chan*, **N. Chacko***, M. Liebling, "A method for high dynamic range (HDR) fluorescence video microscopy for repeating processes" (to be submitted) (*equally contributing authors).

Professional Societies

IEEE Signal Processing Society (Member and Peer-Reviewer), IEEE Young Professionals

Honors and Awards

- **Best Student Paper** [2015], sponsored by Amazon and IEEE Journal of Biomedical and Health Informatics (JBHI) at IEEE International Symposium on Biomedical Imaging, 2015.
- **ECE Outstanding Teaching Assistant** [2015], awarded by the Department of Electrical and Computer Engineering (ECE), UCSB.
- **Travel Grant Based On Peer-Review Scores** [2015], awarded by National Institutes of Health (NIH), U.S. Department of Health & Human Services.
- **Doctoral Student Travel Grant** [2015], awarded by Academic Senate, UCSB.
- **Dissertation Fellowship** [2014], awarded by ECE, UCSB.
- **(Nominated) Excellence in Teaching** [2013-14], Graduate Students Association, UCSB.

Abstract

Spatio-Temporal Reconstruction Techniques for Optical Microscopy

by

Nikhil Chacko

Optical microscopy offers the unique possibility to study living samples under conditions akin to their native state. However, the technique is not void of inherent problems such as optical blur due to light diffraction, contamination with out-of-focus light from adjacent focal planes, and spherical aberrations. Furthermore, with a dearth of techniques that are capable of imaging multiple focal sections in quick succession, the multi-dimensional capture of dynamically changing samples remains a challenge of its own. Computational techniques that use auxiliary knowledge about the imaging system and the sample to mitigate these problems are hence of great interest in optical microscopy.

The first part of this thesis deals with the design of a discrete model to characterize light propagation. Following the scalar diffraction theory in optics, we propose a discrete algorithm, based on generalized sampling theory, to reverse the coherent diffraction process via back propagation. The algorithm consists of a wavelet-based model for the spherical waves emanating from the object of interest and an optimized multi-rate filtering protocol for reconstruction from the diffraction data recorded by non-ideal detectors.

The second part of this thesis describes a spatial registration tool designed for multi-view microscopy. Here, the imaged sample is rotated about a lateral axis for the acquisition of multiple 3D datasets from different views in order to subsequently alleviate the severe axial blur found in each such dataset. Automatic algorithms that only rely on maximizing pixel-based similarity provide poor results in such applications owing to the anisotropic point-spread-function (PSF) of optical microscopes. We propose a

pyramid-based spatial registration algorithm that re-blurs the multi-view datasets with transformed forms of the PSF in order to make them comparable, before maximizing their pixel-based similarity for registration.

The third part of this thesis describes a fast converging iterative multi-view deconvolution technique that can be applied to the spatially registered forms of the 3D datasets acquired using multi-view microscopy. Our sparsity based algorithm solves a non-linear objective function to jointly deconvolve and fuse the multi-view datasets to finally produce a single deblurred 3D result that has nearly isotropic spatial resolution.

The fourth part of this thesis addresses problems due to spherical aberrations encountered during the imaging of thick samples in optical microscopy. The depth-varying nature of the optical blur found in such cases renders fast and efficient shift-invariant deconvolution techniques to be inapplicable. Here, we propose a fast iterative-shrinkage-thresholding shift-variant 3D deconvolution method that uses depth-dependent PSFs to reconstruct a 3D deblurred form of the imaged thick specimen.

The final part of this thesis describes a non-rigid temporal registration tool that aids in the multi-dimensional imaging of quasi-periodic processes such as cardiac cycles. We propose a variant of dynamic time warping that is capable of both temporally warping and wrapping an input sequence by allowing for jump discontinuities in the non-linear temporal alignment function akin to those found in wrapped phase functions.

This work provides a new set of tools for spatio-temporal reconstruction in optical microscopy and we anticipate them to be useful for a wide range of problems in practice.

Contents

List of Figures

List of Tables

Chapter 1

Introduction

Optical microscopy offers the unique possibility to analyze living samples under conditions akin to their native state. The advent of natural fluorescent probes such as the green fluorescent protein (GFP) [20] has further led to the widespread use of fluorescence microscopy [61, 113] for the analysis of specific living cells and tissues. A number of innovations from the fields of physics, optics, as well as genetic, mechanical, and electrical engineering have been combined to enter this new era of biological imaging. Though optical microscopy has historically been an observational technique, the development of digital sensing technologies has led to a parallel surge in the use of digital signal and image processing to model and analyze the data made available through these systems.

1.1   Motivation

Even an ideal aberration-free objective in an optical microscope produces a distorted image of the object due to optical blur, which is a consequence of light diffraction through the optical system, resulting in limited spatial resolution. This limitation is inherent to any optical system and can be described using the wave-like nature of light. According

to the Huygens-Fresnel principle [11], the spherical wave emanating from a point source in the object plane consists of a multitude of other spherical waves. All such waves from the same wave front have the same phase origin and interfere together in the image plane, resulting in a diffraction pattern known as the Airy pattern, consisting of a series of concentric spheres. Furthermore, these spherical waves interfere not only in the image plane, but also throughout the 3D space. This is apparent during optical sectioning, where images are sequentially recorded while the focal plane is varied through the sample, with each focal plane getting inadvertently contaminated with out-of-focus information from the adjacent planes above and below that examined. Consequently, the image of a point source located in the object plane is a three-dimensional diffraction pattern, centered on the conjugate image of the point source located in the image plane. The ensemble of such individual diffraction patterns emanating from different point sources in the object plane finally constitutes the impulse response of the device and the image observed through the eyepiece of the microscope. Assuming the imaging system to follow a linear and shift-invariant nature, this leads the image formation process to be modeled as a convolution between the ideal signal representing the imaged object and the impulse response of the device. While techniques such as confocal [117] and light-sheet microscopy [47] aim to limit the optical blur caused due to contamination from adjacent planes by either blocking the out-of-focus light with a pinhole or by only illuminating a plane of interest at a time, respectively, the use of computational methods as an alternative or supplementary measure to reverse this process continues to be of great interest to the imaging and signal processing community.

The computational technique of deconvolution [87] aims at reducing optical blur using the underlying assumption that the image formation process is approximately linear and shift-invariant, so that it can be characterized by a 3D impulse response or point-spread-function (PSF). However, this is often an ill-posed problem owing to the zeros

present along the axial direction in the transfer function of the PSF, commonly referred to as the optical-transfer-function (OTF). One of the solutions deployed to mitigate this problem is to acquire multiple image stacks after rotating the sample about a lateral axis (orthogonal to the optical axis) and use them during post-processing to reconstruct a representation that has nearly isotropic 3D spatial resolution [90]. However, this technique, commonly referred to as multi-view microscopy, has its own set of difficulties when used in practice. One of the leading challenges in this technique is that of the spatial registration of the multi-view acquisitions, owing to the strong anisotropic spatial resolution in each such acquisition, often rendering conventional intensity-based comparisons inapplicable. Following spatial registration, the subsequent challenge consists of using the acquisitions within the framework of a multi-view deconvolution and fusion algorithm having low computational complexity for a final reconstruction with nearly isotropic spatial resolution.

The primary assumption of spatial shift-invariance for conventional deconvolution algorithms is, however, not always valid along the axial direction in practice. This is unfortunately the case for the imaging of thick biological samples, where light passes through various media with different refractive indices during image formation [36]. When the optical paths differ from the optimal paths for which the objectives are designed, they manifest as spherical aberrations, with the image of a point source becoming dependent on its position in the sample. In general, only the plane position immediately adjacent to a cover-slip of specified refractive index, separated from the objective by an immersion medium of specified thickness and refractive index, will produce an aberration-free image. This solicits the need for spatially-variant deconvolution algorithms that accommodate for such aberrations.

In addition to volumetric acquisitions, the ongoing progress in the hardware and processing capabilities of microscopy techniques have made the collection of multi-dimensional

data ubiquitous. Despite advances in 2D dynamic imaging, the techniques available today still remain slow for acquiring optical sections at successive depths, making it difficult to directly capture the dynamics of fast moving structures. However, when the studied motion has a repetitive nature, such as that in cardiac and pulmonary imaging, one way to circumvent this problem is to sequentially acquire sets of 2D + time sequences at increasing focal depths and later subject them to temporal registration schemes to finally reconstruct a 3D + time sequence. At macroscopic scales, this is often aided by external gating signals such as an electrocardiogram. However, since such signals are either unavailable or cumbersome to acquire in microscopic organisms, fast temporal registration algorithms to efficiently use the information solely contained in the acquisitions, without the need for any data redundancies, aid in minimizing any potential photo damage to the samples during imaging as well as reducing the computational complexity.

1.2   Contribution and Thesis Organization

In this thesis, we propose techniques to model wave propagation inherent in the image formation process and to mitigate the spatial and temporal non-idealities brought about by data acquisition in optical microscopy. We briefly summarize our contributions below.

- **Non-bandlimited and multi-rate generalized discrete characterization of wave propagation (Chapter 2)**

  Based on the scalar diffraction theory in optics and a Hilbert space framework, we propose a digital algorithm to accurately characterize the physical phenomenon of wave propagation that forms an integral part of the image formation process in optical microscopes. Wave propagation can be modeled as an analog convolution operation and its discretization is conventionally performed in the optics community by relying on the assumptions of the classical sampling theory. This is based

Image Formation

Image Deconvolution

Image Registration

Discrete Characterization of Wave Propagation (Chap. 2)

Previous Methods	Our Method
- assume objects do not have abrupt edges and are inherently bandlimited. - assume ideal sampling devices are used for detection. - assume equal sampling rates to represent discrete representations of the waves in the object and image planes.	- represents the objects in suitable shift-invariant spaces to use a Hilbert space model. - is capable to handle non-ideal detectors such as that in finite fill-factor cameras. - uses a multi-rate digital filtering protocol to relate the discrete representations of the waves.

Deconvolution for Multi-View Optical Microscopy (Chap. 4)

Previous Methods	Our Method
- either compute a weighted average of the multi-view measurements without explicit deconvolution or deconvolve single views separately followed by suitable fusion. - require approximations to reduce complexity.	- involves a multi-view deconvolution method that collectively deconvolves the multi-view measurements by sparsity based wavelet regularization with the same computational complexity as the equivalent single-view deconvolution scheme.

Spatial Registration for Multi-View Optical Microscopy (Chap. 3)

Previous Methods	Our Method
- assume isotropic PSF. - require manual supervision of landmarks for registration. - require data-specific landmarks such as cell nuclei. - require fiducial markers added to sample for registration or for hardware calibration.	- accommodates anisotropic PSF. - is an automatic routine with no manual supervision. - is data-independent and doesn't require landmark detection. - doesn't require fiducial markers to be added for registration or hardware calibration.

Depth-Variant Deconvolution for Optical Microscopy (Chap. 5)

Previous Methods	Our Method
- either use a weighted average of the PSF at different regions to deconvolve the measured volume or deconvolve different sub-regions separately followed by suitable fusion.	- involves a depth-variant deconvolution method that collectively deconvolves the measurements by sparsity based wavelet regularization with comparable computational complexity as the equivalent depth-invariant deconvolution.

Temporal Registration for In Vivo Cardiac Microscopy (Chap. 6)

Previous Methods	Our Method
- assume that the sequences to be registered are perfectly periodic. - require the explicit estimation of the time-period of sequences. - require at least one redundant cycle more than the reference. - requires extracting shorter sub-sequences, leading to data loss.	- accommodates sequences that are quasi-periodic. - doesn't require the estimation of the time-period of sequences. - requires only one cycle irrespective of the reference. - is capable to process all cycles without extraction or data loss.

Figure 1.1: An overview of the thesis organization.

on the notion that the spherical waves emanating from the object are band-limited
and that the sampling is ideal. However, these conditions are rarely met in practice,
where signals have finite support or abrupt edges and where sampling is performed
by non-ideal detectors such as finite fill-factor cameras. To solve this problem, we
propose to approximate the wavefront in analog, shift-invariant function spaces,
which do not need to be band-limited. This allows their representation using dis-
crete coefficients that are related via a multi-rate digital filtering operation that
accurately models the analog convolution operator while taking into account non-
ideal sampling devices. This approach retains the efficiency of fast digital filtering
operations and direct sampling but without the band-limiting assumption.

- **Automatic spatial registration for anisotropic PSFs in multi-view optical microscopy (Chapter 3)**

  Multi-view microscopy involves rotating the sample about a lateral axis orthogonal
  to the optical axis and acquiring multiple 3D datasets from different views in order
  to subsequently alleviate the severe axial blur found in each such dataset. However,
  before such datasets can be fused for reconstruction, it is necessary that they are
  spatially aligned to each other. This is a challenging task since these datasets
  have a strong anisotropic blur and are geometrically transformed with respect to
  each other. Automatic algorithms that only rely on maximizing the pixel-based
  similarity or matching the moments provide poor results in such applications. To
  solve this problem, we propose an automatic intensity- and pyramid-based spatial
  registration algorithm that re-blurs the multi-view datasets with transformed forms
  of the PSF in order to make them comparable for spatial registration. This is in
  contrast to existing spatial registration techniques that either naively assume an
  isotropic image formation process, or need manual supervision of landmarks in the

data, or rely on identifying data-specific landmarks, or need fiducial markers added together with the sample for registration (which can inadvertently affect visibility of the sample during imaging), or need hardware calibration.

- **Multi-view deconvolution and fusion with equivalent complexity as single-view processing (Chapter 4)**

  Multi-view deconvolution aims at deconvolving the measurements acquired from different views in multi-view microscopy. We model this multi-view imaging setup as a filter-bank composed of PSFs transformed with respect to each other. We propose a technique to deconvolve these measurements using an iterative shrinkage thresholding technique that seeks a solution that is consistent with the multi-view measurements, while also having a sparse representation with a chosen wavelet basis. Our sparsity based algorithm solves a non-linear objective function to jointly deconvolve and fuse the multi-view datasets to finally yield a single deblurred 3D result with significantly less axial blur than the measurements. Furthermore, the computational complexity of our multi-view deconvolution technique is essentially the same as its single-view counterpart, allowing a fast implementation in practice.

- **Depth-variant deconvolution and fusion for depth-dependent PSFs in optical microscopy (Chapter 5)**

  The imaging of thick samples often involves light passing through various media with different refractive indices, leading to the spatial shift-invariance assumption not being well satisfied along the axial direction. The depth-varying nature of the optical blur found in such 3D datasets renders fast and efficient shift-invariant deconvolution techniques to be inapplicable. In this work, we model the imaging setup using a multi-rate filter-bank structure, where each plane along the optical axis is assigned to a channel with a different PSF. We propose an iterative shrinkage-

thresholding depth-variant 3D deconvolution method that uses depth-dependent PSFs to reconstruct a deblurred form of the imaged thick specimen. We present an approach that directly considers a depth-variant PSF deconvolution problem, yet preserves the form of a highly efficient shift-invariant deconvolution method. The filter bank structure leads to a Landweber deconvolution that uses an iterative shrinkage thresholding algorithm.

- **Non-redundant quasi-periodic temporal registration for in vivo cardiac microscopy (Chapter 6)**

  In vivo cardiac microscopy involves optical imaging of the beating heart as volumes using various imaging modalities at different stages of its morphological development. This often requires the temporal registration of multiple cardiac movies acquired in a serial manner. Using a Hidden Markov Model (HMM), we propose a non-rigid temporal registration tool designed for quasi-periodic signals such as cardiac sequences. Our method is a variant of dynamic time warping that is capable of both temporally warping and wrapping an input sequence by allowing for jump discontinuities in the non-linear temporal alignment function akin to those found in wrapped phase functions. This lifts the need for redundant cycles in the acquired data that are otherwise required for the sole sake of temporal registration. Furthermore, when redundant cycles are indeed available, we show how such redundancies can be used constructively towards frame-rate improvement and noise reduction.

Finally, in Chapter 7, we summarize our contributions towards reconstruction techniques in optical microscopy and provide an outlook for future research.

Throughout this thesis, by convention, we denote the D-dimensional Fourier transform of a function $f(\mathbf{x})$, $\mathbf{x} \in \mathbb{R}^D$, as $\hat{f}(\boldsymbol{\nu})$, $\boldsymbol{\nu} \in \mathbb{R}^D$, with the following definition:

$$\hat{f}(\boldsymbol{\nu}) \stackrel{\text{def}}{=} \int_{\mathbb{R}^D} f(\mathbf{x}) \cdot \exp(-j2\pi\boldsymbol{\nu}^\top\mathbf{x}) \ \mathrm{d}\mathbf{x}, \tag{1.1}$$

$$f(\mathbf{x}) \stackrel{\text{def}}{=} \int_{\mathbb{R}^D} \hat{f}(\boldsymbol{\nu}) \cdot \exp(j2\pi\boldsymbol{\nu}^\top\mathbf{x}) \ \mathrm{d}\boldsymbol{\nu}, \tag{1.2}$$

where $\top$ denotes the conjugate transpose operator.

Chapter 2

Non-bandlimited and Generalized Multi-rate Discrete Model for Wave Propagation

Abstract[1]

Discretization of analog convolution operators by direct sampling of the convolution kernel and use of fast Fourier transforms (FFT) is highly efficient. However, it assumes the input and output signals are bandlimited, a condition rarely met in practice, where signals have finite support or abrupt edges and sampling is non-ideal. Here, we propose to approximate signals in analog, shift-invariant function spaces, which do not need to be bandlimited, resulting in discrete coefficients for which we derive discrete convolution kernels that accurately model the analog convolution operator while taking into account non-ideal sampling devices (such as finite fill-factor cameras). This approach retains the efficiency of direct sampling but not its limiting assumption. We propose fast forward and inverse algorithms that handle finite-length, periodic, and mirror-symmetric signals with

---

[1]This chapter is based on the reference [19] co-authored with T. Blu and M. Liebling.

rational sampling rates. We provide explicit convolution kernels for computing coherent wave propagation in the context of digital holography. When compared to bandlimited methods in simulations, our method leads to fewer reconstruction artifacts when signals have sharp edges or when using non-ideal sampling devices.

2.1   Introduction

Continuous[2] convolution operations are central to model many optical systems and physical phenomena such as wave propagation and diffraction, with applications ranging from optical image formation to digital holography and X-ray scattering [11, 38, 118, 39]. However, since computers can only handle discrete signals, the implementation of such operators requires an accurate mechanism to switch between analog and discrete signals.

Convolution operations are commonly discretized by sampling both the analog input signal and the convolution kernel, with the classical Nyquist-Shannon sampling theory justifying this approach when the signals at hand are bandlimited [89]. However, such an approach suffers from multiple drawbacks. Firstly, most practical signals are not well approximated by bandlimited signals, especially when they have finite support or sharp edges, leading to Gibbs oscillations. Secondly, traditional approaches offer little flexibility regarding the sampling rates of the input and output signals. Thirdly, from a practical perspective, sampling devices, such as digital cameras, gather light over extended areas as opposed to infinitely small points assumed in the ideal sampling model.

Here, we address the problem of approximating continuous convolution operations within the context of generalized sampling theory [109, 107, 46], where analog signals are represented by linear combinations of shifted basis functions that need not be bandlimited. The expansion coefficients in such representations are spatially localized and

---

[2]We use the terms continuous and analog interchangeably in this work.

correspond to discrete signals that can readily be processed by a computer. The formalism also accommodates bandlimited signals and therefore includes the traditional approach as a special case. However, in addition to the slow-decaying sinc function—the underlying building block tied to bandlimited signals—a variety of basis functions can be used to model analog signals with finite support or discontinuities.

Our approach consists of (a) approximating the input signal (via an orthogonal Hilbert projection [55]) in a shift-invariant (SI) space using basis functions adapted to the signal, (b) computing an exact *analog* convolution, and (c) sampling the result by approximating it again (via an orthogonal Hilbert projection) using suitable basis functions. This allows characterizing the input and output signals by a set of discrete coefficients, which are related by a *discrete* convolution. The design, therefore, retains the efficiency of the traditional approach and can readily be implemented using FFT.

While our approach applies to any general convolution operator, we illustrate our method using operators related to wave propagation problems. Specifically, we consider the scalar diffraction theory for wave propagation, the Rayleigh-Sommerfield diffraction integral and its Fresnel approximation [11, 38]. In this context, sampling strategies have been explored previously for Fresnel fields [40, 77, 97, 72] and more general classes of transforms that include the Fresnel transform as a special case [98, 45, 42]. In the particular case of the Fresnel transform, implementations are either *convolution-based* or involve two chirp multiplications and a single FFT [39, 118], the latter thereby providing some computational advantage (though applicable only in the far-field region [54, 73, 71]). The single FFT approach also has its input and output sampling rates as parameter-dependent variants. Methods to address this issue [121, 32] require zero-padding the original signal and thereby offset the computational advantage of the approach. The generalized form of the *convolution-based* approach, which we propose in this work, is related to the Fresnelet formalism [63], with which it shares the basis function representation. Here, however, we

12

do not require that the underlying functions yield multi-resolution spaces.

The chapter is organized as follows. In Section 2.2, we introduce the challenges related to discretizing continuous convolution operations, specifically in the context of coherent propagation of monochromatic scalar wave fields. We derive our method in Section 2.3 and discuss its applicability to digital holography in Section 2.4. In Section 2.5, we evaluate our algorithm in a series of simulation experiments and conclude in Section 2.6.

2.2   Problem Formulation

We consider linear and SI systems, characterized by an impulse response, $h(\mathbf{x})$, $\mathbf{x} = (x, y) \in \mathbb{R}^2$, where the output $g(\mathbf{x})$ is given by the continuous-space (analog) convolution between the complex-valued input signal $f(\mathbf{x})$ and $h(\mathbf{x})$ as:

$$g(\mathbf{x}) \stackrel{\text{def}}{=} \int_{\mathbb{R}^2} f(\boldsymbol{\xi}) \cdot h(\mathbf{x} - \boldsymbol{\xi}) \, \mathrm{d}\boldsymbol{\xi} \stackrel{\text{def}}{=} (f \star h)(\mathbf{x}). \tag{2.1}$$

When f is bandlimited, with maximal frequency less than $1/(2\Delta x)$ and $1/(2\Delta y)$ in the x and y directions, respectively, it is possible to retrieve samples of the continuous convolution, $g[\mathbf{k}] = g(k\Delta x, \ell\Delta y)$ from uniformly-spaced samples of f, $f[\mathbf{k}] = f(k\Delta x, \ell\Delta y)$, $\mathbf{k} = [k, \ell] \in \mathbb{Z}^2$, via the discrete convolution:

$$g[\mathbf{k}] = \sum_{\mathbf{m} \in \mathbb{Z}^2} f[\mathbf{m}] \cdot h_{\mathrm{BL}}[\mathbf{k} - \mathbf{m}] \stackrel{\text{def}}{=} (f * h_{\mathrm{BL}})[\mathbf{k}], \tag{2.2}$$

where $h_{\mathrm{BL}}[\mathbf{k}] = h_{\mathrm{BL}}(k\Delta x, \ell\Delta y)$ denotes samples of the bandlimited impulse response:

$$h_{\mathrm{BL}}(\mathbf{x}) \stackrel{\text{def}}{=} \frac{1}{\Delta x \cdot \Delta y} \left(h(\mathbf{x}) \star \mathrm{sinc}\left(\frac{x}{\Delta x}\right) \mathrm{sinc}\left(\frac{y}{\Delta y}\right) \right). \tag{2.3}$$

However, this straightforward implementation no longer holds if f is not bandlimited. In this work, we consider samples of functions f that are not necessarily bandlimited, and use them to estimate samples of g (and vice-versa). Our approach retains the general form of a discrete convolution as in Eq. (2.2), but we replace $h_{\mathrm{BL}}[\mathbf{k}]$ by a digital filter that is ideally adapted to the problem.

Before proceeding further, we recall the definitions of the scalar wave propagation operators. The Rayleigh-Sommerfeld diffraction integral [38], which relates the scalar field of a propagating wave (having wavelength λ) across two parallel planes separated by a distance z, is a convolution operation as in Eq. (2.1), with the kernel:

$$h_{\mathrm{RS},\lambda,z}(\mathbf{x}) \stackrel{\text{def}}{=} \frac{z}{j\lambda} \cdot \frac{\exp\left(j\frac{2\pi}{\lambda}\sqrt{\|\mathbf{x}\|^2 + z^2}\right)}{\|\mathbf{x}\|^2 + z^2}, \tag{2.4}$$

whose frequency response is given by [38]:

$$\hat{h}_{\mathrm{RS},\lambda,z}(\boldsymbol{\nu}) = \exp\left(j2\pi z\sqrt{\frac{1}{\lambda^2} - \|\boldsymbol{\nu}\|^2}\right), \qquad \boldsymbol{\nu} = (\nu_x, \nu_y) \in \mathbb{R}^2. \tag{2.5}$$

In the Fresnel approximation, h has the form [38]:

$$h_{\mathrm{FrA},\lambda,z}(\mathbf{x}) \stackrel{\text{def}}{=} \frac{\exp\left(j\frac{2\pi}{\lambda}z\right)}{j\lambda z} \cdot \exp\left(\frac{j\pi}{\lambda z}\|\mathbf{x}\|^2\right), \tag{2.6}$$

which, unlike the Rayleigh-Sommerfield kernel $h_{\mathrm{RS},\lambda,z}$, is separable:

$$h_{\mathrm{FrA},\lambda,z}(\mathbf{x}) \stackrel{\text{def}}{=} -j\exp\left(j\frac{2\pi}{\lambda}z\right) \cdot h_{\mathrm{FrT},\tau}(x) \cdot h_{\mathrm{FrT},\tau}(y), \tag{2.7}$$

where the 1D kernel $h_{\mathrm{FrT},\tau}(x)$, with its associated parameter $\tau = \sqrt{\lambda z}$, is defined as:

$$h_{\mathrm{FrT},\tau}(x) \stackrel{\text{def}}{=} \begin{cases} \exp\left(j\frac{\pi}{4}\right) \cdot \delta(x), & \tau = 0 \\ \frac{1}{\tau} \exp\left(j\pi \frac{x^2}{\tau^2}\right), & \text{otherwise,} \end{cases} \tag{2.8}$$

with its frequency response given by:

$$\hat{h}_{\mathrm{FrT},\tau}(\nu) = \exp\left(j\frac{\pi}{4}\right) \cdot \exp\left(-j\pi\tau^2\nu^2\right), \qquad\qquad \nu \in \mathbb{R}. \tag{2.9}$$

This leads to the definition of the unitary 1D Fresnel transform (FrT) [63] of f:

$$\tilde{\mathcal{F}}_\tau\{f\}(x) \stackrel{\text{def}}{=} \tilde{f}_\tau(x) = (f \star h_{\mathrm{FrT},\tau})(x), \qquad\qquad x \in \mathbb{R}. \tag{2.10}$$

Being a unitary transform, the convolution kernel and the frequency response for the inverse FrT are given by the complex conjugates, $h_{\mathrm{FrT},\tau}^{-1}(x) = h_{\mathrm{FrT},\tau}^*(x)$ and $\hat{h}_{\mathrm{FrT},\tau}^{-1}(\nu) = \hat{h}_{\mathrm{FrT},\tau}^*(\nu)$, respectively.

When f is bandlimited, discretizing the wave propagation problem via Eq. (2.3), using the frequency spectrum of the associated convolution kernel, is known by different names in literature, including the *angular-spectrum* method and the *convolution* (CV) based method [54, 73, 71, 121]. In the rest of this work, we refer to such a discretization of any convolution operation using FFT as CV-FFT. For example, the discrete FrT associated with an N-periodic 1D input sequence, $f[k]$ (samples of f at regular intervals Δx), is computed using CV-FFT as:

$$\tilde{f}_\tau^{\mathrm{CV-FFT}}[k] \stackrel{\text{def}}{=} \mathcal{F}_N^{-1}\left\{\mathcal{F}_N(f) \times U^{\mathrm{CV\text{-}FFT}}[k_0]\right\}[k], \qquad -\lfloor N/2 \rfloor \le k, k_0 < \lceil N/2 \rceil, \tag{2.11}$$
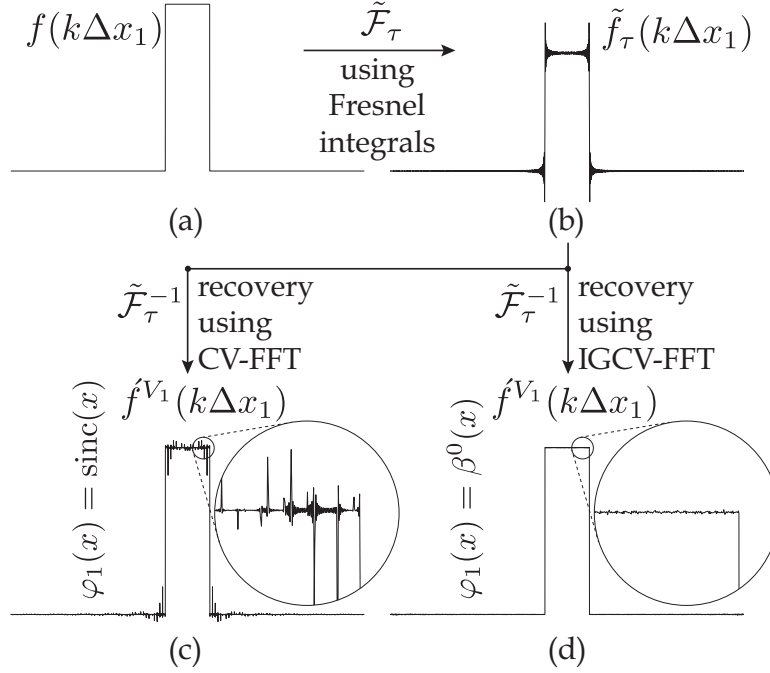
Figure 2.1: (a) A box signal formed with $N = 4096$ samples where $\Delta x_1 = 10\mu$m and aperture width $w = 5.15$mm; (b) Fresnel transform computed using Fresnel integrals [80] with $\lambda = 632$nm and $z = 5$mm (only real values shown); (c) Inverse Fresnel transform of (b) computed using CV-FFT and (d) using IGCV-FFT where prior knowledge $(\varphi_1, \varphi_2, \Delta x_1)$ is exploited for filter design.

where

$$U^{\text{CV-FFT}}[k_0] \overset{\text{def}}{=} \text{rect}\,(k_0/N) \times \hat{h}_{\text{FrT},\tau}(k_0/(N\Delta x)) \tag{2.12}$$

$$\text{rect}\,(\nu) \overset{\text{def}}{=} \begin{cases} 1, & |\nu| < \frac{1}{2} \\ 0, & \text{otherwise,} \end{cases} \tag{2.13}$$

with $\mathcal{F}_N$ and $\mathcal{F}_N^{-1}$ referring to the forward and inverse N-point FFT, respectively. However, when the signals involved are not bandlimited, such a strategy results in ringing artifacts due to the enforced band-limiting operation, even for a near-field region where the technique is usually thought to be effective [54, 73, 71], as shown in Fig. 2.1(a).

16

2.3   Proposed Method

Our approach considers a class of functions far more general than bandlimited signals. We follow the formalism of generalized sampling theory and Hilbert space projections [10], a brief review of which is given in Subsection 2.3.1. The basic assumptions about the functional space to which the input signal belongs are (a) integer shift-invariance, (*i.e.* a basis function shifted by integer-multiples of the signal's sampling step spans the space) and (b) periodicity (*i.e.* the signals it encompasses are periodic; the special case of aperiodic signals is covered when the period tends to infinity).

In this work, we consider the following two problems: (P1) given a sampled form of a signal, f, that belongs to a known SI space, compute samples (or measurements with a known camera) of $g(\mathbf{x}) = (f \star h)(\mathbf{x})$ and conversely, (P2) given measurements of $g(\mathbf{x}) = (f \star h)(\mathbf{x})$, obtained with a known acquisition device, recover the samples of f. We discuss the solutions to these problems in Sections 2.3.2 and 2.3.3, respectively.

2.3.1   Discrete Representation of Analog Signals in Shift-Invariant Spaces using Generalized Sampling Theory

In order to generalize the classical sampling theory, we consider the Hilbert space L_2, which consists of all functions that are square-integrable in Lebesgue's sense. While we focus on 1D signals, extension to higher dimensions will be straightforward. The corresponding L_2-norm in the Hilbert space is:

$$\|f\|_{L_2} \stackrel{\text{def}}{=} \sqrt{\int_{-\infty}^{\infty} |f(x)|^2 \mathrm{d}x} = \sqrt{\langle f, f \rangle}, \tag{2.14}$$

where the L_2-inner product is defined as:

$$\langle f, g \rangle \overset{\text{def}}{=} \int_{-\infty}^{\infty} f(x) \cdot g^*(x) \, \mathrm{d}x. \tag{2.15}$$

We now assume that the input function that we want to sample is in L_2, a space that is considerably more general than the conventional subspace of bandlimited functions. We further consider SI subspaces of L_2 that are generated by scaled and shifted versions of a basis function, φ_1, denoted as:

$$V_1 \overset{\text{def}}{=} \left\{ f \,\middle|\, f(x) = \sum_{k \in \mathbb{Z}} c[k] \cdot \varphi_1 \left(\frac{x}{\Delta x_1} - k \right); \|c\|_{\ell_2} = \sum_{k \in \mathbb{Z}} |c[k]|^2 < \infty \right\}. \tag{2.16}$$

While it would be possible to consider arbitrary basis functions, we want a sampling scheme that is practical and retains the SI nature of the classical Nyquist-Shannon sampling theory. Any function $f \in V_1$, which is continuously defined, is characterized by the sequence of coefficients c as its discrete signal representation, which is not necessarily samples of the signal. For such a continuous/discrete model to be theoretically sound, we need to lay down few mathematical safeguards. First, the sequence of coefficients must be square-summable: $c \in \ell_2$. Second, the representation should be stable and unambiguously defined. In other words, the family of functions $\varphi_1(x - k)_{k \in \mathbb{Z}}$ should form a Riesz basis of V_1, which is the next best thing after an orthogonal basis [27]. This is satisfied when there exists two strictly positive constants A and B such that

$$A\|c\|_{\ell_2}^2 \leq \left\| \sum_{k \in \mathbb{Z}} c[k] \cdot \varphi_1(x - k) \right\|_{L_2}^2 \leq B\|c\|_{\ell_2}^2, \qquad \forall c \in \ell_2. \tag{2.17}$$

A direct consequence of the lower inequality in Eq. (2.17) is that $\sum_k c[k] \cdot \varphi_1(x - k) = 0$ implies that $c = 0$. Thus, the basis functions are linearly independent, which also means

that every signal in V_1 is uniquely specified by its coefficients c. The upper bound implies that the L_2-norm of the signal is finite, so that V_1 is a valid subspace of L_2. Note that the basis is orthonormal if and only if $A = B = 1$, in which case we have a perfect norm equivalence between the continuous and the discrete domains (Parseval's relation). Because of the translation-invariant structure of the construction, the Riesz basis requirement has an equivalent expression in the Fourier domain:

$$A \leq \sum_{k \in \mathbb{Z}} |\hat{\varphi}_1(\nu + k)\|^2 \leq B, \qquad\qquad \forall \nu \in \mathbb{R}. \quad (2.18)$$

The final requirement is that the model should have the capability of approximating any input function as closely as desired by selecting a sampling step Δx_1 that is sufficiently small (similar to the Nyquist criterion). This is equivalent to the partition of unity condition [109]:

$$\sum_{k \in \mathbb{Z}} \varphi_1(x + k) = 1, \qquad\qquad \forall x \in \mathbb{R}. \quad (2.19)$$

In practice, it is this last condition that puts the strongest constraint of the selection of an admissible generating function φ_1. Possible basis functions include the sinc function from the classical Nyquist-Shannon sampling theory, with $\mathring{\varphi}_1(x) = \varphi_1(x) = \text{sinc}(x)$, where V_1 then corresponds to the subspace of L_2 that encompasses functions bandlimited by $1/(2\Delta x_1)$ and c refers to signal samples after the band-limiting operation. Alternatively, B-splines are a popular choice to represent signals with finite-support [108, 25]. The B-spline of degree n is defined as:

$$\beta^n(x) \overset{\text{def}}{=} \underbrace{\left(\beta^0 \star \beta^0 \star \cdots \star \beta^0\right)}_{n+1 \text{ terms}}(x), \qquad\qquad (2.20)$$

where $\beta^0(x) \overset{\text{def}}{=} \text{rect}(x)$ from Eq. (2.13), using which its frequency response can be deduced as $\hat{\beta}^n(\nu) = \text{sinc}^{n+1}(\nu)$.

Having defined such basis functions, we now focus on the fact that any function $f \in L_2$ can be orthogonally projected [55] onto such an SI subspace, $V_1 \subset L_2$, to yield an optimal approximation, f^{V_1}, that is well defined and yields the minimum-error approximation of f into V_1:

$$f^{V_1} = \arg \min_{\tilde{f} \in V_1} \| f - \tilde{f} \|_2^2. \tag{2.21}$$

Note that $f^{V_1}(x) = f(x)$, if $f \in V_1 \subset L_2$. Specifically, the orthogonal projection operation is defined as:

$$f^{V_1}(x) \overset{\text{def}}{=} \frac{1}{\Delta x_1} \sum_{k \in \mathbb{Z}} \left\langle f, \mathring{\varphi}_1 \left(\frac{\bullet}{\Delta x_1} - k \right) \right\rangle \cdot \varphi_1 \left(\frac{x}{\Delta x_1} - k \right) \tag{2.22}$$

$$\overset{\text{def}}{=} \sum_{k \in \mathbb{Z}} c[k] \cdot \varphi_1 \left(\frac{x}{\Delta x_1} - k \right), \tag{2.23}$$

where $\mathring{\varphi}_1$ is the dual of the basis function φ_1, the integer shifted-versions of which span the same space V_1 and also satisfy the biorthogonality condition:

$$\langle \mathring{\varphi}_1(\cdot - m), \varphi_1(\cdot - n) \rangle = \delta[m - n], \qquad m, n \in \mathbb{Z}. \tag{2.24}$$

Note that the dual basis function $\mathring{\varphi}_1$ can be generated as a linear combination of the basis function φ_1 as:

$$\mathring{\varphi}_1(x) \overset{\text{def}}{=} \sum_{k \in \mathbb{Z}} w[k] \cdot \varphi_1(x - k), \tag{2.25}$$

where w is the sequence of weights with its discrete-time Fourier transform given by [10]:

$$W(e^{j2\pi\nu}) = \frac{1}{\sum_{k \in \mathbb{Z}} |\hat{\varphi}_1(\nu + k)|^2} \tag{2.26}$$

20

leading to the frequency response of the dual basis function:

$$\hat{\mathring{\varphi}}_1(\nu) = \frac{\hat{\varphi}_1(\nu)}{\sum_{k \in \mathbb{Z}} |\hat{\varphi}_1(\nu + k)|^2}. \tag{2.27}$$

The projection interpretation of the sampling process has the advantage that it does not require the bandlimited hypothesis and is applicable for a more general class of functions. However, perfect reconstruction is generally not possible when the signal $f \notin V_1$. In the classical scheme with ideal anti-aliasing filtering, the error is entirely due to the out-of-band portion of the signal and its magnitude can be estimated simply by integrating the portion of the spectrum above the Nyquist frequency. For more general spline-like spaces, we can turn to approximation theory [55] to make use of general error bounds that have been derived for similar problems. We can determine the dependence of the approximation error on the sampling step Δx_1 as [109]:

$$\varepsilon_f(\Delta x_1) \overset{\text{def}}{=} \|f - f^{V_1}\|_2 \tag{2.28}$$

$$= \underbrace{\left[\int_{-\infty}^{\infty} \hat{E}_\varphi(\Delta x_1 \nu) |\hat{f}(\nu)|^2 \, d\nu \right]^{1/2}}_{\bar{\varepsilon}_f(\Delta x_1)} + \varepsilon_{\text{corr}}, \tag{2.29}$$

where

$$\hat{E}_\varphi(\nu) \overset{\text{def}}{=} \left(1 - \frac{|\hat{\varphi}_1(\nu)|^2}{\sum_{k \in \mathbb{Z}} |\hat{\varphi}_1(\nu + k)|^2} \right), \tag{2.30}$$

and $\varepsilon_{\text{corr}}$ is a correction term negligible under most circumstances. Specifically, if $f \in W_2^r$ (Sobolev space of order r) with $r > 1/2$, then $\varepsilon_{\text{corr}} < \gamma \Delta x_1^r \|f^{(r)}\|$, where γ is a known constant. Moreover, $\varepsilon_{\text{corr}} = 0$, provided that f is bandlimited to $\nu_{\max} = 1/(2\Delta x_1)$ (Nyquist frequency). Therefore, the estimate $\bar{\varepsilon}_f(\Delta x_1)$ accounts for the dominant part of the approximation error, while $\varepsilon_{\text{corr}}$ is merely a perturbation which may be positive or negative and is guaranteed to vanish provided that f is bandlimited or at least sufficiently

smooth to have $r > 1/2$ derivatives in the L_2-sense (i.e. $f \in W_2^r$). In the latter case, the error can be made arbitrarily small by selecting a sampling step sufficiently small with respect to the smoothness scale of f as measured by $\|f^{(r)}\|$, the norm of its r-th derivative. The minimum requirement for the error to vanish as $\Delta x_1 \to 0$, is $\hat{E}_{\varphi_1}(0) = 0$, a condition that implies the partition of unity [109]. Specifically, if $\hat{E}_{\varphi_1}(\nu) = C^2 \nu^{2L} + \mathcal{O}(\nu^{2L+2})$ as $\nu \to 0$, then the approximation error takes the form [109]:

$$\varepsilon_f(\Delta x_1) = \left[\int_{-\infty}^{\infty} C^2 \Delta x_1^{2L} (\nu)^{2L} |\hat{f}(\nu)|^2 \mathrm{d}\nu \right]^{1/2} \tag{2.31}$$

$$= C \cdot \Delta x_1^L \cdot \|f^{(L)}\|_2, \quad \text{as } \Delta x_1 \to 0, \tag{2.32}$$

where it is assumed that $f \in W_2^L$ so that $\|f^{(L)}\|$ is finite. This implies that the error decays globally as $\mathcal{O}(\Delta x_1^L)$. This rate of decay is called the order of approximation and plays a crucial role in wavelet and approximation theory. For example, the B-splines of degree n have an order of approximation $L = n + 1$ and they are also the shortest and smoothest scaling functions of order L. These provide alternatives to the Nyquist frequency criterion for selecting the appropriate sampling step Δx_1. The error will not be zero in general, but it can be made arbitrarily small without any restriction on f.
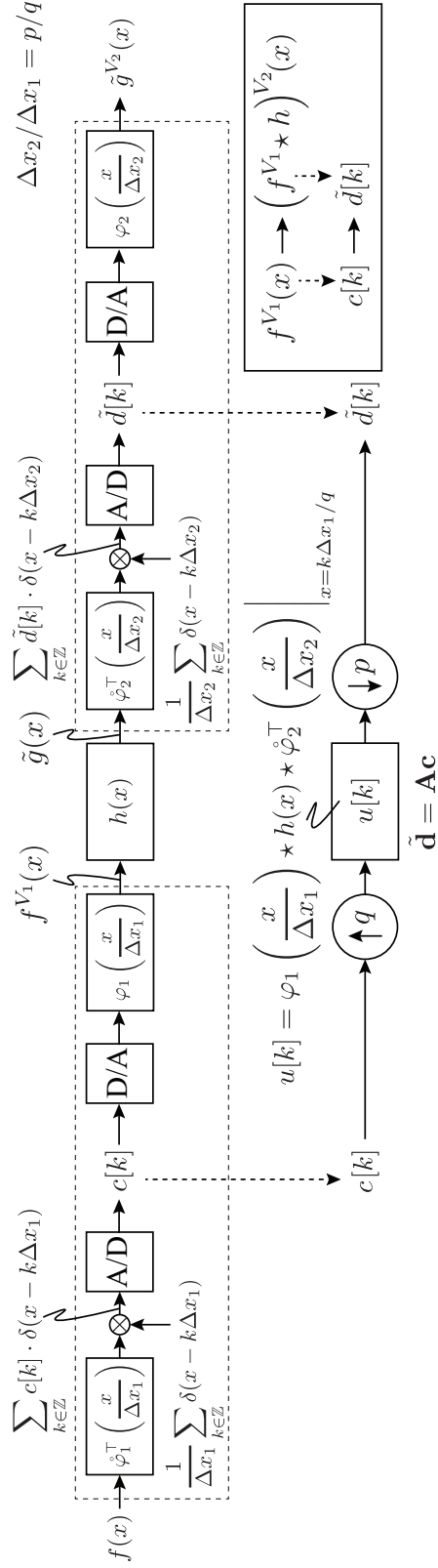
Figure 2.2: The analog convolution $g(x) = (f \star h)(x)$ can be approximated using two suitable SI spaces, $V_i = \text{span}\{\varphi_i(\bullet/\Delta x_i - k)\}_{k\in\mathbb{Z}}$, $(i = 1, 2)$, as $\tilde{g}^{V_2}(x) = (f^{V_1} \star h)^{V_2}(x)$. The expansion coefficients of f^{V_1} and $\tilde{g}^{V_2}$ are related via a discrete convolution with a digital filter, u.

2.3.2   Discretization of Analog Convolution Operators

We now proceed to show that continuous convolution operations of the form:

$$\tilde{g}(x) = \left(f^{V_1} \star h\right)(x),\tag{2.33}$$

can be numerically computed without aliasing, even in cases where f^{V_1} is not bandlimited. With f^{V_1} fully characterized by the discrete sequence c, we also wish to represent $\tilde{g}$ using a similar discrete sequence and therefore approximate it via an orthogonal projection onto an SI space, $V_2 = \mathrm{span}\{\varphi_2(\bullet/\Delta x_2 - k)\}_{k \in \mathbb{Z}}$, to obtain

$$\tilde{g}^{V_2}(x) = \sum_{k \in \mathbb{Z}} \tilde{d}[k] \cdot \varphi_2\left(\frac{x}{\Delta x_2} - k\right).\tag{2.34}$$

This pipeline of operations is illustrated in Fig. 2.2. Despite $f^{V_1}(x)$ and $\tilde{g}^{V_2}(x)$ being both functions of the continuous variable x, they are uniquely characterized by the discrete sequences $c[k]$ and $\tilde{d}[k]$, respectively. Remarkably, when the ratio between their sampling steps is rational, $\Delta x_2/\Delta x_1 = p/q$ $(p, q \in \mathbb{N})$, the sequences $c[k]$ and $\tilde{d}[k]$ are related via a discrete convolution with a digital filter, $u[k]$, shown in Fig. 2.2, whose exact expression we introduce in the following theorem.

Theorem 1 (Equivalent digital filter for analog convolutions): Let $f^{V_1}(x) = \sum_{k \in \mathbb{Z}} c[k] \cdot \varphi_1\left(x/\Delta x_1 - k\right)$, $\tilde{g}(x) = (f^{V_1} \star h)(x)$, and $\tilde{d}[k] = (\Delta x_2)^{-1} \cdot \langle \tilde{g}, \mathring{\varphi}_2\left(\cdot/\Delta x_2 - k\right)\rangle$, with $\Delta x_2/\Delta x_1 = p/q$ $(p, q \in \mathbb{N})$. Then, the coefficients uniquely characterizing f^{V_1} and $\tilde{g}^{V_2}$ are related via a digital filter and sampling-rate conversions as:

$$\tilde{d}[k] = \sum_{\ell \in \mathbb{Z}} c[\ell] \cdot u[pk - q\ell],\tag{2.35}$$

where

$$u(x) = \frac{1}{\Delta x_2} \left\{ \varphi_1 \left(\frac{x}{\Delta x_1} \right) \star h(x) \star \mathring{\varphi}_2^\top \left(\frac{x}{\Delta x_2} \right) \right\}, \qquad (2.36)$$

$$u[k] = u \left(k\Delta x_2/p \right). \qquad (2.37)$$

Proof: See Appendix 2.A.1   □

When the input function is periodic, the discrete convolution in Eq. (2.35) simplifies to a circular convolution that can be implemented using FFT, leading to a generalized CV-FFT algorithm (GCV-FFT), as described in the following theorem.

Theorem 2 (DFT algorithm for computing periodic analog convolutions): Let $f^{V_1}(x) = \sum_{k\in\mathbb{Z}} c[k] \cdot \varphi_1 \left(x/\Delta x_1 - k \right)$ be an $N\Delta x_1$-periodic function ($N \in \mathbb{N}$) and let $h(x)$ be a stable filter with known frequency response $\hat{h}(\nu)$. Then, the orthogonal projection of the continuous convolution $\tilde{g}(x) = (f^{V_1} \star h)(x)$ in an SI space V_2, $\tilde{g}^{V_2}(x) = \sum_{k\in\mathbb{Z}} \tilde{d}[k] \cdot \varphi_2 \left(x/\Delta x_2 - k \right)$, with $\Delta x_2/\Delta x_1 = p/q$ ($p, q, Nq/p \in \mathbb{N}$), is completely characterized by the discrete relation between $\tilde{d}[k]$ and $c[k]$:

$$\tilde{d}[k] = (1/p) \cdot \mathcal{F}_{Nq/p}^{-1} \left\{ \mathcal{F}_N(c) \times U \right\} [k], \qquad 0 \le k < Nq/p \quad (2.38)$$

where $\mathcal{F}_N$ and $\mathcal{F}_N^{-1}$ denotes the N-point DFT and IDFT, respectively, and

$$U[k_0] = q \sum_{m\in\mathbb{Z}} \hat{\varphi}_1 \left(\frac{k_0}{N} - mq \right) \cdot \hat{h} \left(\frac{k_0}{N\Delta x_1} - \frac{mq}{\Delta x_1} \right) \cdot \hat{\mathring{\varphi}}_2^* \left(\frac{pk_0}{Nq} - mp \right), \qquad 0 \le k_0 < Nq.$$
$$(2.39)$$

Proof: See Appendix 2.A.2   □

Note that the N-periodic $\mathcal{F}_N(c)$ is concatenated with its copies to have length Nq, before its point-wise multiplication with the Nq-periodic vector U. The Nq-periodic product vector is then made to fold (alias), with every p-th alternate element added

together, changing its periodicity to Nq/p, before computing its Nq/p-point IDFT. In practice, the infinite-sum in Eq. (2.39) can be truncated to reach any desired accuracy. Note that this infinite sum will converge if $\hat{h}$ is bounded and if the basis functions φ_1, φ_2 generate Riesz bases. An illustration of the discrete implementation of a 1D convolution operation using the above result is shown in Fig. 2.2.

The following corollary describes the special case when $\tilde{g}(x) = \left(f^{V_1} \star h \right)(x)$ is directly sampled without a final orthogonal projection onto V_2.

▶ *Corollary 2.1 (Equivalent digital filter linking input coefficients to samples of the continuous convolution)*: Samples of the convolved signal $\tilde{g}[k] = \tilde{g}(k\Delta x_2)$ are obtained via

$$\tilde{g}[k] = (1/p) \cdot \mathcal{F}_{Nq/p}^{-1} \left\{ \mathcal{F}_N(c) \times U^{\mathrm{s}} \right\}[k], \qquad 0 \leq k < Nq/p \quad (2.40)$$

where U^{s} is the Nq-point vector,

$$U^{\mathrm{s}}[k_0] = q \sum_{m \in \mathbb{Z}} \hat{\varphi}_1\left(\frac{k_0}{N} - mq \right) \cdot \hat{h}\left(\frac{k_0}{N\Delta x_1} - \frac{mq}{\Delta x_1} \right), \qquad 0 \leq k_0 < Nq. \quad (2.41)$$

Proof: Substitute $\hat{\tilde{\varphi}}_2(\nu) = 1$ in Eq. (2.39). $\qquad\qquad \square$

While the input signal f^{V_1} is uniquely defined by the coefficients c, it may also be directly defined by its discrete samples. For this case, the following corollary provides a discrete relationship between the samples of f^{V_1} and $\tilde{g}^{V_2}$ via a digital filter, u_{int}.

▶ *Corollary 2.2 (Equivalent digital filter linking input-output samples of the analog convolution)*: If $f \in V_1$ and $f[k] = f(k\Delta x_1)$ are its uniform samples, then $\tilde{g}^{V_2}[k] = \tilde{g}^{V_2}(k\Delta x_2)$, with $\Delta x_2/\Delta x_1 = p/q$, is given by:

$$\tilde{g}^{V_2}[k] = (1/p) \cdot \mathcal{F}_{Nq/p}^{-1} \left\{ \mathcal{F}_N(f) \times U^{\mathrm{int}} \right\}[k], \qquad 0 \leq k < Nq/p \quad (2.42)$$

where U^{int} is the Nq-point vector,

$$U^{\text{int}}[k_0] = q \sum_{m \in \mathbb{Z}} \hat{\eta}_1 \left(\frac{k_0}{N} - mq \right) \cdot \hat{h} \left(\frac{k_0}{N \Delta x_1} - \frac{mq}{\Delta x_1} \right) \cdot \hat{\mathring{\eta}}_2^* \left(\frac{pk_0}{Nq} - mp \right), \qquad 0 \le k_0 < Nq$$

(2.43)

with

$$\hat{\eta}_i(\nu) = \frac{\hat{\varphi}_i(\nu)}{\sum_{m \in \mathbb{Z}} \hat{\varphi}_i(\nu + m)}, \qquad\qquad i = 1,2 \qquad (2.44)$$

$$\hat{\mathring{\eta}}_i(\nu) = \frac{\hat{\varphi}_i(\nu) \cdot \left(\sum_{m \in \mathbb{Z}} \hat{\varphi}_i^*(\nu + m) \right)}{\sum_{n \in \mathbb{Z}} |\hat{\varphi}_i(\nu + n)|^2}. \qquad\qquad (2.45)$$

Proof: Since $f \in V_1$, $f(x) = f^{V_1}(x)$ and can be represented as in Eq. (2.23), with $c[k]$ and φ_1 replaced by $f[k]$ and η_1, respectively, where η_1 is the equivalent interpolating (*i.e.* $\eta_1(k) = \delta[k]$, $k \in \mathbb{Z}$) basis function that also spans V_1 [10]. Similarly, $\tilde{g}^{V_2}(x)$ can also be represented using $\tilde{g}^{V_2}[k]$ and η_2. The DFT of the digital filter u_{int} is then found by replacing $\hat{\varphi}_1$ and $\hat{\mathring{\varphi}}_2$ in Eq. (2.39) by $\hat{\eta}_1$ and $\hat{\mathring{\eta}}_2$, respectively. Note that the discrete samples $\tilde{g}[k]$ can also be directly obtained from $f[k]$, using Eq. (2.42), by substituting $\hat{\mathring{\eta}}_2(\nu) = 1$ in Eq. (2.43). $\qquad\qquad\square$
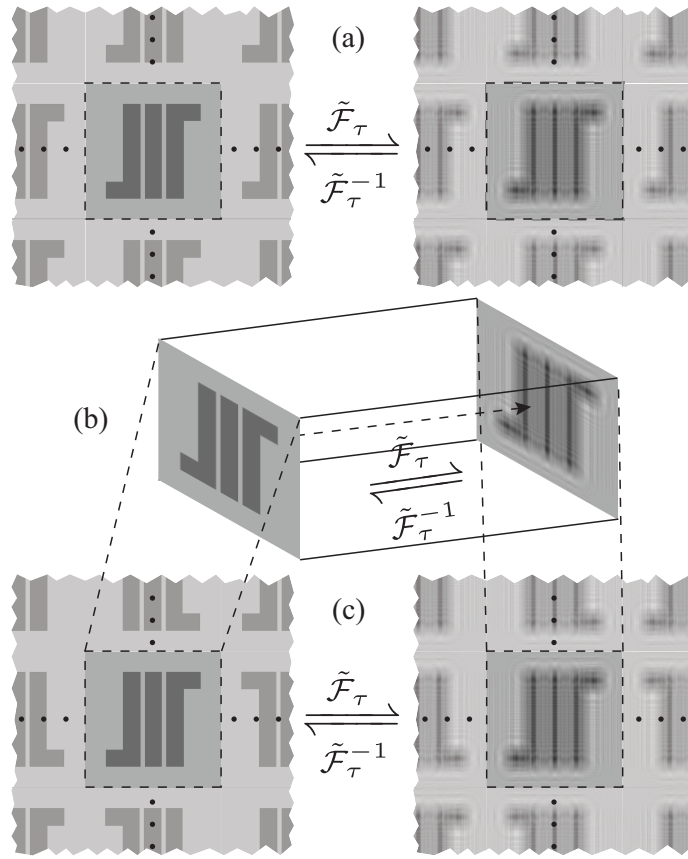
Figure 2.3: The two boundary conditions discussed for discrete Fresnel transform: (a) periodic boundaries; (b) Propagation of a finite-sized object/field confined within a rectangular waveguide lined with mirrors on its four interior planar surfaces, analogous to using (c) mirror-symmetric boundaries for the discrete transform.

The number of computations required to carry out the discrete convolution in Theorem 2 can be further reduced when the signals involved have symmetric boundary conditions. In what follows, we distinguish between discrete periodic signals with *whole-sample* (WS) and *half-sample* (HS) mirror-symmetry [13]. Such signals are symmetric about a sample and about a point midway between two samples, respectively. Such boundary conditions are illustrated in Fig. 2.3.

▶ *Corollary 2.3 (Low complexity DFT algorithm for analog convolution of signals with mirror-symmetry):* Let $f^{V_1}(x) = \sum_{k \in \mathbb{Z}} c^{\mathrm{HS}}[k] \cdot \varphi_1(x/\Delta x_1 - k)$, with c^{HS} being a $2N$-point periodic sequence having HS mirror-symmetry,

$$c^{\mathrm{HS}}[k] = c[\min(k, 2N - 1 - k)], \qquad\qquad 0 \le k < 2N \quad (2.46)$$

If $u(x) = u(-x)$ in Eq. (2.36) and $\Delta x_1 = \Delta x_2$, then we have $\tilde{g}^{V_2}(x) = \sum_{k \in \mathbb{Z}} \tilde{d}^{\mathrm{HS}}[k] \cdot \varphi_2(x/\Delta x_1 - k)$, where $\tilde{d}^{\mathrm{HS}}[k]$ is also a $2N$-point sequence with HS mirror-symmetry. Furthermore, the even and odd elements of its corresponding N-point first-half, $\tilde{d}[k]$, are given by:

$$\tilde{d}[2k] = \tilde{d}^{\mathrm{HS}}[2k] \stackrel{\text{def}}{=} \tilde{d}^{\mathrm{HS}}_{\mathrm{even}}[k], \qquad\qquad 0 \le k < \lceil N/2 \rceil \qquad\qquad (2.47)$$

$$\tilde{d}[2k + 1] = d^{\mathrm{HS}}_{\mathrm{even}}[N - 1 - k], \qquad\qquad 0 \le k < \lceil (N - 1)/2 \rceil \qquad (2.48)$$

where

$$\tilde{d}^{\mathrm{HS}}_{\mathrm{even}}[k] = \mathcal{F}_N^{-1} \left\{ \frac{\mathcal{F}_{2N}\left\{\tilde{d}^{\mathrm{HS}}\right\}[\circ] + \mathcal{F}_{2N}\left\{\tilde{d}^{\mathrm{HS}}\right\}[\circ + N]}{2} \right\}[k], \qquad 0 \le k < N \qquad (2.49)$$

and

$$\mathcal{F}_{2N}\left\{\tilde{d}^{\mathrm{HS}}\right\}[k_0] \stackrel{\mathrm{def}}{=} \mathcal{F}_{2N}\left\{c^{\mathrm{HS}}\right\}[k_0] \times U^{\mathrm{WS}}, \quad 0 \le k_0 < 2N \tag{2.50}$$

$$\mathcal{F}_{2N}\left\{c^{\mathrm{HS}}\right\}[k_0] = \mathcal{F}_{N}\left\{c^{\mathrm{HS}}_{\mathrm{even}}\right\}[k_0] + \left\{\exp\left(j\frac{\pi}{N}k_0\right)\cdot \mathcal{F}_{N}\left\{c^{\mathrm{HS}}_{\mathrm{even}}\right\}[N-k_0]\right\}, \tag{2.51}$$

$$U^{\mathrm{WS}}[k_0] = \sum_{m\in\mathbb{Z}}\hat{\varphi}_1\left(\frac{k_0}{2N}-m\right)\cdot\hat{h}\left(\frac{k_0}{2N\Delta x_1}-\frac{m}{\Delta x_1}\right)\cdot\hat{\bar{\varphi}}_2^{*}\left(\frac{k_0}{2N}-m\right). \tag{2.52}$$

Proof: When $c[k]$ and $u[k]$ have HS and WS symmetry respectively, $\tilde{d}[k] = (c*u)[k]$ has HS symmetry [13]. The mirror-symmetry in the input and output signals thereby allows their DFT/IDFT to be computed using half-length counterparts [33]. Note that Eq. (2.52) is exactly similar to Eq. (2.39), with N replaced by $2N$ and $p = q = 1$.   □

It follows that if φ_1, φ_2 have even symmetry (*e.g.* B-splines), the stated requirement of $u(x) = u(-x)$ is satisfied if $h(x) = h(-x)$ (*e.g.* Fresnel transform). The fact that the calculations involve non-redundant signals of half and quarter the original size in the 1D and 2D cases, reduces the FFT/IFFT computational complexity involved by around 50% and 75%, respectively.

2.3.3   Invertibility of the Equivalent Digital Filters

Having discussed our solution to the forward problem (P1), we next look at the inverse problem (P2) to estimate samples of the original signal f from the measurements of $g(x) = (f \star h)(x)$, obtained with a known acquisition device. We refer to this as the inverse GCV-FFT algorithm (IGCV-FFT), corresponding to a continuous filter, h.

Invertibility is particularly important in digital systems [8] and has been investigated for Fresnel-like transforms before [2, 49]. Here, we seek a sequence $c_{\mathrm{LS}}[k]$ whose forward transform closely matches $d[k]$ in the least-squares sense. In the following theorem, we prove that the coefficients $c_{\mathrm{LS}}[k]$ can be obtained from $d[k]$ by applying a digital filter,

$v[k]$ (Fig. 2.4), and provide its FFT coefficients.

Theorem 3 (Least-squares reconstruction from sampled analog convolution):

Let $f(x)$ be an $N\Delta x_1$-periodic function ($N \in \mathbb{N}$) and let $h(x)$ be a stable filter. Let the

orthogonal projection of the analog convolution $g(x) = (f \star h)(x)$ in an SI space V_2 be

denoted as $g^{V_2}(x) = \sum_{k\in\mathbb{Z}} d[k] \cdot \varphi_2 (x/\Delta x_2 - k)$, with $\Delta x_2/\Delta x_1 = p/q$ ($p, q, Nq/p \in \mathbb{N}$).

Then, given d, the coefficients that give the least-squares solution c_{LS} in the SI space V_1:

$$c_{\mathrm{LS}} = \arg\min_{\tilde{c}\in\ell_2} \sum_{k=0}^{Nq/p-1} \left| d[k] - \frac{1}{\Delta x_2} \sum_{\ell=0}^{N-1} \tilde{c}[l] \cdot \varphi_1 \left(\frac{x}{\Delta x_1} - \ell \right) \star h(x) \star \mathring{\varphi}_2^\top \left(\frac{x}{\Delta x_2} \right) \Big|_{x=k\Delta x_2} \right|^2 \tag{2.53}$$

is obtained through the linear filtering operation,

$$c_{\mathrm{LS}}[k] = (1/q) \cdot \mathcal{F}_N^{-1} \left\{ \mathcal{F}_{Nq/p}(d) \times V_{\mathrm{LS}} \right\} [k], \qquad 0 \le k < N \tag{2.54}$$

where

$$V_{\mathrm{LS}}[k_0] = pq \; \mathbf{U}_{k_0 \bmod N}^\dagger [0,0], \qquad 0 \le k_0 < Nq \tag{2.55}$$

and $\mathbf{U}_r^\dagger$ denotes the Moore-Penrose pseudo-inverse of the $q \times p$-sized matrix $\mathbf{U}_r$:

$$\mathbf{U}_r[m,n] = U \left[r + Nm + \frac{Nq}{p}n \right], \qquad 0 \le m < q, 0 \le n < p \tag{2.56}$$

with U defined as in Eq. (2.39).

Proof: See Appendix 2.A.3   □

When $\Delta x_1 = \Delta x_2$ ($p = q = 1$), the above result simplifies to $V_{\mathrm{LS}}[k_0] = 1/U[k_0]$,

$0 \le k_0 \le N - 1$, for non-zero values of U, and zero otherwise. In particular, when

$h = h_{\mathrm{FrT},\tau}$ is the Fresnel transform kernel and φ_1, φ_2 are chosen as B-spline functions

with $\Delta x_1 = \Delta x_2$, the FFT coefficients $U[k_0]$ in Eq. (2.39) are always non-zero, thereby ensuring the possibility of perfect reconstruction. For arbitrary choices of φ_1, φ_2, Δx_1, Δx_2 and h, the minimum ℓ_2-norm solution yields perfect reconstruction, if and only if the $q \times p$ matrices in Eq. (2.56) are full-rank matrices, with their rank equal to p. A similar inverse to Corollary 2.2 is straightforward in this context, where $\acute{f}^{V_1}[k] = \acute{f}^{V_1}(k\Delta x_1)$, $\acute{f}^{V_1}(x) = \sum_{k \in \mathbb{Z}} c_{\mathrm{LS}}[k] \cdot \varphi_1 (x/\Delta x_1 - k)$, can be obtained from $\tilde{g}^{V_2}[k]$ using a digital filter, $v_{\mathrm{int}}[k]$, whose FFT coefficients V^{int} can be obtained from Eq. (2.55), with U in Eq. (2.56) replaced by U^{int} of Eq. (2.43).

We next consider minimizing the worst-case regret over all possible values of $f \in L_2$ that are consistent with the given samples of $g(x) = (f \star h)(x)$ measured in V_2.

Theorem 4 (Minimax regret reconstruction from sampled analog convolution): Let $f(x)$ be an $N\Delta x_1$-periodic function ($N \in \mathbb{N}$) and let $h(x)$ be a stable filter. Let the orthogonal projection of the analog convolution $g(x) = (f \star h)(x)$ in an SI space V_2 be denoted as $g^{V_2}(x) = \sum_{k \in \mathbb{Z}} d[k] \cdot \varphi_2 (x/\Delta x_2 - k)$, with $\Delta x_2/\Delta x_1 = p/q$ ($p, q, Nq/p \in \mathbb{N}$). Then, given d, the coefficients that give the minimax regret solution c_{MR} in the SI space V_1:

$$c_{\mathrm{MR}} = \arg \min_{\tilde{c} \in \ell_2} \max_{f \in S} \left\| \sum_{\ell=0}^{N-1} \tilde{c}[\ell] \cdot \varphi_1 \left(\frac{x}{\Delta x_1} \right) - f^{V_1}(x) \right\|_{L_2} \tag{2.57}$$

where $S \subset L_2$ is the subset of all functions f that when subjected to the analog convolution with h and orthogonal projection onto V_2 give the same samples d:

$$S = \{f : f(x) \star \frac{1}{\Delta x_2} \left(h(x) \star \mathring{\varphi}_2^\top \left(\frac{x}{\Delta x_2} \right) \right) \Big|_{x=k\Delta x_2} = d[k]\}, \tag{2.58}$$

is obtained through the linear filtering operation,

$$c_{\mathrm{MR}}[k] = (1/q) \cdot \mathcal{F}_N^{-1} \left\{ \mathcal{F}_{Nq/p}(d) \times V_{\mathrm{MR}} \right\}[k], \quad 0 \le k < N, \tag{2.59}$$

where

$$V_{\mathrm{MR}}[k_0] = p \sum_{m \in \mathbb{Z}} \hat{\varphi}_3 \left(\frac{pk_0}{Nq} - mp \right) \cdot \hat{\mathring{\varphi}}_1^* \left(\frac{k_0}{N} - mq \right), \qquad 0 \le k_0 < Nq, \tag{2.60}$$

$$\hat{\varphi}_3(\nu) = \frac{\hat{\varphi}_2(\nu) \cdot \hat{h}^*(\nu/\Delta x_2) \cdot \sum_{m \in \mathbb{Z}} |\varphi_2(\nu + m)|^2}{\sum_{n \in \mathbb{Z}} \left| \hat{\varphi}_2(\nu + n) \cdot \hat{h}^* \left((\nu + n)/\Delta x_2 \right) \right|^2}. \tag{2.61}$$

Proof: As shown in Fig. 2.4(b), if the analog convolution and the dual basis function for V_2 is grouped together as $\mathring{\varphi}_3^\top(x/\Delta x_2) = h(x) \star \mathring{\varphi}_2^\top(x/\Delta x_2)$, then this is comparable to the problem of reconstructing a signal from the samples obtained with a non-ideal acquisition device characterized by φ_3. We refer the reader to [30] for a similar proof to the above problem.   □

2.4   Application to Digital Holography

We now derive discrete filters for the Rayleigh-Sommerfeld diffraction integral and the Fresnel transform. This is achieved by replacing the continuous filter h in the expression for the digital filter $u[k]$, derived in Eq. (2.37) of Theorem 1, by $h_{\mathrm{RS},\lambda,z}$ and $h_{\mathrm{FrT},\tau}$ (or $h_{\mathrm{FrA},\lambda,z}$), respectively. The 2D FFT coefficients of the digital filter corresponding to the Rayleigh-Sommerfeld diffraction integral can be thus obtained by extending Eq. (2.39) to 2D as follows:

$$U^{\mathrm{RS}}[k_0, l_0] = q_x q_y \sum_{m,n \in \mathbb{Z}} \left\{ \hat{\varphi}_1 \left(\frac{k_0 - mN_x q_x}{N_x}, \frac{l_0 - nN_y q_y}{N_y} \right) \right.$$

$$\cdot \hat{h}_{\mathrm{RS},\lambda,z} \left(\frac{k_0 - mN_x q_x}{N_x \Delta x_1}, \frac{l_0 - nN_y q_y}{N_y \Delta y_1} \right) \cdot \hat{\hat{\varphi}}_2^* \left(\frac{k_0 - mN_x q_x}{N_x q_x / p_x}, \frac{l_0 - nN_y q_y}{N_y q_y / p_y} \right) \Bigg\},$$

(2.62)

for $0 \leq k_0 < N_x q_x$, $0 \leq l_0 < N_y q_y$, where $\Delta x_2 / \Delta x_1 = p_x / q_x$, $\Delta y_2 / \Delta y_1 = p_y / q_y$. Similarly, the 1D FFT coefficients of the digital filter corresponding to the separable and unitary FrT can be deduced as:

$$U^{\mathrm{FrT}}[k_0] = q \sum_{m \in \mathbb{Z}} \Bigg\{ \hat{\varphi}_1 \left(\frac{k_0 - mNq}{N} \right) \cdot \hat{\hat{\varphi}}_2^* \left(\frac{k_0 - mNq}{Nq/p} \right) \cdot \exp \left(j \frac{\pi}{4} \right)$$
$$\cdot \exp \left(-j\pi \tau^2 \left(\frac{k_0 - mNq}{N \Delta x_1} \right)^2 \right) \Bigg\},$$

(2.63)

for $0 \leq k_0 < Nq$. Note that the bandlimited CV-FFT approach in Eq. (2.11) reduces to a special case of Eq. (2.63), where $\hat{\varphi}_1(\nu) = \hat{\varphi}_2(\nu) = \mathrm{rect}(\nu)$ and $\Delta x_1 = \Delta x_2$.

Figure 2.4: (a) For the inverse operation, given the expansion coefficients of g^{V_2}, those of $(g \star h^{-1})^{V_1 \perp V_3}$, where V_3 is the SI space spanned by $\mathring{\varphi}_3(x/\Delta x_2) = h(x) \star \mathring{\varphi}_2(x/\Delta x_2)$, correspond to a least-squared reconstruction and can be computed via a discrete convolution with a digital filter, v_{LS}. (b) Similarly, the minimax-regret reconstruction can also be computed via a discrete convolution with a digital filter, v_{MR}.

2.5   Experimental Results and Discussion

With the framework for the numerical implementation of convolution operations laid out in the previous sections, we now illustrate its features and practical applicability, via simulation results.

2.5.1   Inverse Transform from Sampled Fresnel Integral

Here, we compare the reconstruction fidelity for CV-FFT and IGCV-FFT, by individually estimating a signal from its Fresnel transform samples, where the latter is originally calculated using the more computationally-intensive and accurate Fresnel integrals [38]. We consider a box signal, $f(x)$, with aperture-width $w = 5.15$mm, composed of $N = 4096$ samples, spaced apart by $\Delta x_1 = 10\mu$m (Fig. 2.1(a)). We use a box function as the reference since its Fresnel transform can be numerically computed using Fresnel integrals in an accurate manner. Using a C implementation of the integral [80], we obtain the Fresnel transform samples $\tilde{f}_\tau(k\Delta x_1)$, with $\tau = (\lambda z)^{0.5}$ given by $\lambda = 632$nm and $z = 5$mm, as in Fig. 2.1(b). We then estimate $f(k\Delta x_1)$ from $\tilde{f}_\tau(k\Delta x_1)$, using CV-FFT and IGCV-FFT.

While the inverse FrT computed with CV-FFT can be seen to suffer from Gibbs oscillations (Fig. 2.1(c)), the reconstruction obtained using IGCV-FFT (with $\varphi_1(x) = \beta^0(x)$, $h(x) = h_{\mathrm{FrT},\tau}(x)$, $\varphi_2(x) = \delta(x)$ and $\Delta x_1 = \Delta x_2$ in Eq. (2.39)) produces a more fair reconstruction (Fig. 2.1(d)).

2.5.2   Reconstruction of Non-bandlimited Signals Leveraging A Priori Knowledge

We now illustrate how the knowledge that the recovered signal lies in a space V_1 can be exploited during inversion using IGCV-FFT. We consider the signal $f(x)$ shown in

Fig. 2.5(a), defined as a linear combination of box, linear and cubic B-splines. Due to the inherent linearity and shift-invariance of the system, the Fresnel transform samples of $f(x)$ are given by adding the output of three instances of GCV-FFT, where $\varphi_1(x) = \beta^i(x)$ and $\varphi_2(x) = \delta(x)$, for $i = 0, 1, 3$, respectively (Fig. 2.5(b)). We then attempt to reconstruct $f(x)$ by alternately assuming that it lies in a bandlimited space (which it does not) or in any one of the three different SI spaces $V_1 = \text{span}\left\{\beta^i\left(\bullet - k\right)\right\}_{k \in \mathbb{Z}}$, $i = 0, 1, 3$ (which it does not either, since f is a combination of all three). The CV-FFT approach, in Fig. 2.5(c), suffers from severe ringing artifacts, particularly because none of the three basis functions constituting the input signal is similarly bandlimited. Instead, using the inverse filter in Eq. (2.55) with $\varphi_1(x) = \beta^i(x)$, $\varphi_2(x) = \delta(x)$ and $\Delta x_1 = \Delta x_2$ for $i = 0, 1, 3$, the reconstructions are all ringing-free, yet they faithfully recover only those spatial regions of $f(x)$ that are well represented in V_1 (Fig. 2.5(d-f)).

2.5.3   Modeling of Acquisition Sensors with Finite Fill-factors

We next look at how GCV-FFT can naturally model the imaging process with digital cameras, where each sensor spatially-averages the incoming signal over its active area (Fig. 2.6(a)) to give a pixel value. Note that this boils down to taking $\varphi_2(x) = \beta^0(x/\gamma)$ (Fig. 2.6(b)), with $d[k]$ then representing the pixel values. The corresponding dual basis is similarly defined as $\mathring{\varphi}_2(x) = (1/\gamma)\beta^0(x/\gamma)$, where $0 < \gamma \leq 1$ is the fill-factor [97], defined as the ratio between the integration area and the pixel size it represents.

As an example, we consider the Fresnel transform of a square aperture that is measured by its projection onto $V_{\text{CCD}} = \text{span}\left\{\varphi_2\left(\bullet/\Delta x_2 - k\right)\right\}_{k \in \mathbb{Z}}$, where $\varphi_2(x) = \beta^0(x/\gamma)$ (Fig. 2.6(c)). Since the model underlying the CV-FFT reconstruction does not match the acquisition procedure, the bandlimited reconstruction produces ringing artifacts. These artifacts can be visually highlighted as dark regions using the Structural Similarity Map
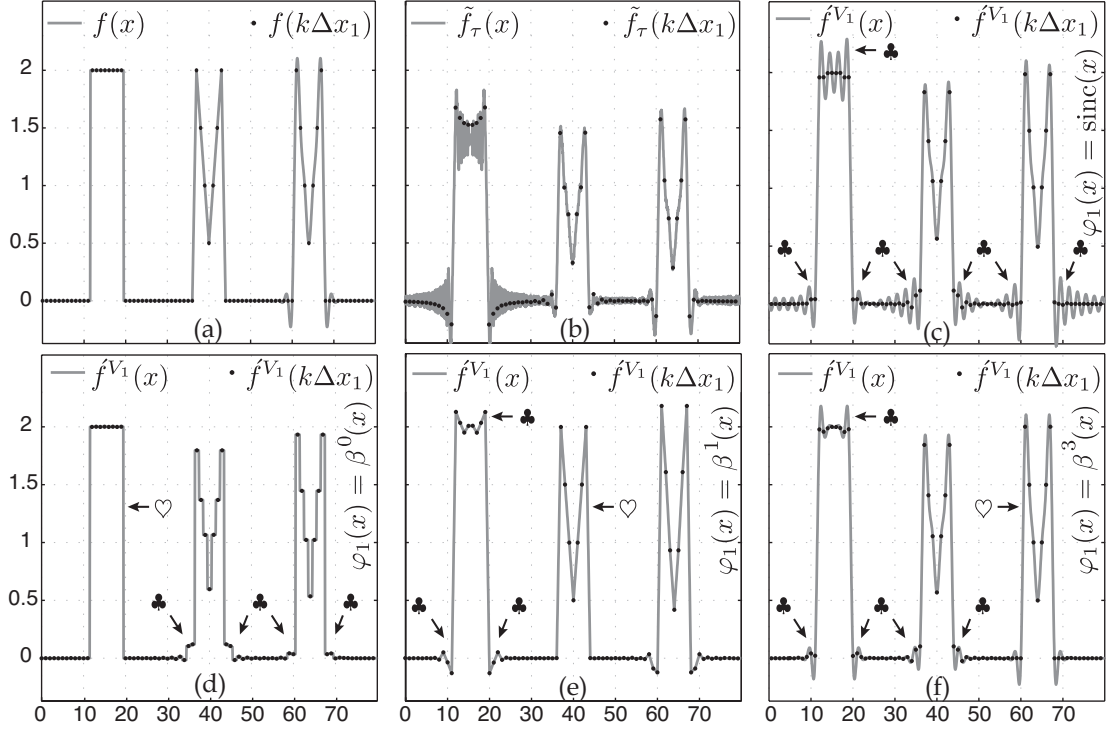
Figure 2.5: (a) $f(x)$ composed of three types of basis functions (β^0, β^1 and β^3); (b) $\tilde{f}_\tau(x)$, where $\tau = 1$, (only real values shown) and its samples used for the recovery of $f(x)$; (c) The reconstructed signal and samples in the bandlimited space, obtained using CV-FFT; (d)-(f) The recovered signal in the three separate SI spaces, $V_1 = \text{span}\left\{\beta^i\left(\bullet - k\right)\right\}_{k \in \mathbb{Z}}$, $i = 0, 1, 3$, using IGCV-FFT. Clover leaves indicate reconstruction artifacts (e.g. Gibbs oscillation) and hearts denote perfect reconstruction.

(SSIM) [116], which associates a high index (1) to regions similar to the ground truth and a low index (0) to regions that differ, as shown in Fig. 2.6(e). Instead, by using $\varphi_1(x) = \beta^0(x)$, $h(x) = h_{\text{FrT},\tau}(x)$, $\varphi_2(x) = \beta^0(x/\gamma)$, the IGCV-FFT algorithm is well adapted to the problem at hand and hence yields perfect reconstruction (Fig. 2.6(f-g)).

In the particular context of digital holography, Stern et al. [97], and more recently Kelly et al. [51], have shown that finite-size pixels attenuate high spatial frequencies in the propagated signal, in addition to the artifacts introduced by the sampling operation, rendering perfect reconstruction virtually impossible. Here, we overcome this limitation by leveraging prior knowledge of the basis functions that underly the acquisition device
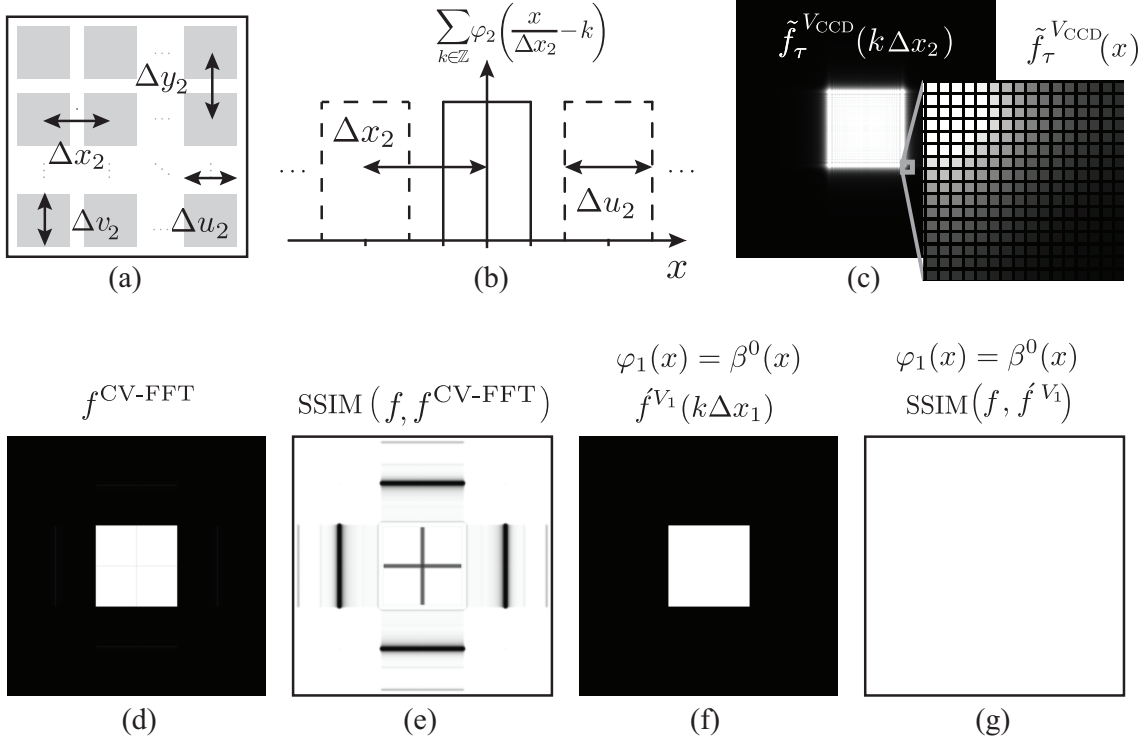
Figure 2.6: (a) A typical CCD with finite-size detector elements, and (b) its corresponding family of 1D basis functions; (c) $\tilde{f}_{(\lambda \cdot z)^{0.5}}^{V_{\mathrm{CCD}}}(k\Delta x_2)$ (only absolute values shown) ($\lambda = 632$nm, $z = 1$cm, $\Delta x_1 = \Delta x_2 = 10\mu$m, $\gamma = 0.7$) for a square aperture, $f(x)$ (not shown); (d) Reconstruction using CV-FFT and (e) its SSIM map showing the presence of artifacts (white: SSIM=1, black: SSIM=0); (f) reconstruction using IGCV-FFT, yielding (g) an SSIM map that is uniformly 1 (white, perfect reconstruction).

and the signal.

2.5.4   Comparison of GCV-FFT with IGCV-FFT

Since GCV-FFT allows discretizing forward convolutions with h, it could also be used to approximate the inverse operation h^{-1}. However, this is not equivalent to computing the IGCV-FFT algorithm for h. Specifically, for a signal $f \in V_1$, the sequence of operations consisting of (a) continuous convolution with h, (b) projection onto V_2, (c) continuous convolution with h^{-1} and finally (d) projection onto V_1, is usually not identity.
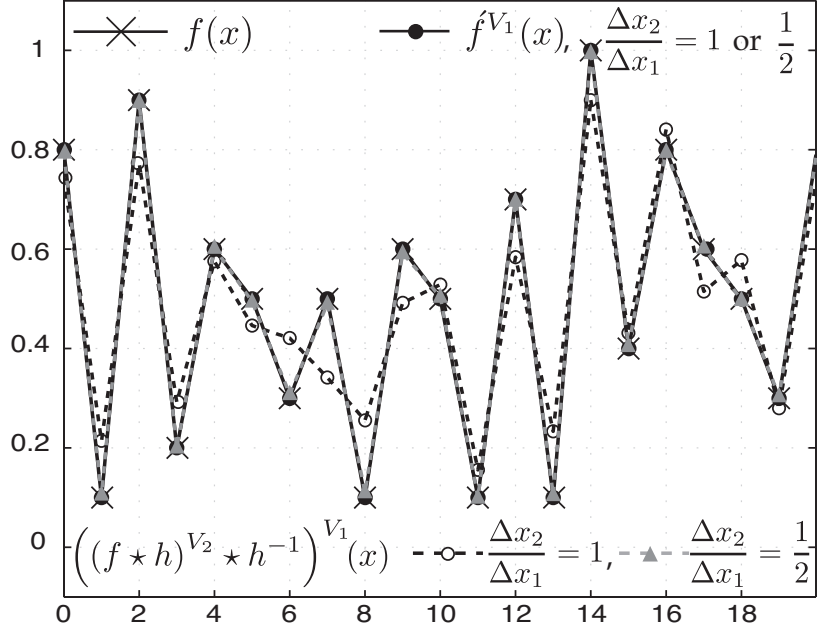
Figure 2.7: Comparison of methods to estimate f from $\tilde{f}_\tau^{V_2}$ (not shown), where $\tau = 2.5$ and $\varphi_2 = \beta^1$, using *discrete-inverse* $\acute{f}^{V_1}$ with IGCV-FFT, and alternatively, using *discretized-continuous-inverse* $(\tilde{f}_\tau^{V_2} \star h_{\mathrm{FrT},\tau}^{-1})^{V_1}$ with GCV-FFT.

In order to illustrate the difference between using (i) GCV-FFT for h^{-1} and (ii) IGCV-FFT for h, we consider a signal $f \in V_1 = \mathrm{span}\,\{\beta^1\,(\bullet/\Delta x_1 - k)\}_{k \in \mathbb{Z}}$, as shown in Fig. 2.7. Using GCV-FFT, we compute its discretized FrT, $\tilde{f}_\tau^{V_2}$, measured via projection into $V_2 = \mathrm{span}\,\{\beta^1\,(\bullet/\Delta x_2 - k)\}_{k \in \mathbb{Z}}$, with $\Delta x_2/\Delta x_1 = 1$ or $1/2$. We then estimate f from $\tilde{f}_\tau^{V_2}$ using either approach and compare the reconstruction results. The reconstruction obtained using (i) differs from f, while (ii) proves to be a perfect reconstruction (Fig. 2.7). The quality of the reconstructed signal using (i) improves when $\Delta x_2/\Delta x_1 = 1/2$. The IGCV-FFT approach yields perfect reconstruction for both $\Delta x_2/\Delta x_1 = 1$ and $1/2$.

2.6   Discussion and Conclusion

By approximating input and output functions as linear combinations of localized basis functions we obtain a flexible framework to compute continuous convolutions. Its main features are summarized below: (i) it does not require assuming the input or output signals are bandlimited, thereby limiting Gibbs oscillation artifacts near sharp edges, (ii) it takes into account variable sampling rates between the input and output signals making it suitable for multi-resolution algorithms [63, 62], (iii) the implementation retains the form of a discrete convolution, making it directly applicable wherever bandlimited methods are in use, (iv) the basis functions can be chosen to match the experimental, camera-specific setups, (v) both periodic and mirror-periodic boundary conditions can be selected (with a fast algorithm for mirror-periodic signals that reduces the computational complexity by a factor of around 2 (in 1D) and 4 (in 2D) over direct periodic implementation), and (vi) the equivalent discrete inverse operator, optimal in the least-squares sense, can be implemented using the same algorithm. Our approach could be applied to a wide range of analog operators. Experiments to compute and reconstruct complex wave-fields indicate that our approach might be particularly well suited for digital holography applications. To facilitate integration with existing methods (which could include recent compressed-sensing methods [24, 69, 86]) and spur new uses, we make the software implementation of our algorithms available [16].

2.A   Appendix

2.A.1   Proof of Theorem 1

The coefficients d characterizing $\tilde{g}^{V_2}$ are given by the L_2-inner product:

$$d[k] = \frac{1}{\Delta x_2} \int_{-\infty}^{\infty} \tilde{g}(\eta) \cdot \mathring{\varphi}_2^{\top} \left(k - \frac{\eta}{\Delta x_2} \right) \mathrm{d}\eta \tag{2.64}$$

$$= \frac{1}{\Delta x_2} \int_{-\infty}^{\infty} \left(\int_{-\infty}^{\infty} f^{V_1}(\xi) \cdot h(\eta - \xi) \mathrm{d}\xi \right) \mathring{\varphi}_2^{\top} \left(k - \frac{\eta}{\Delta x_2} \right) \mathrm{d}\eta \tag{2.65}$$

$$= \frac{1}{\Delta x_2} \int_{-\infty}^{\infty} \left(\int_{-\infty}^{\infty} \sum_{\ell \in \mathbb{Z}} c[\ell] \cdot \varphi_1 \left(\frac{\xi}{\Delta x_1} - \ell \right) \cdot h(\eta - \xi) \mathrm{d}\xi \right) \mathring{\varphi}_2^{\top} \left(k - \frac{\eta}{\Delta x_2} \right) \mathrm{d}\eta \tag{2.66}$$

$$= \frac{1}{\Delta x_2} \sum_{\ell \in \mathbb{Z}} c[\ell] \int_{-\infty}^{\infty} \left(\int_{-\infty}^{\infty} \varphi_1 \left(\frac{\xi}{\Delta x_1} - \ell \right) \cdot h(\eta - \xi) \mathrm{d}\xi \right) \mathring{\varphi}_2^{\top} \left(k - \frac{\eta}{\Delta x_2} \right) \mathrm{d}\eta \tag{2.67}$$

$$= \frac{1}{\Delta x_2} \sum_{\ell \in \mathbb{Z}} c[\ell] \int_{-\infty}^{\infty} \left(\varphi_1 \left(\frac{\eta}{\Delta x_1} \right) \star h(\eta - \ell \Delta x_1) \right) \cdot \mathring{\varphi}_2^{\top} \left(k - \frac{\eta}{\Delta x_2} \right) \mathrm{d}\eta \tag{2.68}$$

$$= \frac{1}{\Delta x_2} \sum_{\ell \in \mathbb{Z}} c[\ell] \cdot \left(\varphi_1 \left(\frac{x}{\Delta x_1} \right) \star h(x) \star \mathring{\varphi}_2^{\top} \left(\frac{x}{\Delta x_2} \right) \right) \Big|_{x = k \Delta x_2 - \ell \Delta x_1} \tag{2.69}$$

$$= \sum_{\ell \in \mathbb{Z}} c[\ell] \cdot u[pk - q\ell] \tag{2.70}$$

where u is defined as in Theorem 1. $\qquad\qquad\qquad\qquad\qquad\qquad\qquad\qquad\square$

2.A.2   Proof of Theorem 2

The frequency response of the digital filter in Eq. (2.37) is

$$U(e^{j2\pi\nu\Delta x_1/q}) = q \sum_{m \in \mathbb{Z}} \left\{ \hat{\varphi}_1 \left(\Delta x_1 \nu - mq \right) \cdot \hat{h} \left(\nu - \frac{mq}{\Delta x_1} \right) \cdot \hat{\mathring{\varphi}}_2^{*} \left(\Delta x_2 \nu - mp \right) \right\}. \tag{2.71}$$

The corresponding Nq-point FFT vector is obtained by sampling Eq. (2.71) at $\Delta\nu = 1/(N\Delta x_1)$, yielding the expression in Eq. (2.39).

2.A.3   Proof of Theorem 3

We denote by $\mathbf{c}$ and $\mathbf{d}$ the column vectors that contain the N input and Nq/p output coefficients in GCV-FFT:

$$\mathbf{d} = \mathbf{A} \cdot \mathbf{c}, \tag{2.72}$$

$$\mathbf{A} = \mathbf{W}_{Nq/p}^{-1} \cdot \mathbf{U} \cdot \mathbf{W}_N, \tag{2.73}$$

$$\mathbf{U} = \begin{bmatrix} \mathbf{I}_{Nq/p} & \cdots & \mathbf{I}_{Nq/p} \end{bmatrix} \cdot \mathcal{D}_U \cdot \begin{bmatrix} \mathbf{I}_N \\ \vdots \\ \mathbf{I}_N \end{bmatrix}, \tag{2.74}$$

$$\mathbf{W}_N[m,n] = \exp\left(-j2\pi mn/N\right), \qquad 0 \leq m,n < N \tag{2.75}$$

$$\mathcal{D}_U[m,n] = U[m] \cdot \delta[m-n], \qquad 0 \leq m,n < Nq \tag{2.76}$$

$$\mathbf{I}_N[m,n] = \delta[m-n], \qquad 0 \leq m,n < N \tag{2.77}$$

so that $\text{rank}(\mathbf{A}) = \text{rank}(\mathbf{U})$. It can be verified that $\mathbf{U}$ is a sparse matrix having only the Nq FFT coefficients in $\mathcal{D}_U$ as its non-zero entries, and that,

$$\text{rank}(\mathbf{U}) = \sum_{r=0}^{N/p-1} \text{rank}(\mathbf{U}_r), \tag{2.78}$$

where $\mathbf{U}_r$ is as given in Eq. (2.56). This allows the pseudoinverse [8] of $\mathbf{U}$ to be calculated from smaller matrices $\mathbf{U}_r$. The pseudoinverse of $\mathbf{A}$ is given by:

$$\mathbf{A}^\dagger = \mathbf{W}_N^{-1} \cdot \mathbf{U}^\dagger \cdot \mathbf{W}_{Nq/p}, \tag{2.79}$$

and has essentially the same form as Eq. (2.73), involving up-sampling, convolution and down-sampling operations.

Chapter 3

Automatic and Anisotropic Spatial Registration for Multi-View Optical Microscopy

Abstract[3]

We present an algorithm to spatially register two volumetric datasets related via a rigid-body transform and degraded by an anisotropic point-spread-function (PSF). Registration is necessary, for example, when fusing data in multi-view microscopy. Automatic algorithms that only rely on maximizing pixel similarity, without accounting for the anisotropic image formation process, provide poor results in such applications. We propose to solve this problem by re-blurring the reference and test data with transformed forms of the PSF, in order to make them comparable, before minimizing the mean squared intensity difference between them. Our approach extends the pyramid-based sub-pixel registration algorithm proposed by Thévenaz et al., 1998 [105], that employs an improved form of the Marquardt-Levenberg algorithm. We show, via simulations, that our method

---

[3]This chapter is based on the reference [15] co-authored with K. Chan and M. Liebling.

is more accurate than the conventional approach that does not account for the PSF. We demonstrate our algorithm in practice by registering multi-view volumes of a zebrafish larva acquired using a wide-field microscope.

3.1   Introduction

Optical microscopy allows the study of living samples under conditions similar to their native state. However, the technique often suffers from anisotropic resolution owing to the image formation process, which consists of a 3D convolution operation with the imaging system's (anisotropic) point-spread-function (PSF) [90]. Despite recent advances to design instruments that exhibit nearly isotropic PSFs, many commonly used microscopes have a PSF that is more elongated in the axial direction, with wide-field microscopy having the most severe form of anisotropy, and techniques such as confocal, two-photon, and light-sheet microscopy having the least. This anisotropy translates to an axial resolution that is worse than the lateral resolution in the acquired data. Multi-view microscopy attempts to circumvent this problem by merging acquisitions from multiple tilted directions [90, 22, 44, 43, 100, 56, 17]. However, operations therein, such as multi-view fusion and deconvolution, require the volumes to be precisely registered beforehand.

Several approaches have been proposed to address this registration problem. Heintzmann *et al.* [44] presented a mostly *manual* registration algorithm that relies on an interactive selection of salient points in the input volumes, which are used as an alignment aid. However, such a manual technique tends to be both laborious and inaccurate. A second class of algorithms that can be considered *automatic* relies on fiducial markers, such as fluorescent beads, added in moderate concentration to the prepared sample [79, 103], which are subsequently detected and used for registration. Although these approaches were shown to be accurate, they require a special method of sample prepara-
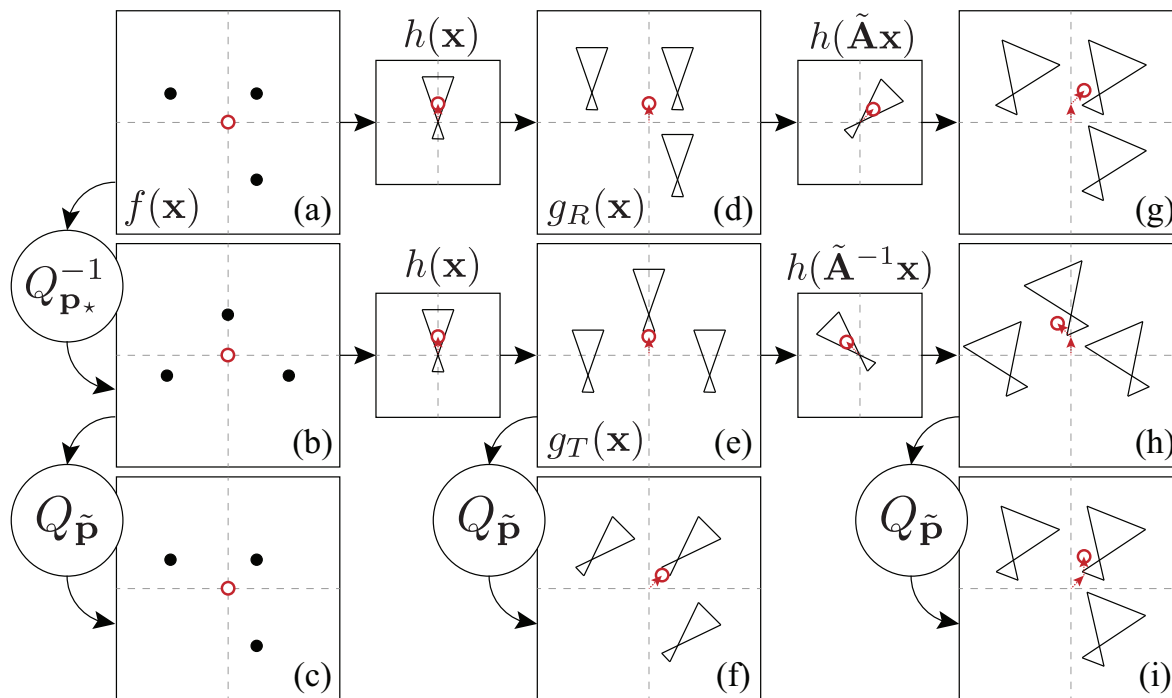
Figure 3.1: An illustration of how an anisotropic PSF affects data registration. The red circle denotes the center of mass in each case. (a-c) Registration of datasets uncorrupted by PSF. (d-f) Reference, test, and registered test, respectively. (g-i) *Cross-blurred* forms of the datasets in (d-f). Note that the center of mass coincides in (g) and (i), unlike that in (d) and (f).

tion. Moreover, the markers added can interfere with the visibility of the sample being imaged. To alleviate this problem, Krzic *et al.* [56] designed an imaging system where such fiducial markers are only used for hardware calibration, thereby averting the need to add beads along with the sample during imaging. In lieu of external markers, Keller *et al.* [50] followed a data-specific strategy to automatically detect cell nuclei and treat them as landmarks for multi-view registration. Others have used techniques such as cross-correlation [90, 22, 43, 100, 85] based on the pixel-wise similarity between datasets for registration. However, such approaches can lead to inaccuracies because they ignore the anisotropy inherent in the image formation process. A simple example is detailed

in Fig. 3.1, where a sample (Fig. 3.1(a-c)) is convolved with an anisotropic PSF. The convolution shifts the optical center of mass (and other moments) in directions within the object coordinates[4] [60] (Fig. 3.1(d-f)), leading conventional pixel-based matching methods (which would also match the center of mass) to yield a biased solution.

In this work, we propose to modify the registration cost function by *cross-blurring* the reference and test datasets (Fig. 3.1(d-f)) using PSFs tilted by the candidate transformation, so that the image volumes are comparable and identically degraded at convergence (Fig. 3.1(g-i)). We demonstrate our approach using simulations and experimental data.

The chapter is organized as follows. In Section 3.2, we describe our notations, the cost function that we wish to minimize, and our optimization strategy. In Section 3.4, we illustrate the applicability of our method on simulated and experimental datasets, and we finally conclude in Section 3.5.

3.2 Proposed Method

3.2.1 Problem Formulation

We consider a function $f(\mathbf{x})$, $\mathbf{x} \in \mathbb{R}^3$, that represents an object being imaged. We assume f undergoes a geometric transformation that can be parameterized by (i) a shearing matrix, $\mathbf{A} \in \mathbb{R}^{3\times3}$, and (ii) a translation vector, $\mathbf{b} \in \mathbb{R}^3$. We represent this using (i) a shearing operator, $A_\mathbf{A}$, and (ii) a translation operator, $T_\mathbf{b}$, defined as follows:

$$A_\mathbf{A}\left\{f\right\}(\mathbf{x}) \stackrel{\mathrm{def}}{=} f(\mathbf{A}\mathbf{x}), \tag{3.1}$$

$$T_\mathbf{b}\left\{f\right\}(\mathbf{x}) \stackrel{\mathrm{def}}{=} f(\mathbf{x}+\mathbf{b}). \tag{3.2}$$

---

[4]The effect of the PSF on the center of a mass of an imaged volume is derived in Appendix 3.A.1.

Note that rigid body transforms are a special case of affine transforms $A_{\mathbf{A}}$, when the shearing matrix $\mathbf{A}$ is a rotation matrix $\mathbf{R}_{\varphi,\theta,\psi}$, where φ, θ, and ψ represents the Euler angles[5]. We define the rotation operator $R_{\varphi,\theta,\psi}$ and its inverse $R_{\varphi,\theta,\psi}^{-1}$ as:

$$R_{\varphi,\theta,\psi}\{f\}(\mathbf{x}) \overset{\text{def}}{=} f\left(\mathbf{R}_{\varphi,\theta,\psi}\mathbf{x}\right), \tag{3.3}$$

$$R_{\varphi,\theta,\psi}^{-1}\{f\}(\mathbf{x}) \overset{\text{def}}{=} f\left(\mathbf{R}_{\varphi,\theta,\psi}^{-1}\mathbf{x}\right). \tag{3.4}$$

We jointly express the parameters $\mathbf{A}$ and $\mathbf{b}$ as $\mathbf{p} \overset{\text{def}}{=} \{p_0, p_1, \ldots, p_{M-1}\}$. For an affine transform, we have $M = 12$ parameters given by $\mathbf{p} \overset{\text{def}}{=} \{b_0, b_1, b_2, a_{00}, a_{01}, \ldots, a_{22}\}$, where b_k and $a_{k,\ell}$ denote the matrix entries $\mathbf{b}[k]$ and $\mathbf{A}[k, \ell]$, respectively. Similarly, for a rigid body transform, we have $M = 6$ parameters given by $\mathbf{p} \overset{\text{def}}{=} \{b_0, b_1, b_2, \varphi, \theta, \psi\}$[6]. We represent the sequence of transformations parameterized by $\mathbf{p}$ as:

$$Q_{\mathbf{p}}\{f\}(\mathbf{x}) \overset{\text{def}}{=} (A_{\mathbf{A}} \circ T_{\mathbf{b}} \circ f)(\mathbf{x}) \tag{3.5}$$

$$= A_{\mathbf{A}}\{T_{\mathbf{b}}\{f\}\}(\mathbf{x}) \tag{3.6}$$

$$= f(\mathbf{A}\mathbf{x} + \mathbf{b}), \tag{3.7}$$

$$Q_{\mathbf{p}}^{-1}\{f\}(\mathbf{x}) \overset{\text{def}}{=} (T_{-\mathbf{b}} \circ A_{\mathbf{A}^{-1}} \circ f)(\mathbf{x}) \tag{3.8}$$

$$= (A_{\mathbf{A}^{-1}} \circ T_{-\mathbf{A}^{-1}\mathbf{b}} \circ f)(\mathbf{x}) \tag{3.9}$$

$$= f\left(\mathbf{A}^{-1}(\mathbf{x} - \mathbf{b})\right). \tag{3.10}$$

In particular, we consider two volumes–the reference g_R and the test g_T (which is to be geometrically transformed to match g_R)–defined as follows:

$$g_R(\mathbf{x}) \overset{\text{def}}{=} (f \star h)(\mathbf{x}), \tag{3.11}$$

---

[5]The convention used for Euler angles in rigid body transformations is described in Appendix 3.A.2.

[6]The composite and norm rules for both the affine and rigid body transformations are described in Appendix 3.A.3 and 3.A.4, respectively.

$$g_T(\mathbf{x}) \stackrel{\text{def}}{=} \left(Q_{\mathbf{p}_\star}^{-1}\{f\} \star h\right)(\mathbf{x}), \tag{3.12}$$

where $\star$ denotes the convolution operation. Specifically, $\mathbf{p}_\star$ represents the unknown set of parameters ($\mathbf{A}_\star$ and $\mathbf{b}_\star$) that we wish to estimate and that characterize the geometrical transformation undergone by the object f between the acquisitions of g_R and g_T.

3.2.2 Proposed Registration Approach

The motivation of our approach stems from the fact that even if the correct geometrical transform $Q_{\mathbf{p}_\star}$ is applied to the test data g_T, the resulting volume $Q_{\mathbf{p}_\star}\{g_T\}$ will be different from the reference g_R in terms of point-wise comparison of their signal intensities. This is because the geometrical transform $Q_{\mathbf{p}_\star}$ also applies to the convolution kernel h, thus making an intensity-based similarity criterion unsuitable (Fig. 3.1(d-f)). To overcome this problem, we propose to *cross-blur* the reference and test data with each other's effective PSF before using any candidate transform $Q_{\tilde{\mathbf{p}}}$ (Fig. 3.1(g-i)).

Using Eq. (3.11) in conjunction with properties of convolution operations, the convolution between g_R and a rotated version of h can be expressed as:

$$\left(g_R \star A_{\mathbf{A}_\star}\{h\}\right)(\mathbf{x}) = \left(f \star h \star A_{\mathbf{A}_\star}\{h\}\right)(\mathbf{x}). \tag{3.13}$$

Similarly, using Eq. (3.12) and properties of affine transforms [12], applying $Q_{\mathbf{p}_\star}$ after subjecting g_T to a convolution with an inverse-rotated form of h is equivalent to[7]:

$$Q_{\mathbf{p}_\star}\left\{g_T \star A_{\mathbf{A}_\star^{-1}}\{h\}\right\}(\mathbf{x}) = |\mathbf{A}_\star| \left(Q_{\mathbf{p}_\star}\{g_T\} \star h\right)(\mathbf{x}) \tag{3.14}$$

$$= |\mathbf{A}_\star|^2 \left(f \star A_{\mathbf{A}_\star}\{h\} \star h\right)(\mathbf{x}), \tag{3.15}$$

---

[7]The effect of an affine transformation on a convolution operation is derived in Appendix 3.A.5.
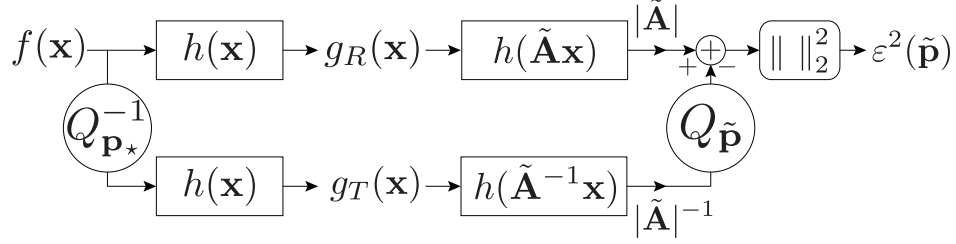
Figure 3.2: The proposed cost function ε^2 to be minimized using *cross-blurred* forms of the reference g_R and test g_T datasets.

where $|\mathbf{A}|$ denotes the determinant of the matrix $\mathbf{A}$. For the correct transform, since the *cross-blurred* volumes are equivalent except for a scaling constant (compare Eqs. (3.13) and (3.15)), we can estimate the optimal set of parameters $\mathbf{p}_\star$ via the following cost function (see also Fig. 3.2):

$$\varepsilon^2(\tilde{\mathbf{p}}) \stackrel{\text{def}}{=} \left\| |\tilde{\mathbf{A}}| \left(g_R \star A_{\tilde{\mathbf{A}}}\{h\}\right)(\mathbf{x}) - |\tilde{\mathbf{A}}|^{-1} Q_{\tilde{\mathbf{p}}} \left\{g_T \star A_{\tilde{\mathbf{A}}^{-1}}\{h\}\right\}(\mathbf{x}) \right\|_{L_2}^2, \tag{3.16}$$

$$= \frac{1}{|\tilde{\mathbf{A}}|} \left\| \left(Q_{\tilde{\mathbf{p}}}^{-1}\{g_R\} \star h\right)(\mathbf{x}) - |\tilde{\mathbf{A}}|^{-1} \left(g_T \star A_{\tilde{\mathbf{A}}^{-1}}\{h\}\right)(\mathbf{x}) \right\|_{L_2}^2, \tag{3.17}$$

where $\tilde{\mathbf{p}}$ comprises the shearing matrix $\tilde{\mathbf{A}}$ and the translation $\tilde{\mathbf{b}}$.

To estimate the optimal set of parameters $\mathbf{p}_\star$, we solve a variant of $\partial \varepsilon^2(\tilde{\mathbf{p}})/\partial \tilde{\mathbf{p}} = 0$ with an improved form of the Marquardt-Levenberg (ML) algorithm, an iterative gradient based algorithm for nonlinear least-squares optimization problems [70], using an approach similar to that proposed by Thévenaz *et al.* [105], as described in the next section.

3.3   Optimization

The Marquardt-Levenberg (ML) method is a standard technique used to solve nonlinear least squares problems, which is designed as a combination of the gradient descent and the Gauss-Newton method. Specifically, it acts more like the gradient-descent method when the parameters are far from their optimal value and resembles the Gauss-Newton

method when the parameters are almost optimal.

3.3.1   Optimization with Affine Transformation

In order to use the improved form of the ML algorithm [105], we represent $Q_{\tilde{\mathbf{p}}}$ as a combination of two transformations $Q_{\tilde{\mathbf{p}}} = Q_{\mathbf{p} \circ \Delta \mathbf{p}} = Q_{\mathbf{p}} \circ Q_{\Delta \mathbf{p}}$, where $Q_{\mathbf{p}} = A_{\mathbf{A}} \circ T_{\mathbf{b}}$ and $Q_{\Delta \mathbf{p}} = A_{\mathbf{I}+\Delta \mathbf{A}} \circ T_{\Delta \mathbf{b}}$ and rewrite the cost function in Eq. (3.16) as:

$$
\varepsilon^2(\mathbf{p} \circ \Delta \mathbf{p}) = \left\| \left| (\mathbf{I} + \Delta \mathbf{A})\mathbf{A} \right| \left(g_R \star A_{(\mathbf{I}+\Delta \mathbf{A})\mathbf{A}} \{h\} \right) (\mathbf{x}) \right.
$$
$$
\left. - \left| (\mathbf{I} + \Delta \mathbf{A})\mathbf{A} \right|^{-1} Q_{\mathbf{p} \circ \Delta \mathbf{p}} \left\{ \left(g_T \star A_{((\mathbf{I}+\Delta \mathbf{A})\mathbf{A})^{-1}} \{h\} \right) \right\} (\mathbf{x}) \right\|_{L_2}^2 \qquad (3.18)
$$
$$
= \frac{1}{|\mathbf{A}|} \left\| \left| \mathbf{I} + \Delta \mathbf{A} \right| \left(Q_{\mathbf{p}^{-1}} \{g_R\} \star A_{\mathbf{I}+\Delta \mathbf{A}} \{h\} \right) (\mathbf{x}) \right.
$$
$$
\left. - |\mathbf{A}|^{-1} \left(Q_{\Delta \mathbf{p}} \{g_T\} \star A_{\mathbf{A}^{-1}} \{h\} \right) (\mathbf{x}) \right\|_{L_2}^2 . \qquad (3.19)
$$

Specifically, instead of trying to directly minimize $\varepsilon^2(\mathbf{p})$ in Eq. (3.17), we try to find the optimal incremental update $\Delta \mathbf{p}$ by minimizing $\varepsilon^2(\mathbf{p} \circ \Delta \mathbf{p})$ with an initial guess for $\mathbf{p}$ in Eq. (3.19). This strategy is superior because the gradient of the criterion $\varepsilon^2(\mathbf{p} \circ \Delta \mathbf{p})$ with respect to $\Delta \mathbf{p}$ is independent of the initial guess $\mathbf{p}$ and is computed about a fixed point in the parameter space (unlike the gradient of $\varepsilon^2(\tilde{\mathbf{p}})$ with respect to $\tilde{\mathbf{p}}$) [105]. On a sampled spatial grid, the cost function can be approximated using the discrete norm as:

$$
\varepsilon^2(\mathbf{p} \circ \Delta \mathbf{p}) \approx \chi^2(\mathbf{p} \circ \Delta \mathbf{p}) \qquad (3.20)
$$
$$
\stackrel{\text{def}}{=} \frac{1}{|\mathbf{A}|} \sum_{i=0}^{N-1} \left| \left| \mathbf{I} + \Delta \mathbf{A} \right| \left(Q_{\mathbf{p}^{-1}} \{g_R\} \star A_{\mathbf{I}+\Delta \mathbf{A}} \{h\} \right) (\mathbf{x}_i) \right.
$$
$$
\left. - |\mathbf{A}|^{-1} \left(Q_{\Delta \mathbf{p}} \{g_T\} \star A_{\mathbf{A}^{-1}} \{h\} \right) (\mathbf{x}_i) \right|^2 , \qquad (3.21)
$$

where $\mathbf{x}_i$ denotes coordinates in the the sampled grid and N is the total number of pixels.

We can then estimate the ideal incremental update $\Delta\mathbf{p} = \{\Delta p_0, \Delta p_1, \ldots, \Delta p_{M-1}\}$ for the guess $\mathbf{p}$ by solving for:

$$
\begin{pmatrix}
(1+\lambda)\alpha_{0,0} & \alpha_{0,1} & \cdots & \alpha_{0,M-1} \\
\alpha_{1,0} & (1+\lambda)\alpha_{1,1} & \cdots & \alpha_{1,M-1} \\
\vdots & \vdots & \ddots & \vdots \\
\alpha_{M-1,0} & \alpha_{M-1,1} & \cdots & (1+\lambda)\alpha_{M-1,M-1}
\end{pmatrix}
\begin{pmatrix}
\Delta p_0 \\
\Delta p_1 \\
\vdots \\
\Delta p_{M-1}
\end{pmatrix}
\stackrel{\text{def}}{=}
\begin{pmatrix}
\beta_0 \\
\beta_1 \\
\vdots \\
\beta_{M-1}
\end{pmatrix},
\qquad (3.22)
$$

$$
\boldsymbol{\alpha}_\lambda \cdot \Delta\mathbf{p} \stackrel{\text{def}}{=} \boldsymbol{\beta}, \qquad (3.23)
$$

where β_k is proportional to the gradient and $\alpha_{k,\ell}$ is derived through the Hessian matrix calculated in the parameter space at $\Delta\mathbf{p} = 0$, similar to the approach in [105], as[8]:

$$
\beta_k \stackrel{\text{def}}{=} -\left(\frac{1}{2}\right) \frac{\partial \chi^2(\mathbf{p} \circ \Delta\mathbf{p})}{\partial \Delta p_k}\bigg|_{\Delta\mathbf{p}=\mathbf{0}}, \qquad 0 \le k < M, \qquad (3.24)
$$

$$
\alpha_{k,\ell} \stackrel{\text{def}}{=} \left(\frac{1}{2}\right) \frac{\partial^2 \chi^2(\mathbf{p} \circ \Delta\mathbf{p})}{\partial \Delta p_k \, \partial \Delta p_\ell}\bigg|_{\Delta\mathbf{p}=\mathbf{0}}, \qquad 0 \le k, \ell < M, \quad (3.25)
$$

and where $\lambda \ge 0$ determines the degree to which the update $\Delta\mathbf{p}$ conforms to a Gauss-Newton method or to a gradient-descent approach. The characteristic of ML is to adapt λ at each iteration such that λ is decreased for successful updates (where the value of the cost function has decreased) to resemble the Gauss-Newton method. Conversely, λ is increased for less successful updates to resemble the gradient-descent approach.

3.3.2   Optimization with Rigid Body Transformation

Following a similar approach as before, for the special case of rigid body transformations, we can represent $Q_{\tilde{\mathbf{p}}}$ as a combination of two transformations $Q_{\tilde{\mathbf{p}}} = Q_{\mathbf{p} \circ \Delta\mathbf{p}} =$

---

[8]The gradient and Hessian matrix values are derived for affine transformations in Appendix 3.A.6.

$Q_{\mathbf{p}} \circ Q_{\Delta\mathbf{p}}$, where $Q_{\mathbf{p}} = R_{\varphi,\theta,\psi} \circ T_{\mathbf{b}}$ and $Q_{\Delta\mathbf{p}} = R_{\Delta\varphi,\Delta\theta,\Delta\psi} \circ T_{\Delta\mathbf{b}}$, and rewrite the cost function in Eq. (3.16) as (ignoring the determinants, since they are equal to unity for rigid body transformations):

$$\varepsilon^2(\mathbf{p} \circ \Delta\mathbf{p}) = \left\| (g_R \star R_{\varphi,\theta,\psi} \{R_{\Delta\varphi,\Delta\theta,\Delta\psi} \{h\}\}) (\mathbf{x}) - (Q_{\mathbf{p}\circ\Delta\mathbf{p}} \{g_T\} \star h) (\mathbf{x}) \right\|_{L_2}^2, \quad (3.26)$$

$$= \left\| (Q_{\mathbf{p}^{-1}} \{g_R\} \star R_{\Delta\varphi,\Delta\theta,\Delta\psi} \{h\}) (\mathbf{x}) - (Q_{\Delta\mathbf{p}} \{g_T\} \star R_{\varphi,\theta,\psi}^{-1} \{h\}) (\mathbf{x}) \right\|_{L_2}^2,$$
$$(3.27)$$

which can be approximated on a sampled spatial grid using the discrete norm as:

$$\chi^2(\mathbf{p} \circ \Delta\mathbf{p}) = \sum_{i=0}^{N-1} \left| (Q_{\mathbf{p}^{-1}} \{g_R\} \star R_{\Delta\varphi,\Delta\theta,\Delta\psi} \{h\}) (\mathbf{x}_i) - (Q_{\Delta\mathbf{p}} \{g_T\} \star R_{\varphi,\theta,\psi}^{-1} \{h\}) (\mathbf{x}_i) \right|^2.$$
$$(3.28)$$

We can compute the gradient and Hessian matrix values[9] as in Eqs. (3.24) and (3.25) in the parameter space at $\Delta\mathbf{p} = 0$, similar to the approach in [105].

3.3.3   Multi-resolution Processing

Following the approach proposed by Thevenaz *et al.* [105], we employ a multi-resolution approach by using a dyadic pyramid based on cubic B-splines to represent the volumes in shift-invariant (SI) spaces V_k at multiple scales k, $0 \leq k < J$. Following a coarse-to-fine strategy, the algorithm first achieves a quick registration based on the large-scale features in the data, and subsequently makes changes for progressively finer details. This is advantageous with respect to both computation time and robustness against local minima, especially since computations (and convolutions during re-blurring) are in 3D. We consider the routine to have converged at each scale when the total relative change in the parameters has dropped below a set threshold, as illustrated in Algorithm 3.1. Since

---

[9]The gradient and Hessian matrix values are derived for rigid transformations in Appendix 3.A.7.

the method is implemented by a multi-resolution approach, the gradient and Hessian matrices have to be computed at each resolution level and the transformation parameters need to be propagated between the levels, as described in Appendix 3.A.8.

Algorithm 3.1 Proposed PSF-aware form of the improved ML algorithm

1: **Input:** $g_T(\mathbf{x})$, $g_R(\mathbf{x})$, $h(\mathbf{x})$, $\mathbf{p}$ (initial guess), λ
2: **Initial condition:** $\tilde{\mathbf{p}} \leftarrow \mathbf{p}$;
3: **for** $k =$ coarsest to finest scale **do**
4:      Retrieve parameters $\tilde{\mathbf{p}}$ corresponding to present scale;
5:      Compute $g_R^{V_k}$, $g_T^{V_k}$, and h^{V_k} (orthogonal projection onto SI B-spline space V_k);
6:      $\chi^2(\tilde{\mathbf{p}}) \leftarrow \sum_{i=0}^{N-1} \left| |\tilde{\mathbf{A}}| \left(g_R^{V_k} \star A_{\tilde{\mathbf{A}}} \left\{ h^{V_k} \right\} \right) (\mathbf{x}_i) - \left(Q_{\tilde{\mathbf{p}}} \left\{ g_T^{V_k} \right\} \star h^{V_k} \right) (\mathbf{x}_i) \right|^2$;
7:      **if** convergence is achieved **then**
8:          **if** finest scale **then**
9:              return **Output**;
10:         **else**
11:             Go to next finer level;
12:         **end if**
13:     **else**
14:         **if** $\chi^2(\tilde{\mathbf{p}})$ has reduced from previous iteration **then**
15:             Decrease λ (to resemble the Guass-Newton approach);
16:             $\mathbf{p} \leftarrow \tilde{\mathbf{p}}$ (update the initial guess of parameters);
17:         **else**
18:             Increase λ (to resemble the gradient-descent approach);
19:         **end if**
20:         Compute Hessian and gradient matrices $\boldsymbol{\alpha}_\lambda$ and $\boldsymbol{\beta}$;
21:         Solve for $\Delta\mathbf{p}$ in $\boldsymbol{\alpha}_\lambda \cdot \Delta\mathbf{p} = \boldsymbol{\beta}$;
22:         Use composite rules to update parameters $\tilde{\mathbf{p}} \leftarrow \mathbf{p} \circ \Delta\mathbf{p}$;
23:         Repeat from step 6 to calculate new value of cost function;
24:     **end if**
25: **end for**
26: **Output:** $Q_{\tilde{\mathbf{p}}} \left\{ g_T \right\} (\mathbf{x})$

3.4   Experiments

3.4.1   Validation with Simulated Data

For validation purposes, we considered a synthetic dataset consisting of six parallel hollow bars [41] (Fig. 3.3(a-b)) as our uncorrupted volume, f. We then used a software package [52] to generate a Gibson & Lanni 3D PSF model [36] (Fig. 3.3(c)), h, applicable for wide-field microscopes, with the following parameters: immersion refractive index = 1 (air), sample refractive index = 1.33, numerical aperture (NA) = 0.7, working distance = 2 mm, particle position = 0 μm, sampling step $\Delta x = \Delta y = \Delta z = 0.5\mu$m, excitation wavelength = 495 nm, and emission wavelength = 509 nm. Using f and h, we generated the reference g_R (Fig. 3.3(d)). Next, we rotated f by an angle of 30 about the x-axis, and translated it by a vector $[b_0, b_0, b_1]^\top$, where b_0, b_0, and b_1 were chosen from a uniform distribution between 0 and 5, and finally convolved it with h to form g_T (Fig. 3.3(e)). With an initial guess equal to the identity transformation, we then attempted to estimate $\mathbf{p}_\star$ using two different approaches: (i) using the PSF ignorant form of the improved ML algorithm [105] (*i.e* assuming $h(\mathbf{x}) = \delta(\mathbf{x})$), and (ii) using our proposed algorithm. The simulation was run over 10 random instances, and the mean error in the estimated angle was found to be 11.55 using the traditional approach, and 1.71 using our proposed algorithm. Examples of the registered results obtained using the two algorithms are shown in Fig. 3.3(f) and (g), respectively. We repeated this experiment by also using a Gaussian approximation of the PSF corresponding to a disk scanning confocal microscope [120] with NA = 0.3, pinhole radius = 5 Airy units, and similar parameters as before. For this case, the mean error in the estimated angle was recorded as 5.69 using the traditional approach, and 0.39 using our proposed algorithm.
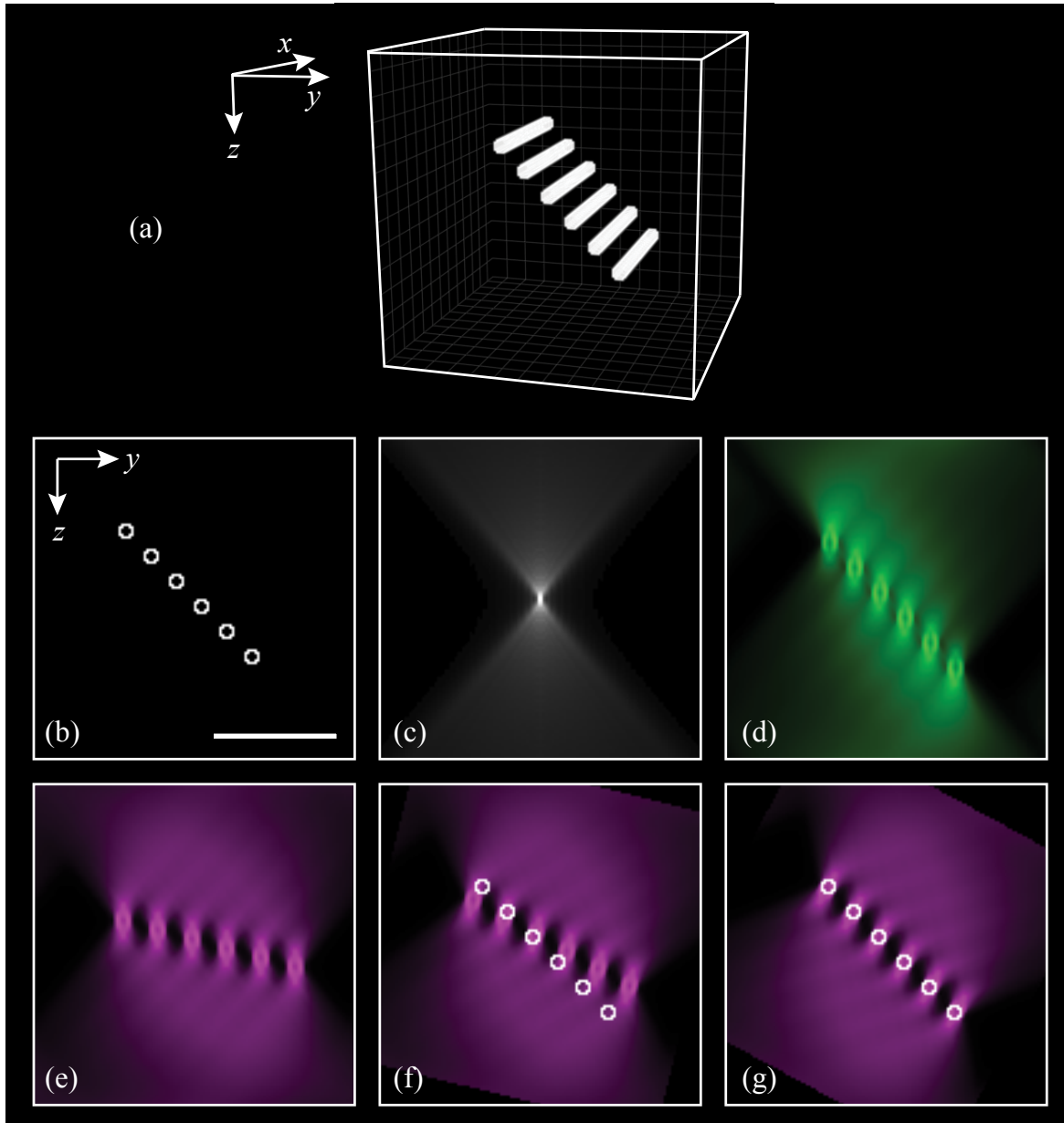
Figure 3.3: (a) 3D perspective of the object used in simulations. (b-g) Maximum intensity projection (MIP) in the yz plane of f, h (after gamma-correction of $\gamma = 0.3$), g_R, g_T, the registered results using the traditional, and our proposed approach, respectively. For comparison, (b) has been overlaid on the registered results shown in (f) and (g). Scale bar is $25\mu m$.
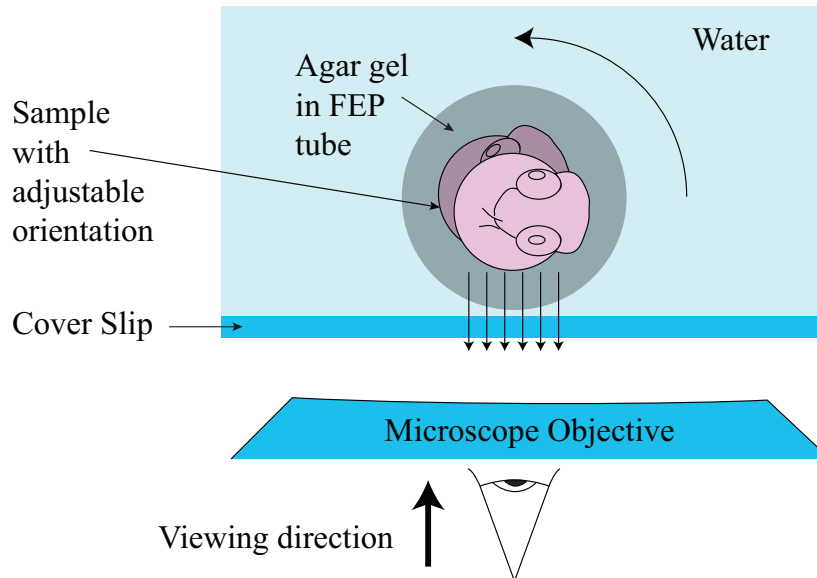
Figure 3.4: An illustration of the multi-view acquisition setup where the zerbrafish sample is placed inside an FEP tube filled with agar gel and placed within a chamber of water, with the tube being connected to a stepper motor in order to be rotated.

3.4.2   Illustration with Experimentally Acquired Data

To prove the applicability of our approach for experimental datasets, we used an inverted wide-field microscope equipped with a $10\times/0.3$ dry objective to acquire 3D volumes of a 25-hpf (hours post-fertilization)-old transgenic zebrafish larva (*Tg(fli1a:EGFP)*), which expresses green fluorescent protein in the vasculature. We inserted the larva in a tube made from fluorinated ethylene propylene (FEP), whose refractive index is close to that of water, and rotated the tube using a stepper motor for six multi-view acquisitions (Figs. 3.4, 3.5(d)). Treating the first volume as the reference, we recursively registered each subsequent dataset to its aligned predecessor. The registered form of the final volume is shown together with the first reference in Fig. 3.5(a-c). The results demonstrate that despite the anisotropic resolution, characteristic of wide-field microscopy, our approach correctly matches the curvature and bright features of the vasculature, without erroneously matching the dominant blur.

Figure 3.5: (a-c) MIP of the first volume (green) and the recursively registered final volume (magenta) (originally acquired after a rotation of about 90 about th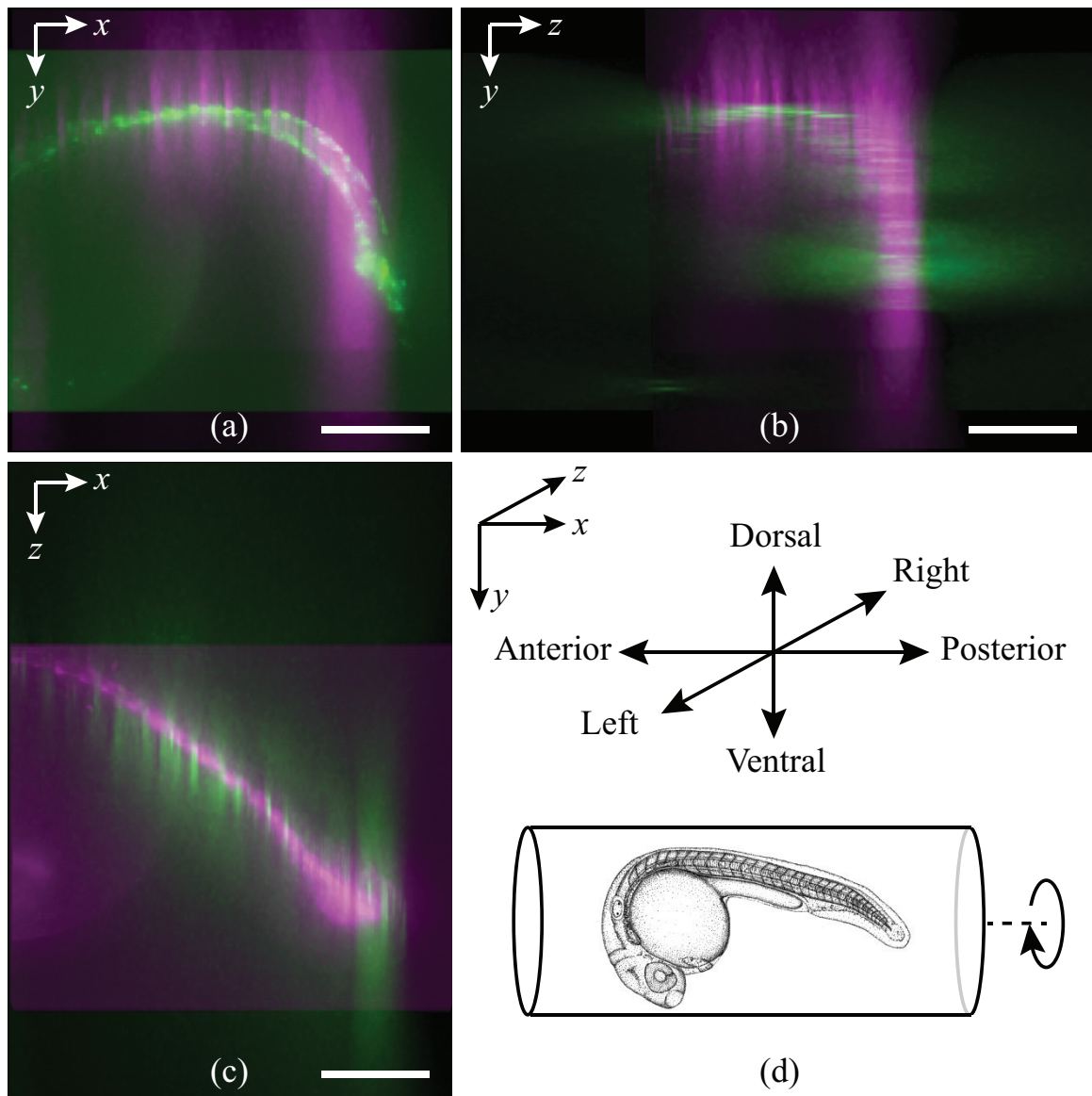e x-axis) in the xy, yz, and xz planes, respectively. (d) A schematic representation showing the relative position of the sample and the axis of rotation in our experimental setup. Scale bar is $200\mu m$.

3.5   Conclusion

We have derived an automatic intensity-based registration routine and have demonstrated its suitability for aligning volumes that were acquired using imaging systems with severely anisotropic PSFs. The simulation results, which showed an accuracy of around an order of magnitude over the traditional scheme, demonstrates the benefits of such an approach that integrates the imaging model. The good alignment we observed using multi-view volumes from a wide-field microscope, whose PSF anisotropy is particularly strong, confirms our method's potential for applications in multi-view microscopy.

3.A   Appendix

3.A.1   Effect of PSF on Center of Mass

Consider a signal that is the result of an analog convolution operation $g(\mathbf{x}) \stackrel{\text{def}}{=} (f \star h)(\mathbf{x})$, where $\mathbf{x} \in \mathbb{R}^3$. The abscissa of its center of mass is defined as:

$$\langle x \rangle_g \stackrel{\text{def}}{=} \frac{\iiint_{\mathbb{R}^3} x \cdot g(\mathbf{x}) \mathrm{d}\mathbf{x}}{\iiint_{\mathbb{R}^3} g(\mathbf{x}) \mathrm{d}\mathbf{x}}. \tag{3.29}$$

Using the substitution $g_0(\mathbf{x}) = x \cdot g(\mathbf{x})$ and the properties of Fourier transforms, we have:

$$\langle x \rangle_g \stackrel{\text{def}}{=} \frac{\iiint_{\mathbb{R}^3} g_0(\mathbf{x}) \mathrm{d}\mathbf{x}}{\iiint_{\mathbb{R}^3} g(\mathbf{x}) \mathrm{d}\mathbf{x}} \tag{3.30}$$

$$= \frac{\hat{g}_0(0)}{\hat{f}(0) \cdot \hat{h}(0)} \tag{3.31}$$

$$= \left(\frac{1}{\hat{f}(0) \cdot \hat{h}(0)} \right) \left(\frac{j}{2\pi} \right) \left(\frac{\partial \hat{g}(\mathbf{u})}{\partial u} \bigg|_{\mathbf{u}=0} \right) \tag{3.32}$$

$$= \left(\frac{1}{\hat{f}(0) \cdot \hat{h}(0)} \right) \left(\frac{j}{2\pi} \right) \left(\frac{\partial \left(\hat{f}(\mathbf{u}) \cdot \hat{h}(\mathbf{u}) \right)}{\partial u} \bigg|_{\mathbf{u}=0} \right) \tag{3.33}$$

$$= \left(\frac{1}{\hat{f}(0)} \right) \left(\frac{j}{2\pi} \right) \left(\frac{\partial \hat{f}(\mathbf{u})}{\partial u} \bigg|_{\mathbf{u}=0} \right) + \left(\frac{1}{\hat{h}(0)} \right) \left(\frac{j}{2\pi} \right) \left(\frac{\partial \hat{h}(\mathbf{u})}{\partial u} \bigg|_{\mathbf{u}=0} \right) \tag{3.34}$$

$$= \frac{\iiint_{\mathbb{R}^3} x \cdot f(\mathbf{x}) \mathrm{d}\mathbf{x}}{\iiint_{\mathbb{R}^3} f(\mathbf{x}) \mathrm{d}\mathbf{x}} + \frac{\iiint_{\mathbb{R}^3} x \cdot h(\mathbf{x}) \mathrm{d}\mathbf{x}}{\iiint_{\mathbb{R}^3} h(\mathbf{x}) \mathrm{d}\mathbf{x}} \tag{3.35}$$

$$\stackrel{\text{def}}{=} \langle x \rangle_f + \langle x \rangle_h, \tag{3.36}$$

i.e. the centers of abscissa of the center of mass add up in a convolution operation.

3.A.2   Euler Angle Conventions

Using a right-handed coordinate system with positive angles in the anti-clockwise direction, we use the following convention for matrices characterizing the Euler angles:

$$\mathbf{R}_\varphi^x \stackrel{\text{def}}{=} \begin{pmatrix} 1 & 0 & 0 \\ 0 & \cos(\varphi) & -\sin(\varphi) \\ 0 & \sin(\varphi) & \cos(\varphi) \end{pmatrix} \tag{3.37}$$

$$\mathbf{R}_\theta^y \stackrel{\text{def}}{=} \begin{pmatrix} \cos(\theta) & 0 & \sin(\theta) \\ 0 & 1 & 0 \\ -\sin(\theta) & 0 & \cos(\theta) \end{pmatrix} \tag{3.38}$$

$$\mathbf{R}_\psi^z \stackrel{\text{def}}{=} \begin{pmatrix} \cos(\psi) & -\sin(\psi) & 0 \\ \sin(\psi) & \cos(\psi) & 0 \\ 0 & 0 & 1 \end{pmatrix} \tag{3.39}$$

$$\mathbf{R}_{\varphi,\theta,\psi} \stackrel{\text{def}}{=} \mathbf{R}_\varphi^x \times \mathbf{R}_\theta^y \times \mathbf{R}_\psi^z. \tag{3.40}$$

3.A.3 Composite Rules for Affine and Rigid Transformations

The consecutive application of affine transformations can be combined as follows:

$$(T_{\mathbf{b}} \circ T_{\mathbf{a}} \circ f)(\mathbf{x}) = (T_{\mathbf{a}+\mathbf{b}} \circ f)(\mathbf{x}), \tag{3.41}$$

$$(T_{\mathbf{b}} \circ A_{\mathbf{A}} \circ f)(\mathbf{x}) = (A_{\mathbf{A}} \circ T_{\mathbf{Ab}} \circ f)(\mathbf{x}), \tag{3.42}$$

$$(A_{\mathbf{A}} \circ T_{\mathbf{b}} \circ f)(\mathbf{x}) = (T_{\mathbf{A}^{-1}\mathbf{b}} \circ A_{\mathbf{A}} \circ f)(\mathbf{x}), \tag{3.43}$$

$$(A_{\mathbf{B}} \circ A_{\mathbf{A}} \circ f)(\mathbf{x}) = (A_{\mathbf{AB}} \circ f)(\mathbf{x}). \tag{3.44}$$

Two consecutive 3D rotations can be combined as a single rotation as:

$$(R_{\varphi_2,\theta_2,\psi_2} \circ R_{\varphi_1,\theta_1,\psi_1} \circ f)(\mathbf{x}) \stackrel{\text{def}}{=} (R_{\varphi_3,\theta_3,\psi_3} \circ f)(\mathbf{x}), \tag{3.45}$$

where

$$\theta_3 \stackrel{\text{def}}{=} \sin^{-1}\left(\alpha_0 \cos(\theta_2) + \sin(\theta_2)\cos(\theta_1)\cos(\psi_1)\right), \tag{3.46}$$

$$\psi_3 \stackrel{\text{def}}{=} \sin^{-1}\left(\frac{\sin(\psi_2)}{\cos(\theta_3)}\left(\cos(\theta_2)\cos(\theta_1)\cos(\psi_1) - \alpha_0\sin(\theta_2)\right) - \alpha_1\frac{\cos(\psi_2)}{\cos(\theta_3)}\right), \tag{3.47}$$

$$\varphi_3 \stackrel{\text{def}}{=} \sin^{-1}\left(\frac{\cos(\theta_2)}{\cos(\theta_3)}\left(\cos(\varphi_2)\sin(\varphi_1)\cos(\theta_1) + \alpha_2\sin(\varphi_1)\right) - \alpha_3\frac{\sin(\theta_1)}{\cos(\theta_3)}\right), \tag{3.48}$$

$$\alpha_0 \stackrel{\text{def}}{=} \cos(\varphi_2)\sin(\theta_1) + \sin(\varphi_2)\cos(\theta_1)\sin(\psi_1), \tag{3.49}$$

$$\alpha_1 \stackrel{\text{def}}{=} \sin(\varphi_2)\sin(\theta_1) - \cos(\varphi_2)\cos(\theta_1)\sin(\psi_1), \tag{3.50}$$

$$\alpha_2 \stackrel{\text{def}}{=} \cos(\varphi_1)\cos(\psi_1) - \sin(\psi_1)\sin(\theta_1)\sin(\psi_1), \tag{3.51}$$

$$\alpha_3 \stackrel{\text{def}}{=} \cos(\varphi_1)\sin(\psi_1) + \sin(\varphi_1)\sin(\theta_1)\cos(\varphi_1). \tag{3.52}$$

Two transformations $Q_{\Delta\mathbf{p}} \stackrel{\text{def}}{=} A_{\mathbf{I}+\Delta\mathbf{A}} \circ T_{\Delta\mathbf{b}}$ and $Q_{\mathbf{p}} \stackrel{\text{def}}{=} A_{\mathbf{A}} \circ T_{\mathbf{b}}$ can be combined as:

$$(Q_{\mathbf{p}} \circ Q_{\Delta\mathbf{p}} \circ f)(\mathbf{x}) \stackrel{\text{def}}{=} (Q_{\tilde{\mathbf{p}}} \circ f)(\mathbf{x}), \tag{3.53}$$

where $Q_{\tilde{\mathbf{p}}} \stackrel{\text{def}}{=} A_{\tilde{\mathbf{A}}} \circ T_{\tilde{\mathbf{b}}}$ is characterized by:

$$\tilde{\mathbf{A}} = (\mathbf{I} + \Delta\mathbf{A})\mathbf{A}, \tag{3.54}$$

$$\tilde{\mathbf{b}} = (\mathbf{I} + \Delta\mathbf{A})\mathbf{b} + \Delta\mathbf{b}. \tag{3.55}$$

3.A.4 Norm Rules for Affine and Rigid Transformations

The norm of any given signal is affected by affine and rigid body transformations as:

$$\left\| T_{\mathbf{b}} \left\{ f \right\} (\mathbf{x}) \right\|_{L_2}^2 = \left\| f(\mathbf{x}) \right\|_{L_2}^2, \tag{3.56}$$

$$\left\| A_{\mathbf{A}} \left\{ f \right\} (\mathbf{x}) \right\|_{L_2}^2 = \frac{1}{|\mathbf{A}|} \left\| f(\mathbf{x}) \right\|_{L_2}^2, \tag{3.57}$$

$$\left\| R_{\varphi,\theta,\psi} \left\{ f \right\} (\mathbf{x}) \right\|_{L_2}^2 = \left\| f(\mathbf{x}) \right\|_{L_2}^2. \tag{3.58}$$

Therefore, for general affine transformations,

$$\left\| Q_{\mathbf{p}} \left\{ f \right\} (\mathbf{x}) \right\|_{L_2}^2 = \left\| A_{\mathbf{A}} \left\{ T_{\mathbf{b}} \left\{ f \right\} \right\} (\mathbf{x}) \right\|_{L_2}^2 = \frac{1}{|\mathbf{A}|} \left\| T_{\mathbf{b}} \left\{ f \right\} (\mathbf{x}) \right\|_{L_2}^2 = \frac{1}{|\mathbf{A}|} \left\| f(\mathbf{x}) \right\|_{L_2}^2, \tag{3.59}$$

while for rigid body transformations,

$$\left\| Q_{\mathbf{p}} \left\{ f \right\} (\mathbf{x}) \right\|_{L_2}^2 = \left\| R_{\varphi,\theta,\psi} \left\{ T_{\mathbf{b}} \left\{ f \right\} \right\} (\mathbf{x}) \right\|_{L_2}^2 = \left\| T_{\mathbf{b}} \left\{ f \right\} (\mathbf{x}) \right\|_{L_2}^2 = \left\| f(\mathbf{x}) \right\|_{L_2}^2. \tag{3.60}$$

3.A.5   Affine Transform of a Convolution Operation

Consider the affine transform $Q_\mathbf{p} \overset{\text{def}}{=} A_\mathbf{A} \circ T_\mathbf{b}$ characterized by the parameters $\mathbf{p} : \mathbf{A} \in \mathbb{R}^{3\times3}, \mathbf{b} \in \mathbb{R}^{3\times1}$ applied to a 3D coordinate system $\mathbf{x} \in \mathbb{R}^3$:

$$\mathbf{x}' \overset{\text{def}}{=} \mathbf{A}\mathbf{x} + \mathbf{b}. \tag{3.61}$$

Given a signal, $g(\mathbf{x})$, and its affine transformed form, $Q_\mathbf{p}\{g\}(\mathbf{x}) = g(\mathbf{x}')$, the 3D Fourier transform of $Q_\mathbf{p}\{g\}$, denoted as $\hat{Q}_\mathbf{p}\{g\}$, can be calculated as:

$$\hat{Q}_\mathbf{p}\{g\}(\mathbf{u}) \overset{\text{def}}{=} \iiint_{\mathbb{R}^3} Q_\mathbf{p}\{g\}(\mathbf{x}) \cdot \exp(-j2\pi\mathbf{u}^\top\mathbf{x})\mathrm{d}\mathbf{x} \tag{3.62}$$

$$= \frac{1}{|\mathbf{A}|} \iiint_{\mathbb{R}^3} g(\mathbf{x}') \cdot \exp(-j2\pi\mathbf{u}^\top\mathbf{A}^{-1}(\mathbf{x}' - \mathbf{b}))\mathrm{d}\mathbf{x}' \tag{3.63}$$

$$= \frac{1}{|\mathbf{A}|} \exp(j2\pi\mathbf{u}^\top\mathbf{A}^{-1}\mathbf{b}) \cdot \hat{g}\left(\left(\mathbf{A}^{-1}\right)^\top \mathbf{u}\right). \tag{3.64}$$

If $g(\mathbf{x}) \overset{\text{def}}{=} (f \star h)(\mathbf{x})$, then $\hat{g}(\mathbf{u}) = \hat{f}(\mathbf{u}) \cdot \hat{h}(\mathbf{u})$. Therefore, we have:

$$\hat{Q}_\mathbf{p}\{g\}(\mathbf{u}) = \frac{1}{|\mathbf{A}|} \exp(j2\pi\mathbf{u}^\top\mathbf{A}^{-1}\mathbf{b}) \cdot \hat{f}\left(\left(\mathbf{A}^{-1}\right)^\top \mathbf{u}\right) \cdot \hat{h}\left(\left(\mathbf{A}^{-1}\right)^\top \mathbf{u}\right) \tag{3.65}$$

$$= \hat{Q}_\mathbf{p}\{f\}(\mathbf{u}) \cdot \hat{h}\left(\left(\mathbf{A}^{-1}\right)^\top \mathbf{u}\right), \tag{3.66}$$

which implies the following:

$$\mathbf{g}(\mathbf{A}\mathbf{x} + \mathbf{b}) = |\mathbf{A}| \cdot (f(\mathbf{A}\mathbf{x} + \mathbf{b}) \star h(\mathbf{A}\mathbf{x})), \tag{3.67}$$

$$\text{i.e.} \quad Q_\mathbf{p}\{(f \star h)\}(\mathbf{x}) = |\mathbf{A}| \cdot (Q_\mathbf{p}\{f\}(\mathbf{x}) \star A_\mathbf{A}\{h\}(\mathbf{x})). \tag{3.68}$$

3.A.6 Gradient and Hessian Matrix for Affine Transformations

The gradient β_k and Hessian matrix $\alpha_{k,\ell}$ calculated in the parameter space at $\Delta\mathbf{p} = 0$ can be calculated as (ignoring similar constants and second derivative terms):

$$\beta_k \stackrel{\text{def}}{=} -\left(\frac{1}{2}\right) \frac{\partial\chi^2(\mathbf{p}\circ\Delta\mathbf{p})}{\partial\Delta p_k}\bigg|_{\Delta\mathbf{p}=\mathbf{0}}, \qquad\qquad 0 \leq k < M, \quad (3.69)$$

$$= -\sum_{i=0}^{N-1} \left((Q_{\mathbf{p}^{-1}}\{g_R\}\star h)(\mathbf{x}_i) - |\mathbf{A}|^{-1}(g_T \star A_{\mathbf{A}^{-1}}\{h\})(\mathbf{x}_i)\right)$$
$$\left(\frac{\partial|\mathbf{I}+\Delta\mathbf{A}|}{\partial\Delta p_k}(Q_{\mathbf{p}^{-1}}\{g_R\}\star h)(\mathbf{x}_i) + \left(Q_{\mathbf{p}^{-1}}\{g_R\}\star\frac{\partial A_{\mathbf{I}+\Delta\mathbf{A}}\{h\}}{\partial\Delta p_k}\right)(\mathbf{x}_i)\right.$$
$$\left.-|\mathbf{A}|^{-1}\left(\frac{\partial Q_{\Delta\mathbf{p}}\{g_T\}}{\partial\Delta p_k}\star A_{\mathbf{A}^{-1}}\{h\}\right)(\mathbf{x}_i)\right), \qquad\qquad (3.70)$$

$$\alpha_{k,\ell} \stackrel{\text{def}}{=} \left(\frac{1}{2}\right) \frac{\partial^2\chi^2(\mathbf{p}\circ\Delta\mathbf{p})}{\partial\Delta p_k\partial\Delta p_\ell}\bigg|_{\Delta\mathbf{p}=\mathbf{0}}, \qquad\qquad 0 \leq k,\ell < M, \quad (3.71)$$

$$= \sum_{i=0}^{N-1} \left(\frac{\partial|\mathbf{I}+\Delta\mathbf{A}|}{\partial\Delta p_\ell}(Q_{\mathbf{p}^{-1}}\{g_R\}\star h)(\mathbf{x}_i) + \left(Q_{\mathbf{p}^{-1}}\{g_R\}\star\frac{\partial A_{\mathbf{I}+\Delta\mathbf{A}}\{h\}}{\partial\Delta p_\ell}\right)(\mathbf{x}_i)\right.$$
$$\left.-|\mathbf{A}|^{-1}\left(\frac{\partial Q_{\Delta\mathbf{p}}\{g_T\}}{\partial\Delta p_\ell}\star A_{\mathbf{A}^{-1}}\{h\}\right)(\mathbf{x}_i)\right)$$
$$\left(\frac{\partial|\mathbf{I}+\Delta\mathbf{A}|}{\partial\Delta p_k}(Q_{\mathbf{p}^{-1}}\{g_R\}\star h)(\mathbf{x}_i) + \left(Q_{\mathbf{p}^{-1}}\{g_R\}\star\frac{\partial A_{\mathbf{I}+\Delta\mathbf{A}}\{h\}}{\partial\Delta p_k}\right)(\mathbf{x}_i)\right.$$
$$\left.-|\mathbf{A}|^{-1}\left(\frac{\partial Q_{\Delta\mathbf{p}}\{g_T\}}{\partial\Delta p_k}\star A_{\mathbf{A}^{-1}}\{h\}\right)(\mathbf{x}_i)\right)$$
$$+\left((Q_{\mathbf{p}^{-1}}\{g_R\}\star h)(\mathbf{x}_i) - |\mathbf{A}|^{-1}(g_T\star A_{\mathbf{A}^{-1}}\{h\})(\mathbf{x}_i)\right)$$
$$\left(\frac{\partial^2|\mathbf{I}+\Delta\mathbf{A}|}{\partial\Delta p_k\partial\Delta p_\ell}(Q_{\mathbf{p}^{-1}}\{g_R\}\star h)(\mathbf{x}_i)\right) \qquad\qquad (3.72)$$

3.A.6.1   Derivatives of Affine Transformed Volume w.r.t. Parameters

Consider the affine transform $Q_{\Delta\mathbf{p}} \stackrel{\text{def}}{=} A_{\mathbf{I}+\Delta\mathbf{A}} \circ T_{\Delta\mathbf{b}}$ characterized by the parameters $\Delta\mathbf{p} : \Delta\mathbf{A} \in \mathbb{R}^{3\times3}, \Delta\mathbf{b} \in \mathbb{R}^{3\times1}$ applied to a 3D coordinate system, $\mathbf{x} \in \mathbb{R}^3$:

$$\mathbf{x}' \stackrel{\text{def}}{=} (\mathbf{I}+\Delta\mathbf{A})\mathbf{x} + \Delta\mathbf{b} = \begin{pmatrix} 1+\Delta a_{00} & \Delta a_{01} & \Delta a_{02} \\ \Delta a_{10} & 1+\Delta a_{11} & \Delta a_{12} \\ \Delta a_{20} & \Delta a_{21} & 1+\Delta a_{22} \end{pmatrix} \begin{pmatrix} x \\ y \\ z \end{pmatrix} + \begin{pmatrix} \Delta b_0 \\ \Delta b_1 \\ \Delta b_2 \end{pmatrix}. \quad (3.73)$$

Given a signal, $g(\mathbf{x})$, the derivatives of its affine transformed form $Q_{\Delta\mathbf{p}}\{g\}(\mathbf{x}) = g(\mathbf{x}')$ with respect to each of the 12 parameters in $\Delta\mathbf{p}$, computed at $\Delta\mathbf{p} = 0$, is essential for the improved ML algorithm. For example,

$$\frac{\partial Q_{\Delta\mathbf{p}}\{g_T\}(\mathbf{x})}{\partial \Delta b_0} = \frac{\partial g_T(\mathbf{x}')}{\partial x'} \cdot \frac{\partial x'}{\partial \Delta b_0} + \frac{\partial g_T(\mathbf{x}')}{\partial y'} \cdot \frac{\partial y'}{\partial \Delta b_0} + \frac{\partial g_T(\mathbf{x}')}{\partial z'} \cdot \frac{\partial z'}{\partial \Delta b_0}. \quad (3.74)$$

At $\Delta\mathbf{p} = \mathbf{0}$, the derivatives with respect to all the 12 parameters can be computed as:

$$\left.\frac{\partial Q_{\Delta\mathbf{p}}\{g_T\}(\mathbf{x})}{\partial \Delta b_0}\right|_{\Delta\mathbf{p}=0} = \frac{\partial g_T(\mathbf{x})}{\partial x} \quad (3.75)$$

$$\left.\frac{\partial Q_{\Delta\mathbf{p}}\{g_T\}(\mathbf{x})}{\partial \Delta b_1}\right|_{\Delta\mathbf{p}=0} = \frac{\partial g_T(\mathbf{x})}{\partial y} \quad (3.76)$$

$$\left.\frac{\partial Q_{\Delta\mathbf{p}}\{g_T\}(\mathbf{x})}{\partial \Delta b_2}\right|_{\Delta\mathbf{p}=0} = \frac{\partial g_T(\mathbf{x})}{\partial z} \quad (3.77)$$

$$\left.\frac{\partial Q_{\Delta\mathbf{p}}\{g_T\}(\mathbf{x})}{\partial \Delta a_{00}}\right|_{\Delta\mathbf{p}=0} = x\frac{\partial g_T(\mathbf{x})}{\partial x} \quad (3.78)$$

$$\left.\frac{\partial Q_{\Delta\mathbf{p}}\{g_T\}(\mathbf{x})}{\partial \Delta a_{01}}\right|_{\Delta\mathbf{p}=0} = y\frac{\partial g_T(\mathbf{x})}{\partial x} \quad (3.79)$$

$$\left.\frac{\partial Q_{\Delta\mathbf{p}}\{g_T\}(\mathbf{x})}{\partial \Delta a_{02}}\right|_{\Delta\mathbf{p}=0} = z\frac{\partial g_T(\mathbf{x})}{\partial x} \quad (3.80)$$

$$\left.\frac{\partial Q_{\Delta\mathbf{p}}\{g_T\}(\mathbf{x})}{\partial \Delta a_{10}}\right|_{\Delta\mathbf{p}=0} = x\frac{\partial g_T(\mathbf{x})}{\partial y} \tag{3.81}$$

$$\left.\frac{\partial Q_{\Delta\mathbf{p}}\{g_T\}(\mathbf{x})}{\partial \Delta a_{11}}\right|_{\Delta\mathbf{p}=0} = y\frac{\partial g_T(\mathbf{x})}{\partial y} \tag{3.82}$$

$$\left.\frac{\partial Q_{\Delta\mathbf{p}}\{g_T\}(\mathbf{x})}{\partial \Delta a_{12}}\right|_{\Delta\mathbf{p}=0} = z\frac{\partial g_T(\mathbf{x})}{\partial y} \tag{3.83}$$

$$\left.\frac{\partial Q_{\Delta\mathbf{p}}\{g_T\}(\mathbf{x})}{\partial \Delta a_{20}}\right|_{\Delta\mathbf{p}=0} = x\frac{\partial g_T(\mathbf{x})}{\partial z} \tag{3.84}$$

$$\left.\frac{\partial Q_{\Delta\mathbf{p}}\{g_T\}(\mathbf{x})}{\partial \Delta a_{21}}\right|_{\Delta\mathbf{p}=0} = y\frac{\partial g_T(\mathbf{x})}{\partial z} \tag{3.85}$$

$$\left.\frac{\partial Q_{\Delta\mathbf{p}}\{g_T\}(\mathbf{x})}{\partial \Delta a_{22}}\right|_{\Delta\mathbf{p}=0} = z\frac{\partial g_T(\mathbf{x})}{\partial z} \tag{3.86}$$

3.A.6.2   Derivatives of Sheared Volume w.r.t. Parameters

Note that the derivatives for the pure shearing transformation (without translation) at $\Delta\mathbf{p} = 0$ follows directly as:

$$\left.\frac{\partial A_{\mathbf{I}+\Delta\mathbf{A}}\{g_T\}(\mathbf{x})}{\partial \Delta p_k}\right|_{\Delta\mathbf{p}=0} = \begin{cases} 0, & \text{if } \Delta p_k = \Delta b_0, \Delta b_1, \Delta b_2 \\ \left.\frac{\partial Q_{\Delta\mathbf{p}}\{g_T\}(\mathbf{x})}{\partial p_k}\right|_{\Delta\mathbf{p}=0}, & \text{otherwise.} \end{cases} \tag{3.87}$$

3.A.6.3   Derivatives of Transform Determinant w.r.t. Parameters

The determinant of the shearing transformation $\mathbf{I} + \Delta\mathbf{A}$ can be computed as:

$$|\mathbf{I} + \Delta\mathbf{A}| = \begin{vmatrix} 1 + \Delta a_{00} & \Delta a_{01} & \Delta a_{02} \\ \Delta a_{10} & 1 + \Delta a_{11} & \Delta a_{12} \\ \Delta a_{20} & \Delta a_{21} & 1 + \Delta a_{22} \end{vmatrix} \tag{3.88}$$

$$= (1 + \Delta a_{00})\left((1 + \Delta a_{11})(1 + \Delta a_{22}) - \Delta a_{12}\Delta a_{21}\right)$$

$$- \Delta a_{01} \left((1 + \Delta a_{22}) \Delta a_{10} - \Delta a_{12} \Delta a_{20} \right)$$

$$+ \Delta a_{02} \left(\Delta a_{10} \Delta a_{21} - (1 + \Delta a_{11}) \Delta a_{20} \right). \tag{3.89}$$

The derivatives with respect to all the 12 parameters can be computed as:

$$\frac{\partial |\mathbf{I} + \Delta \mathbf{A}|}{\partial \Delta a_{00}} = (1 + \Delta a_{11})(1 + \Delta a_{22}) - \Delta a_{12} \Delta a_{21} \tag{3.90}$$

$$\frac{\partial |\mathbf{I} + \Delta \mathbf{A}|}{\partial \Delta a_{01}} = \Delta a_{12} \Delta a_{20} - (1 + \Delta a_{22}) \Delta a_{10} \tag{3.91}$$

$$\frac{\partial |\mathbf{I} + \Delta \mathbf{A}|}{\partial \Delta a_{02}} = \Delta a_{10} \Delta a_{21} - (1 + \Delta a_{11}) \Delta a_{20} \tag{3.92}$$

$$\frac{\partial |\mathbf{I} + \Delta \mathbf{A}|}{\partial \Delta a_{10}} = \Delta a_{02} \Delta a_{21} - (1 + \Delta a_{22}) \Delta a_{01} \tag{3.93}$$

$$\frac{\partial |\mathbf{I} + \Delta \mathbf{A}|}{\partial \Delta a_{11}} = (1 + \Delta a_{00})(1 + \Delta a_{22}) - \Delta a_{02} \Delta a_{20} \tag{3.94}$$

$$\frac{\partial |\mathbf{I} + \Delta \mathbf{A}|}{\partial \Delta a_{12}} = \Delta a_{01} \Delta a_{20} - (1 + \Delta a_{00}) \Delta a_{21} \tag{3.95}$$

$$\frac{\partial |\mathbf{I} + \Delta \mathbf{A}|}{\partial \Delta a_{20}} = \Delta a_{01} \Delta a_{12} - (1 + \Delta a_{11}) \Delta a_{02} \tag{3.96}$$

$$\frac{\partial |\mathbf{I} + \Delta \mathbf{A}|}{\partial \Delta a_{21}} = \Delta a_{02} \Delta a_{10} - (1 + \Delta a_{00}) \Delta a_{12} \tag{3.97}$$

$$\frac{\partial |\mathbf{I} + \Delta \mathbf{A}|}{\partial \Delta a_{22}} = (1 + \Delta a_{00})(1 + \Delta a_{11}) - \Delta a_{01} \Delta a_{10} \tag{3.98}$$

At $\Delta \mathbf{p} = \mathbf{0}$, the derivatives can be computed as:

$$\frac{\partial |\mathbf{I} + \Delta \mathbf{A}|}{\partial \Delta p_k} \bigg|_{\Delta \mathbf{p} = \mathbf{0}} = \begin{cases} 1, & \text{if } \Delta p_k = \Delta a_{00}, \Delta a_{11}, \Delta a_{22} \\ 0, & \text{otherwise.} \end{cases} \tag{3.99}$$

At $\Delta \mathbf{p} = \mathbf{0}$, the second derivatives can be computed as:

$$\frac{\partial^2 |\mathbf{I} + \Delta \mathbf{A}|}{\partial \Delta a_{00} \, \partial \Delta a_{11}} \bigg|_{\Delta \mathbf{p} = \mathbf{0}} = 1 \tag{3.100}$$

$$\left.\frac{\partial^2 |\mathbf{I} + \Delta\mathbf{A}|}{\partial \Delta a_{00} \, \partial \Delta a_{22}}\right|_{\Delta\mathbf{p}=0} = 1 \tag{3.101}$$

$$\left.\frac{\partial^2 |\mathbf{I} + \Delta\mathbf{A}|}{\partial \Delta a_{11} \, \partial \Delta a_{22}}\right|_{\Delta\mathbf{p}=0} = 1 \tag{3.102}$$

$$\left.\frac{\partial^2 |\mathbf{I} + \Delta\mathbf{A}|}{\partial \Delta a_{01} \, \partial \Delta a_{10}}\right|_{\Delta\mathbf{p}=0} = -1 \tag{3.103}$$

$$\left.\frac{\partial^2 |\mathbf{I} + \Delta\mathbf{A}|}{\partial \Delta a_{02} \, \partial \Delta a_{20}}\right|_{\Delta\mathbf{p}=0} = -1 \tag{3.104}$$

$$\left.\frac{\partial^2 |\mathbf{I} + \Delta\mathbf{A}|}{\partial \Delta a_{12} \, \partial \Delta a_{21}}\right|_{\Delta\mathbf{p}=0} = -1 \tag{3.105}$$

and zero for all other combinations of parameters.

3.A.7   Gradient and Hessian Matrix for Rigid Transformations

The gradient β_k and Hessian matrix $\alpha_{k,\ell}$ calculated in the parameter space at $\Delta\mathbf{p} = 0$ can be calculated as (ignoring similar constants and second derivative terms):

$$\beta_k \stackrel{\text{def}}{=} -\left(\frac{1}{2}\right) \left.\frac{\partial \chi^2(\mathbf{p} \circ \Delta\mathbf{p})}{\partial \Delta p_k}\right|_{\Delta\mathbf{p}=\mathbf{0}}, \qquad\qquad 0 \le k < M \tag{3.106}$$

$$= -\sum_{i=0}^{N-1} \left((Q_{\mathbf{p}^{-1}} \{g_R\} \star h)(\mathbf{x}_i) - (g_T \star R_{\varphi,\theta,\psi}^{-1} \{h\})(\mathbf{x}_i) \right)$$

$$\left(\left(Q_{\mathbf{p}^{-1}} \{g_R\} \star \frac{\partial R_{\Delta\varphi,\Delta\theta,\Delta\psi} \{h\}}{\partial \Delta p_k} \right)(\mathbf{x}_i) - \left(\frac{\partial Q_{\Delta\mathbf{p}} \{g_T\}}{\partial \Delta p_k} \star R_{\varphi,\theta,\psi}^{-1} \{h\} \right)(\mathbf{x}_i) \right),$$

$$\tag{3.107}$$

$$\alpha_{k,\ell} \stackrel{\text{def}}{=} \left(\frac{1}{2}\right) \left.\frac{\partial^2 \chi^2(\mathbf{p} \circ \Delta\mathbf{p})}{\partial \Delta p_k \partial \Delta p_\ell}\right|_{\Delta\mathbf{p}=\mathbf{0}}, \qquad\qquad 0 \le k, \ell < M \tag{3.108}$$

$$= \sum_{i=0}^{N-1} \left(\left(Q_{\mathbf{p}^{-1}} \{g_R\} \star \frac{\partial R_{\Delta\varphi,\Delta\theta,\Delta\psi} \{h\}}{\partial \Delta p_k} \right)(\mathbf{x}_i) - \left(\frac{\partial Q_{\Delta\mathbf{p}} \{g_T\}}{\partial \Delta p_k} \star R_{\varphi,\theta,\psi}^{-1} \{h\} \right)(\mathbf{x}_i) \right)$$

$$\left(\left(Q_{\mathbf{p}^{-1}} \{g_R\} \star \frac{\partial R_{\Delta\varphi,\Delta\theta,\Delta\psi} \{h\}}{\partial \Delta p_\ell} \right) (\mathbf{x}_i) - \left(\frac{\partial Q_{\Delta\mathbf{p}} \{g_T\}}{\partial \Delta p_\ell} \star R_{\varphi,\theta,\psi}^{-1} \{h\} \right) (\mathbf{x}_i) \right).$$

(3.109)

3.A.7.1   Derivatives of Rigid Transformed Volume w.r.t. Parameters

Consider the rigid body transform $Q_{\Delta\mathbf{p}} = R_{\Delta\varphi,\Delta\theta,\Delta\psi} \circ T_{\Delta\mathbf{b}}$ characterized by the parameters $\Delta\mathbf{p} : \{\Delta\varphi, \Delta\theta, \Delta\psi\}$, $\Delta\mathbf{b} \in \mathbb{R}^{3\times 1}$ applied to $\mathbf{x} \in \mathbb{R}^3$. At $\Delta\mathbf{p} = \mathbf{0}$, the derivatives with respect to the 6 parameters can be computed as:

$$\left. \frac{\partial Q_{\Delta\mathbf{p}} \{g_T\} (\mathbf{x})}{\partial \Delta b_0} \right|_{\Delta\mathbf{p}=\mathbf{0}} = \frac{\partial g_T(\mathbf{x})}{\partial x} \tag{3.110}$$

$$\left. \frac{\partial Q_{\Delta\mathbf{p}} \{g_T\} (\mathbf{x})}{\partial \Delta b_1} \right|_{\Delta\mathbf{p}=\mathbf{0}} = \frac{\partial g_T(\mathbf{x})}{\partial y} \tag{3.111}$$

$$\left. \frac{\partial Q_{\Delta\mathbf{p}} \{g_T\} (\mathbf{x})}{\partial \Delta b_2} \right|_{\Delta\mathbf{p}=\mathbf{0}} = \frac{\partial g_T(\mathbf{x})}{\partial z} \tag{3.112}$$

$$\left. \frac{\partial Q_{\Delta\mathbf{p}} \{g_T\} (\mathbf{x})}{\partial \Delta\varphi} \right|_{\Delta\mathbf{p}=\mathbf{0}} = y\frac{\partial g_T(\mathbf{x})}{\partial z} - z\frac{\partial g_T(\mathbf{x})}{\partial y} \tag{3.113}$$

$$\left. \frac{\partial Q_{\Delta\mathbf{p}} \{g_T\} (\mathbf{x})}{\partial \Delta\theta} \right|_{\Delta\mathbf{p}=\mathbf{0}} = z\frac{\partial g_T(\mathbf{x})}{\partial x} - x\frac{\partial g_T(\mathbf{x})}{\partial z} \tag{3.114}$$

$$\left. \frac{\partial Q_{\Delta\mathbf{p}} \{g_T\} (\mathbf{x})}{\partial \Delta\psi} \right|_{\Delta\mathbf{p}=\mathbf{0}} = x\frac{\partial g_T(\mathbf{x})}{\partial y} - y\frac{\partial g_T(\mathbf{x})}{\partial x}. \tag{3.115}$$

3.A.7.2   Derivatives of Rotated Volume w.r.t. Parameters

Note that the derivatives for the pure rotation transformation (without translation) at $\Delta\mathbf{p} = 0$ follows directly as:

$$\left. \frac{\partial R_{\Delta\varphi,\Delta\theta,\Delta\psi} \{g_T\} (\mathbf{x})}{\partial \Delta p_k} \right|_{\Delta\mathbf{p}=\mathbf{0}} = \begin{cases} 0, & \text{if } \Delta p_k = \Delta b_0, \Delta b_1, \Delta b_2 \\ \left. \frac{\partial Q_{\Delta\mathbf{p}} \{g_T\} (\mathbf{x})}{\partial p_k} \right|_{\Delta\mathbf{p}=\mathbf{0}}, & \text{otherwise.} \end{cases} \tag{3.116}$$

3.A.8   Propagation of Transform Parameters across Scales

Since the method is implemented by a multi-resolution approach, the derivatives and the Hessian matrices have to be computed at each resolution level, and the transformation parameters need to be propagated between levels. For example, consider the following affine transform at the coordinate system in the finest scale (Level-0):

$$\mathbf{x}_0' \stackrel{\text{def}}{=} \mathbf{A}\mathbf{x}_0 + \mathbf{b}. \tag{3.117}$$

Say, at the next coarser scale (Level-1), the coordinates change by a scalar factor s_x, s_y, s_z along x, y, z, respectively:

$$\mathbf{x}_0' \stackrel{\text{def}}{=} \mathbf{S}\mathbf{x}_0' \text{ and } \mathbf{x}_0 \stackrel{\text{def}}{=} \mathbf{S}\mathbf{x}_0, \tag{3.118}$$

where $\mathbf{S} \in \mathbb{R}^{3\times3}$ is a diagonal matrix with weights s_x, s_y, s_z. We then have:

$$\mathbf{x}_0' = \mathbf{S}\left(\mathbf{A}\mathbf{S}^{-1}\mathbf{x}_0 + \mathbf{b}\right) \tag{3.119}$$

$$= \mathbf{S}\mathbf{A}\mathbf{S}^{-1}\mathbf{x}_0 + \mathbf{S}\mathbf{b}. \tag{3.120}$$

In a dyadic pyramid scheme where $s_x = s_y = s_z = 1/2$, the general affine transform parameters at Level-k would be:

$$\mathbf{x}_k' = \mathbf{A}\mathbf{x}_k + 2^{-k}\mathbf{b}, \tag{3.121}$$

i.e., only the translation parameters change by a factor of $1/2$ across scales, while the shearing matrix remains the same.

Chapter 4

Multi-View Deconvolution and Fusion for Optical Microscopy

Abstract[10]

3D deconvolution in optical microscopy aims at recovering deblurred forms of optical sections acquired through objects. This is generally an ill-posed problem owing to the zeros prevalent along the axial direction of the optical-transfer-function (OTF). One of the ways to mitigate this problem is by acquiring data from multiple, mutually-tilted directions, which helps fill the missing cone of information in the OTF. Here, we propose a fast-converging iterative deconvolution method for multi-view deconvolution microscopy. Specifically, we formulate the imaging problem using a filter-bank structure, and present a multi-channel variation of a thresholded Landweber deconvolution algorithm with wavelet-sparsity regularization. Notably, the computational complexity of the multi-channel algorithm presented is equivalent to its single-channel counterpart. Decomposition of the minimization problem into subband-dependent terms ensures fast convergence. We demonstrate the applicability of the algorithm via simulation results.

---

[10]This chapter is based on the reference [17] co-authored with M. Liebling.

4.1   Introduction

Deconvolution is a classical inverse problem [8] with applications in fields as diverse as optical microscopy [87, 113], medical imaging [74], astronomy, [95] and photography [119]. It is widely employed both as a stand-alone computational method and as an adjunct to physical modifications in the instrument design, aimed at improving the image quality. In general, deconvolution from a single contaminated observation is an ill-posed problem, due to the complete loss of signal information at frequencies corresponding to the zeros of the filter. One of the ways to mitigate this problem is by the acquisition of multiple images of the same specimen blurred differently (single-input, multiple-output), where the lack of information in one observation is compensated in others. This better posed inverse problem can be referred to as *multi-channel* deconvolution, in contrast to the conventional *single-channel* deconvolution.

This holds particular significance in optical fluorescence microscopy, where the resolution along the optical axis is well known to be worse than that along the lateral directions. The resolution anisotropy is explainable since all objective lenses have an angular aperture of less than 90°, which means that the rays originating from a point source do not perfectly converge to a single point [11]. Instead, due to diffraction, it manifests itself as a blurred counterpart in the image, widely known as the point-spread-function (PSF). The central section of the PSF is an Airy disc, which diverges into a conical form on either side of the focal plane. The Fourier transform of the PSF, referred to as the optical transfer function (OTF), offers a different insight in the nature of degradation, where the lack of resolution in the axial direction is evident as a cone of zeros. This underscores the difficulty in recovering a good estimate of the imaged specimen from a single blurred observation alone.

In their seminal work, Shaw *et al.* [90] had proposed to alleviate this problem by

using multiple mutually-tilted, through-focal section views of the same object. Their original work followed an individual deconvolution of the tilted views and a final fusion of the reoriented data for an improved estimate of the imaged *Drosophila melanogaster* embryo nuclei. This idea has evolved since then to have a more holistic nature, where the deconvolution algorithm is applied to the ensemble of the available blurry observations, rather than to each of them separately. They have yielded results with relatively low computational complexity and have been demonstrated in various optical microscopy types, including widefield, confocal and light-sheet-based microscopy [111, 100, 85, 104]. This broad class of algorithms have come to be known as *multi-view* deconvolution microscopy, which is essentially a special case of *multi-channel* deconvolution, where the filter in each channel can be interpreted as a tilted form of one common filter.

Several *single-channel* deconvolution algorithms have been proposed for 3D microscopy. They can be broadly classified as: (a) no-neighbors, (b) neighboring, (c) linear, (d) non-linear, (e) statistical, (h) transform-domain sparsity-based, and (g) blind deconvolution techniques. We direct the interested reader to reviews on the subject [91, 87] for a detailed description. In this work, we specifically focus on a *multi-channel* deconvolution algorithm of type (h), where the ℓ_1-norm of the wavelet coefficients of the object acts as the sparsity-inducing regularizer to the deconvolution problem.

Wavelet-based 3D deconvolution microscopy is a relatively new technique. Several researchers have established the theoretical foundation underlying this approach, which alternates between a Landweber update and wavelet-coefficient thresholding [94, 34, 28, 6, 21], referred to as the thresholded Landweber (TL) or iterative shrinkage thresholding algorithm (ISTA). Recently, fast implementations were proposed for this method by Vonesch *et al.* [114, 115] and Beck *et al.* [5]. The main objective of this work is to derive a *multi-channel* analogue for this framework, and show that it can be be implemented without adding to its computational complexity, and demonstrate its applicability for

multi-view deconvolution in fluorescence microscopy.

The chapter is organized as follows. In Section 4.2, we introduce the imaging model and state the problem. We describe the method in Section 4.3, and present our experimental results in Section 4.4. We finally conclude in Section 4.5.

4.2   Problem Statement

4.2.1   Image Formation Model

We consider images formed by an optical microscope that allows rotating the sample around an axis perpendicular to the imaging direction with the coordinate system represented as $\mathbf{x} \in \mathbb{R}^3$. Following the representation in Chapter 3, we model the M different measured volumes as a convolution between rotated form of the sample and the PSF as:

$$g_i(\mathbf{x}) \stackrel{\text{def}}{=} \left(Q_{\mathbf{p}_i}^{-1} \{f\} \star h\right)(\mathbf{x}) + n_i(\mathbf{x}), \qquad i = 0, \ldots, M-1 \quad (4.1)$$

where g_i denotes the measured volume for the i-th angle, f is the original volume being imaged, n_i is an additive noise component, h is the PSF corresponding to the microscope, and $Q_{\mathbf{p}_i}^{-1} \stackrel{\text{def}}{=} A_{\mathbf{A}_i^{-1}} \circ T_{-\mathbf{A}_i^{-1}\mathbf{b}_i}$ is a general affine operator involving a shearing matrix $\mathbf{A}_i^{-1} \in \mathbb{R}^{3\times3}$ and translation of $-\mathbf{A}_i^{-1}\mathbf{b}_i \in \mathbb{R}^3$, as defined in Eq. (3.9). We choose the measured volume at the first angle as the golden reference and apply geometrical transformations to other volumes to match it. In other words, we assume $\mathbf{A}_0$ is the identity matrix and $\mathbf{b}_0 = 0$, and estimate the transform parameters $\mathbf{p}_i$, as discussed in Chapter 3, which is subsequently applied to g_i to reverse the geometrical transformations

underwent by the sample during acquisition:

$$\tilde{g}_i(\mathbf{x}) \overset{\text{def}}{=} Q_{\mathbf{p}_i}\{g_i\}(\mathbf{x}) \qquad\qquad i = 0, \ldots, M-1 \quad (4.2)$$

$$= |\mathbf{A}_i| \left(f \star A_{\mathbf{A}_i}\{h\}\right)(\mathbf{x}) + Q_{\mathbf{p}_i}\{n_i\}(\mathbf{x}) \qquad\qquad (4.3)$$

$$\overset{\text{def}}{=} \left(f \star h_i\right)(\mathbf{x}) + \tilde{n}_i(\mathbf{x}), \qquad\qquad (4.4)$$

where $\tilde{g}_i \overset{\text{def}}{=} Q_{\mathbf{p}_i}\{g_i\}$ and $h_i \overset{\text{def}}{=} |\mathbf{A}_i| A_{\mathbf{A}_i}\{h\}$ denotes geometrically transformed forms of g_i and h_i, respectively. This shift-invariant imaging model can be discretized and cast into a *multi-channel* matrix formulation. Specifically, the signal measured in the ith channel (angle) can be represented as:

$$\tilde{\mathbf{g}}_i \overset{\text{def}}{=} \mathbf{H}_i \mathbf{f} + \tilde{\mathbf{n}}_i, \qquad\qquad i = 0, \ldots, M-1 \quad (4.5)$$

where $\tilde{\mathbf{g}}_i, \mathbf{f}$, and $\tilde{\mathbf{n}}_i$ are column vectors that represent the N lexicographically ordered samples of $\tilde{g}_i$, f, and $\tilde{n}_i$, respectively, while $\mathbf{H}_i$ is the $N \times N$ transform matrix corresponding to the filtering operation with the discretized PSF h_i. All the measured signals $\tilde{\mathbf{g}}_i$ can then be concatenated to a single vector $\tilde{\mathbf{g}}$, represented as:

$$\tilde{\mathbf{g}} \overset{\text{def}}{=} \begin{pmatrix} \tilde{\mathbf{g}}_0 \\ \vdots \\ \tilde{\mathbf{g}}_{M-1} \end{pmatrix} = \begin{pmatrix} \mathbf{H}_0 \\ \vdots \\ \mathbf{H}_{M-1} \end{pmatrix} \mathbf{f} + \begin{pmatrix} \tilde{\mathbf{n}}_0 \\ \vdots \\ \tilde{\mathbf{n}}_{M-1} \end{pmatrix} \overset{\text{def}}{=} \mathbf{H}\mathbf{f} + \tilde{\mathbf{n}}, \qquad\qquad (4.6)$$

The inverse problem that we wish to solve is finding an estimate $\bar{\mathbf{f}}$ of $\mathbf{f}$, given the collection of the spatially registered multi-view measurements $\tilde{\mathbf{g}}$ and the transform matrices $\mathbf{H}$.

4.2.2   Cost-function

We follow a transform-domain sparsity-based approach to solve this inverse problem. Specifically, we wish to use the assumption that objects of interest $\mathbf{f}$ can often be approximated well using only a few large wavelet coefficients. We represent the object in a dyadic multi-resolution wavelet space as:

$$f^V(\mathbf{x}) = \sum_{j=1}^{J} \sum_{s \in S_j} \sum_{\mathbf{k} \in \mathbb{Z}^3} 2^{-j} \langle f, \mathring{\psi}_s^{\top} \left(\cdot / 2^j - \mathbf{k} \right) \rangle \psi_s \left(\mathbf{x}/2^j - \mathbf{k} \right) \tag{4.7}$$

$$\stackrel{\text{def}}{=} \sum_{j=1}^{J} \sum_{s \in S_j} \sum_{\mathbf{k} \in \mathbb{Z}^3} w_{j,s}[\mathbf{k}] \cdot \psi_{j,s} \left(\mathbf{x} - \mathbf{k} \right). \tag{4.8}$$

where $\psi_{j,s}(\mathbf{x}) \stackrel{\text{def}}{=} \psi_s(\mathbf{x}/2^j)$ and $w_{j,s}$ represents the wavelet (or scaling) basis function and wavelet coefficients corresponding to the subband s at scale j, respectively, J is the number of scales, and $S_j = \{1, \ldots, S\}$ denotes the S wavelet subbands at scale $1 \leq j \leq J$. For example, $S = 3$ and 7 in 2D and 3D coordinate systems, respectively. At the coarsest scale $j = J$, we also include the scaling subband as $S_J = \{0, \ldots, S\}$. The wavelet coefficients $w_{j,s}$ can be arranged in a vector form and defined in terms of matrix multiplications as:

$$\mathbf{w}_{j,s} \stackrel{\text{def}}{=} \mathring{\Psi}_{j,s}^{\top} \mathbf{f}, \tag{4.9}$$

where $\mathring{\Psi}_{j,s}^{\top}$ is the matrix that represents the combination of filtering/downsampling operations for the analysis action corresponding to the wavelet coefficients $w_{j,s}$. The ensemble

of wavelet coefficients can then be represented as:

$$\mathbf{w} \stackrel{\text{def}}{=} \begin{pmatrix} \mathbf{w}_{J,0} \\ \mathbf{w}_{J,1} \\ \vdots \\ \mathbf{w}_{1,S} \end{pmatrix} = \begin{pmatrix} \mathring{\Psi}_{J,0}^{\top} \\ \mathring{\Psi}_{J,1}^{\top} \\ \vdots \\ \mathring{\Psi}_{1,S}^{\top} \end{pmatrix} \mathbf{f} \stackrel{\text{def}}{=} \mathring{\Psi}^{\top} \mathbf{f}. \tag{4.10}$$

Similarly, the discrete samples of f^V can be arranged in a vector form and defined in terms of matrix multiplications as:

$$\mathbf{f}^V \stackrel{\text{def}}{=} \sum_{j=1}^{J} \sum_{s \in S_j} \Psi_{j,s} \mathbf{w}_{j,s} = \begin{pmatrix} \Psi_{J,0} & \Psi_{J,1} & \cdots & \Psi_{1,S} \end{pmatrix} \begin{pmatrix} \mathbf{w}_{J,0} \\ \mathbf{w}_{J,1} \\ \vdots \\ \mathbf{w}_{1,S} \end{pmatrix} \stackrel{\text{def}}{=} \Psi \mathbf{w}, \tag{4.11}$$

where $\mathbf{w}_{j,s}$ is the vectorized form of the wavelet coefficients $w_{j,s}$ and $\Psi_{j,s}$ is the matrix that represents the combination of upsampling/filtering operations for the synthesis action corresponding to the wavelet coefficients $w_{j,s}$.

Similar to wavelet-sparsity-based inverse problems in the literature [94, 34, 28, 6, 21, 114, 115], we pursue the solution $\bar{\mathbf{f}} = \Psi\bar{\mathbf{w}}$, where $\bar{\mathbf{w}}$ minimizes the cost function:

$$\mathcal{C}(\mathbf{w}) \stackrel{\text{def}}{=} \|\tilde{\mathbf{g}} - \mathbf{H}\Psi\mathbf{w}\|_{\ell_2}^2 + \lambda\|\mathbf{w}\|_{\ell_1}, \tag{4.12}$$

where λ is a non-negative scalar quantity. The two terms in the cost function $\mathcal{C}(\mathbf{w})$ of Eq. (4.12) serve the purposes of data-consistency and regularization, respectively.

Replacing the general form of $\tilde{\mathbf{g}}$ and $\mathbf{H}$ in Eq. (4.12) by taking advantage of its

structure specific to our problem, we get:

$$\mathcal{C}(\mathbf{w}) = \sum_{i=0}^{M-1} \|\tilde{\mathbf{g}}_i - \mathbf{H}_i \Psi \mathbf{w}\|_{\ell_2}^2 + \lambda \|\mathbf{w}\|_{\ell_1}. \qquad (4.13)$$

In the following sections, we show that the special form of the matrix $\mathbf{H}$ in a *multi-channel* scheme allows for the direct application of the fast, wavelet-based minimization technique originally developed by Vonesch and Unser [115] in an implicit *single-channel* framework and which is efficiently implemented in the Fourier domain.

4.3   Method

We start by discussing a simpler inverse problem, where there is no regularization ($\lambda = 0$) before recalling Vonesch and Unser's method [115] and finally addressing the special case of *multi-view* deconvolution.

4.3.1   Multi-channel Landweber Iteration

When $\lambda = 0$, the cost function in Eq. (4.12) takes the form:

$$\mathcal{C}(\mathbf{w}) = \|\tilde{\mathbf{g}} - \mathbf{H}\Psi \mathbf{w}\|_{\ell_2}^2, \qquad (4.14)$$

making it a pure least-squares minimization problem. The minimizer to this problem can be directly obtained by the pseudo-inverse of $\mathbf{H}$, when $\mathbf{H}$ is non-singular. However, if $\mathbf{H}$ is ill-conditioned, this is a poor choice since it is highly susceptible to errors in $\tilde{\mathbf{g}}$ and can amplify the noise component. As a viable solution, the minimization can be performed iteratively by gradient descent [92], which is similar to the Landweber iteration [57] in this context, and can be stopped after a fixed number of iterations or when the variation
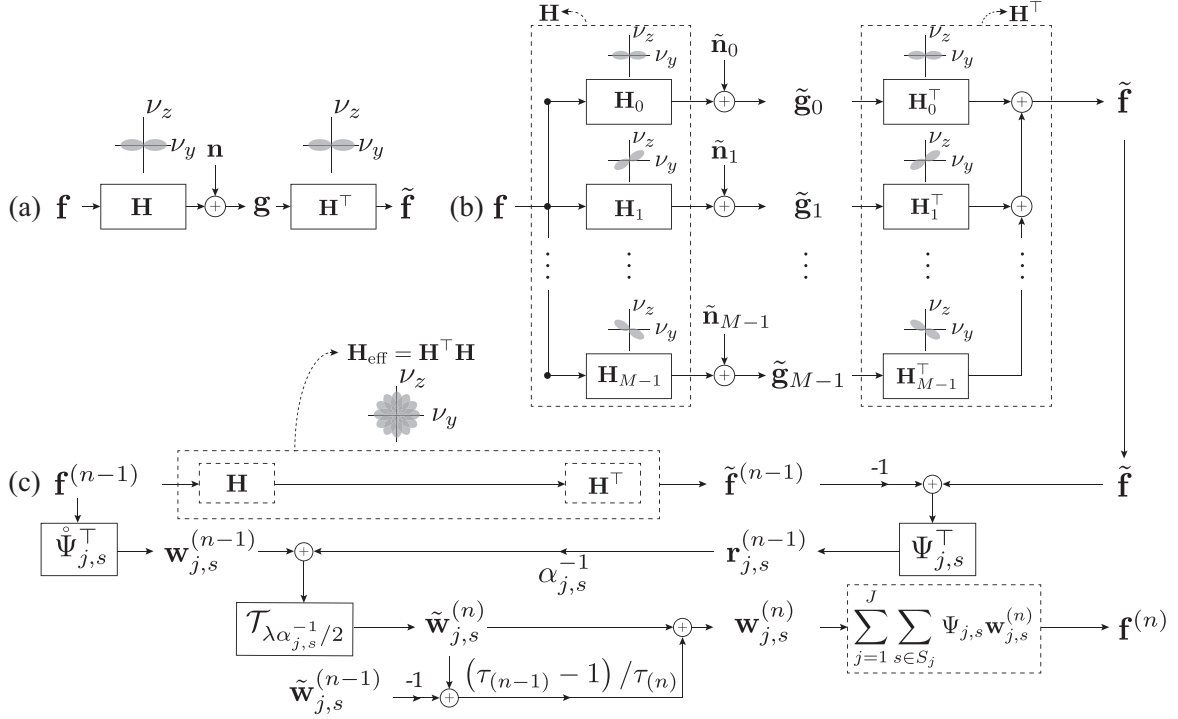
Figure 4.1: Block diagram showing (a) the forward imaging model with M angles, where the OTF in the first angle has zeros along the axial direction ν_z, and the re-blurred signal $\tilde{\mathbf{f}}$; (b) the computation of the subband dependent residual $\mathbf{r}_s^{(n-1)}$ for the nth Landweber iteration, from $\tilde{\mathbf{f}}$, $\mathbf{H}_{\text{eff}}$ and $\mathbf{f}^{(n-1)} = \sum_{s \in S_1} \Psi_s \mathbf{w}_s^{(n-1)}$; (c) the two-step procedure of Landweber iteration and soft-thresholding ($\mathcal{T}$), characteristic in the fast TL algorithm, to update the wavelet coefficients $\mathbf{w}_s$ in each subband s and eventually construct the updated estimate $\mathbf{f}^{(n)}$.

in the update is below a set threshold.

Starting from an initial estimate $\mathbf{w}^{(0)}$, we can arrive at an updated sequence $\mathbf{w}^{(n)}$ that eventually converges to the minimizer of $\mathcal{C}(\mathbf{w})$. Since $\mathbf{H}$ is a linear operator, the Landweber iteration holds:

$$\mathbf{w}^{(n)} \stackrel{\text{def}}{=} \mathbf{w}^{(n-1)} + \tau \cdot \Psi^\top \mathbf{H}^\top \left(\mathbf{g} - \mathbf{H}\Psi\mathbf{w}^{(n-1)} \right) \tag{4.15}$$

$$\stackrel{\text{def}}{=} \mathbf{w}^{(n-1)} + \tau \cdot \mathbf{r}^{(n-1)}, \tag{4.16}$$

where $\mathbf{r}^{(n-1)}$ is the residual that acts as the correction term in each iteration, while τ is

79

the step size that controls the contribution of $\mathbf{r}^{(n-1)}$ to the latest update. Owing to the special structure of the matrices in our present context, we can rewrite the residual in each iteration as:

$$\mathbf{r}^{(n-1)} = \Psi^\top \left(\tilde{\mathbf{f}} - \mathbf{H}_{\text{eff}} \Psi \mathbf{w}^{(n-1)} \right) \tag{4.17}$$

where $\tilde{\mathbf{f}}$ is the sum of the re-blurred spatially registered multi-view measurements:

$$\tilde{\mathbf{f}} = \sum_{i=0}^{M-1} \mathbf{H}_i^\top \tilde{\mathbf{g}}_i, \tag{4.18}$$

and $\mathbf{H}_{\text{eff}}$ is the matrix corresponding to the effective *single-channel* filter (Fig. 4.1(b)) defined as:

$$\mathbf{H}_{\text{eff}} = \sum_{i=0}^{M-1} \mathbf{H}_i^\top \mathbf{H}_i. \tag{4.19}$$

Note that this *multi-channel* equivalent of the Landweber iteration could be easily implemented in the frequency domain, just as in the *single-channel* problem. This follows from the fact that $\mathbf{H}$ and $\mathbf{H}^\top$ are analogous to the analysis and synthesis sides of a filter-bank, respectively, and can be combined to form an effective *single-channel* filter, as illustrated in Fig. 4.1(a).

4.3.2   Fast Iterative Shrinkage Thresholding Algorithm

We follow the approach proposed by Vonesch and Unser [115] in the *single-channel* scheme to minimize $\mathcal{C}(\mathbf{w})$. For the purpose of completeness, we briefly recall the algorithm below, before discussing its *multi-channel* counterpart.

4.3.2.1   Single-channel Fast Iterative Shrinkage Thresholding Algorithm

For better clarity, we rewrite the cost function in Eq. (4.12), for the *single-channel* scenario ($M = 1$) as:

$$\mathcal{C}(\mathbf{w}) = \|\mathbf{g}_0 - \mathbf{H}_0 \Psi \mathbf{w}\|_{\ell_2}^2 + \lambda \|\mathbf{w}\|_{\ell_1}. \tag{4.20}$$

Since minimizing $\mathcal{C}(\mathbf{w})$ is non-trivial, the algorithm proceeds to minimize an auxiliary cost function $\mathcal{A}^{(n)}(\mathbf{w})$, which closely approximates $\mathcal{C}(\mathbf{w})$ and is easier to minimize:

$$\mathcal{A}^{(n)}(\mathbf{w}) \stackrel{\text{def}}{=} \mathcal{C}(\mathbf{w}) + \sum_{j=1}^{J} \sum_{s \in S_j} \alpha_{j,s} \left\| \mathbf{w}_{j,s}^{(n-1)} - \mathbf{w}_{j,s} \right\|_{\ell_2}^2 - \left\| \mathbf{H}_0 \Psi \left(\mathbf{w}^{(n-1)} - \mathbf{w} \right) \right\|_{\ell_2}^2, \tag{4.21}$$

where the subband dependent constants $\alpha_{j,s}$ are such that

$$\|\mathbf{H}_0 \Psi \mathbf{w}\|_{\ell_2}^2 \leq \sum_{j=1}^{J} \sum_{s \in S_j} \alpha_{j,s} \|\mathbf{w}_{j,s}\|_{\ell_2}^2. \tag{4.22}$$

This auxiliary cost function $\mathcal{A}^{(n)}(\mathbf{w})$ has two important characteristics for any $\mathbf{w} \in \ell_2$:

$$\mathcal{A}^{(n)}(\mathbf{w}) \geq \mathcal{C}(\mathbf{w}), \tag{4.23}$$

$$\mathcal{A}^{(n)}(\mathbf{w}^{(n-1)}) = \mathcal{C}(\mathbf{w}^{(n-1)}). \tag{4.24}$$

These characteristics imply that if a new estimate $\mathbf{w}^{(n)} = \arg\min \mathcal{A}^{(n)}(\mathbf{w})$ can be found, it will also effectively decrease $\mathcal{C}(\mathbf{w})$, since

$$\mathcal{C}(\mathbf{w}^{(n)}) \leq \mathcal{A}^{(n)}(\mathbf{w}^{(n)}) \leq \mathcal{A}^{(n)}(\mathbf{w}^{(n-1)}) = \mathcal{C}(\mathbf{w}^{(n-1)}). \tag{4.25}$$

A key aspect of the multi-resolution approach [115] is that $\mathcal{A}^{(n)}(\mathbf{w})$ in Eq. (4.21) can

be rewritten in terms of scale and subband-dependent sub-functions :

$$\mathcal{A}^{(n)}(\mathbf{w}) = \sum_{j=1}^{J} \sum_{s \in S_j} \alpha_{j,s} \left(\left\| \mathbf{w}_{j,s}^{(n-1)} + \alpha_{j,s}^{-1} \mathbf{r}_{j,s}^{(n-1)} - \mathbf{w}_{j,s} \right\|_{\ell_2}^2 + \lambda \alpha_{j,s}^{-1} \left\| \mathbf{w}_{j,s} \right\|_{\ell_1} \right) + \gamma, \quad (4.26)$$

$$\stackrel{\text{def}}{=} \sum_{j=1}^{J} \sum_{s \in S_j} \alpha_{j,s} \cdot \mathcal{A}_{j,s}^{(n)}(\mathbf{w}_s) + \gamma, \quad (4.27)$$

where γ is a constant independent of $\mathbf{w}$ and $\mathbf{r}_{j,s}^{(n-1)}$ is the residual for the wavelet subband s at scale j during the nth iteration defined as:

$$\mathbf{r}_{j,s}^{(n-1)} \stackrel{\text{def}}{=} \Psi_{j,s}^{\top} \mathbf{H}_0^{\top} \left(\mathbf{g}_0 - \mathbf{H}_0 \Psi \mathbf{w}^{(n-1)} \right). \quad (4.28)$$

Note that Eq. (4.27) reveals that the auxiliary functional is essentially a weighted sum of sub-functionals $\mathcal{A}_{j,s}^{(n)}$ that depend on distinct subbands. This implies that one can individually minimize each sub-functional as:

$$\mathbf{w}_{j,s}^{(n)} \stackrel{\text{def}}{=} \arg \min_{\mathbf{w}} \mathcal{A}_{j,s}^{(n)}(\mathbf{w}), \quad (4.29)$$

and effectively minimize $\mathcal{A}^{(n)}(\mathbf{w})$:

$$\mathbf{w}^{(n)} \stackrel{\text{def}}{=} \arg \min_{\mathbf{w}} \mathcal{A}^{(n)}(\mathbf{w}) = \begin{pmatrix} \mathbf{w}_{J,0}^{(n)} \\ \vdots \\ \mathbf{w}_{1,S}^{(n)} \end{pmatrix}, \quad (4.30)$$

i.e. $\mathbf{w}^{(n)}$ is a collection of the wavelet subband coefficients $\mathbf{w}_{j,s}^{(n)}$ that minimize each sub-functional $\mathcal{A}_{j,s}^{(n)}$. The minimization of $\mathcal{A}_{j,s}^{(n)}$ is readily given by the *wavelet shrinkage*

algorithm of Donoho and Johnstone [29]:

$$\mathbf{w}_{j,s}^{(n)} = \mathcal{T}_{\lambda \alpha_{j,s}^{-1}/2} \left\{ \mathbf{w}_{j,s}^{(n-1)} + \alpha_{j,s}^{-1} \mathbf{r}_{j,s}^{(n-1)} \right\}. \tag{4.31}$$

where $\mathcal{T}_{\theta}$ is the soft-thresholding operation defined as:

$$\mathcal{T}_{\theta}(w) \stackrel{\text{def}}{=} \operatorname{sgn}(w) \max\left(|w| - \theta, 0\right). \tag{4.32}$$

The thresholded Landweber algorithm thus involves alternating between two steps: (a) a Landweber update of the wavelet coefficients from the previous iteration, and (b) a soft-thresholding of the coefficients computed in (a), as evident in Eq. (4.31).

The scaling factors $\alpha_{j,s}$ that satisfy Eq. (4.22) can be efficiently estimated for all subbands $s \in S_j$, $j = 1, \ldots, J$, as:

$$\alpha_{j,s} \geq \sum_{s' \in S_j} \rho\left(\Psi_{j,s'}^{\top} \mathbf{H}_0^{\top} \mathbf{H}_0 \Psi_{j,s}\right), \qquad \forall s \in S_j \tag{4.33}$$

if the wavelet coefficients in only one scale are updated at a time [115], where $\rho(\mathbf{A})$ denotes the spectral radius [37] of the square matrix $\mathbf{A}$. This is easily computed in the frequency domain using DFT. Specifically, in a wavelet decomposition with a dyadic subsampling scheme,

$$\rho\left(\Psi_{j,s'}^{\top} \mathbf{H}_0^{\top} \mathbf{H}_0 \Psi_{j,s}\right) = \max_{k_0} \left| \sum_{k=0}^{2^j-1} \hat{\psi}_{j,s'}^{*}\left[k_0 + k\frac{N}{2^j}\right] \hat{\psi}_{j,s}\left[k_0 + k\frac{N}{2^j}\right] \left|\hat{h}_0\left[k_0 + k\frac{N}{2^j}\right]\right|^2 \right|,$$
$$\tag{4.34}$$

where $\hat{h}_0$ denotes the DFT coefficients of the discretized h_0. The subband dependent constants $\alpha_{j,s}$ form the backbone of the *fast* TL algorithm and is in direct contrast to the traditional TL algorithm, where $\alpha = \rho(\mathbf{H}_0^{\top} \mathbf{H}_0)$ is used for all subbands, adversely

affecting the convergence rate of the algorithm. By letting j vary at every iteration, it is then possible to successively update the subbands at all scales. This can be efficiently realized by several multi-grid techniques, without explicitly recomputing the subband residuals across different scales [115].

The performance of ISTA can be further sped up by computing the next iterate based not only on the previous one, but also on two or more previously computed iterates (fast ISTA, (FISTA) [5]). Specifically, the steps of the minimization are:

$$\mathbf{w}_{j,s}^{(n)} \overset{\text{def}}{=} \tilde{\mathbf{w}}_{j,s}^{(n)} + \left(\frac{\tau_{(n-1)} - 1}{\tau_{(n)}} \right) \left(\tilde{\mathbf{w}}_{j,s}^{(n)} - \tilde{\mathbf{w}}_{j,s}^{(n-1)} \right), \tag{4.35}$$

where $\mathbf{w}_{j,s}^{(n)}$ are the wavelet coefficients in the sub-band s at scale j during the n-th iteration, and the temporary coefficients:

$$\tilde{\mathbf{w}}_{j,s}^{(n)} \overset{\text{def}}{=} \mathcal{T}_{\lambda \alpha_{j,s}^{-1}/2} \left\{ \mathbf{w}_{j,s}^{(n-1)} + \alpha_{j,s}^{-1} \mathbf{r}_{j,s}^{(n-1)} \right\}, \tag{4.36}$$

are obtained via the soft-thresholding operation defined in Eq. (4.32), with the weighing factors defined as:

$$\tau_{(n)} \overset{\text{def}}{=} \frac{1 + \sqrt{1 + 4\tau_{(n-1)}^2}}{2}. \tag{4.37}$$

Commonly used initial conditions include $\tau_{(0)} = 1$ and $\tilde{\mathbf{w}}_{j,s}^{(0)} = \mathbf{w}_{j,s}^{(0)} = \mathring{\Psi}_{j,s}^{\top} \mathbf{g}$.

4.3.2.2   Multi-channel Fast Iterative Shrinkage Thresholding Algorithm

For the *multi-channel* framework, we can redefine the auxiliary cost function $\mathcal{A}^{(n)}(\mathbf{w})$ in Eq. (4.21) as:

$$\mathcal{A}^{(n)}(\mathbf{w}) \overset{\text{def}}{=} \mathcal{C}(\mathbf{w}) + \sum_{j=1}^{J} \sum_{s \in S_j} \alpha_{j,s} \left\| \mathbf{w}_s^{(n-1)} - \mathbf{w}_{j,s} \right\|_2^2 - \sum_{i=0}^{M-1} \left\| \mathbf{H}_i \Psi \left(\mathbf{w}^{(n-1)} - \mathbf{w} \right) \right\|_2^2, \quad (4.38)$$

where the constants $\alpha_{j,s}$ are such that

$$\sum_{i=0}^{M-1} \|\mathbf{H}_i \Psi \mathbf{w}\|_2^2 \leq \sum_{j=1}^{J} \sum_{s \in S_j} \alpha_{j,s} \|\mathbf{w}_{j,s}\|_2^2. \tag{4.39}$$

As in the *single-channel* case, we can rewrite $\mathcal{A}^{(n)}(\mathbf{w})$ in terms of scale and sub-band dependent sub-functionals $\mathcal{A}_s^{(n)}$, as given in Eq. (4.27), where the wavelet subband residual $\mathbf{r}_s^{(n-1)}$ now takes the form:

$$\mathbf{r}_{j,s}^{(n-1)} \stackrel{\text{def}}{=} \Psi_{j,s}^{\top} \left(\tilde{\mathbf{f}} - \mathbf{H}_{\text{eff}} \Psi \mathbf{w}^{(n-1)} \right). \tag{4.40}$$

This new expression for $\mathbf{r}_{j,s}^{(n-1)}$ can be easily computed (Fig. 4.1(c)) similar to that in the *single-channel* form and thus has an equivalent computational complexity. The soft-thresholding of the Landweber updated wavelet coefficients is exactly identical to that discussed for the *single-channel* case, yielding $\mathbf{w}_{j,s}^{(n)} \stackrel{\text{def}}{=} \arg\min \mathcal{A}_{j,s}^{(n)}(\mathbf{w})$, as in Eq. (4.31).

The scaling factors $\alpha_{j,s}$ that satisfy Eq. (4.39) can be calculated for all subbands $s \in S_j$, $j = 1, \ldots, J$, similar to that in Eq. (4.33), as:

$$\alpha_{j,s} \geq \sum_{s' \in S_j} \rho \left(\Psi_{j,s'}^{\top} \mathbf{H}_{\text{eff}} \Psi_{j,s} \right). \tag{4.41}$$

Again, this can be easily computed in the frequency domain using DFT, where the counterpart to Eq. (4.34) is given by:

$$\rho \left(\Psi_{j,s'}^{\top} \mathbf{H}_{\text{eff}} \Psi_{j,s} \right) = \max_{k_0} \left| \sum_{k=0}^{2^j-1} \hat{\psi}_{j,s'}^* \left[k_0 + k\frac{N}{2^j} \right] \hat{\psi}_{j,s} \left[k_0 + k\frac{N}{2^j} \right] \sum_{i=0}^{M-1} \left| \hat{h}_i \left[k_0 + k\frac{N}{2^j} \right] \right|^2 \right|. \tag{4.42}$$

Therefore, owing to the special structure of the *multi-channel* framework, all the

efficient multi-grid techniques discussed by Vonesch and Unser [115] for the *single-channel* case still holds valid for any general wavelet basis. As before, the performance of ISTA can be further improved using FISTA.

4.4   Results

We demonstrate the performance of the discussed algorithm by deconvolving an intentionally blurred confocal stack of a mouse brain section showing the brain-brain barrier [23]. The specimen is immunostained for glial fibrillary acidic protein (GFAP) (red) to show the astrocytic processes and Factor 8 (FVIII) (green) in the vesicles in the endothelial cells of the blood microvessel walls. (Fig. 4.4(a)). For the confocal dataset available, where the original voxel size is $0.2 \times 0.2 \times 0.5$ μm, cubic interpolation is employed along the last dimension to make the resolution uniform as $0.2 \times 0.2 \times 0.2$ μm. The size of this data stack is finally chosen as $256 \times 256 \times 256$, where zero-padding is employed in the absence of data. The two channels in the dataset are processed separately, by treating the gray-scale values as pixel values recorded by a 16-bit camera. In order to have a good visual reference to assess the restoration quality along the axial direction z, we rotate the original confocal stack available by 90° about the y-axis, to arrive at our phantom object **f** (Fig. 4.4(a)).

The ImageJ plugin 'PSF Generator' [53] is used to create a phantom wide-field microscope PSF (Fig. 4.2) that is eventually used to blur the data (Fig. 4.4(i-iv)). Richards and Wolf model is used for this purpose and the parameters chosen are as follows: numerical aperture (NA) = 0.7, refractive index of immersion medium = 1, emission wavelength = 515 nm, lateral and axial resolution = 0.2 μm, size = $256 \times 256 \times 256$. The effective filters h_i are normalized such that $\rho(\mathbf{H}^\top \mathbf{H}) = 1$.

In order to simulate the presence of noise components, Gaussian white noise is added
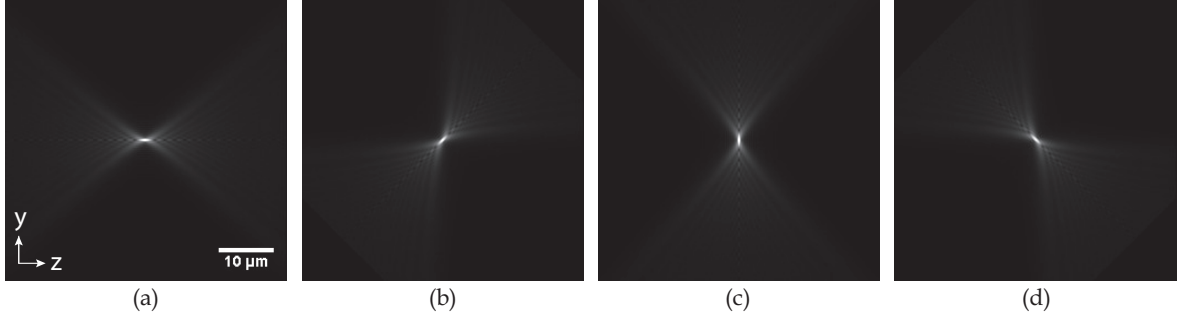
Figure 4.2: The $x = 0$ planes of the $M = 4$ mutually-tilted PSFs h_i, generated by the Richards and Wolf model (shown with gamma = 0.5). The angles shown correspond to (a) 0°, (b) 45°, (c) 90° and (d) 135°. The scale bar is 10 μm.

to the blurred result from each angle. The variance (σ^2) is set the same for all angles and is computed such that the blurred signal-to-noise ratio (BSNR) [114] in the first observation, defined as:

$$\text{BSNR} = 10 \log_{10} \left(\frac{\|\mathbf{g}_0\|_2^2 - N \left(\text{mean}(\mathbf{g}_0)\right)^2}{N\sigma^2} \right), \qquad (4.43)$$

is equal to 40 dB. The initial estimate for the iterative process is computed using a filtering operation akin to linear Wiener or Tikhonov filtering, following Figueiredo *et al.* [34]:

$$\mathbf{w}^{(0)} = \mathring{\mathbf{W}}^\top (\mathbf{H}^\top \mathbf{H} + \beta\sigma^2 \mathbf{I})^{-1} \mathbf{H}^\top \tilde{\mathbf{g}}, \qquad (4.44)$$

where $\mathbf{I}$ denotes an identity matrix and β is chosen as 10^{-8} to yield best results in our experiment.

The conventional *single-channel* fast TL deconvolution result after 10 iterations, using a $J = 5$ level decomposition in Daubechies-4 wavelet basis, is shown in Fig. 4.4(b), with the regularization factor chosen as $\lambda = 0.1$. As was done by Vonesch and Unser [115], we use a random shift of the estimate at the beginning of every fast TL iteration. Using the same parameters and $M = 4$ mutually-tilted blurred observations acquired
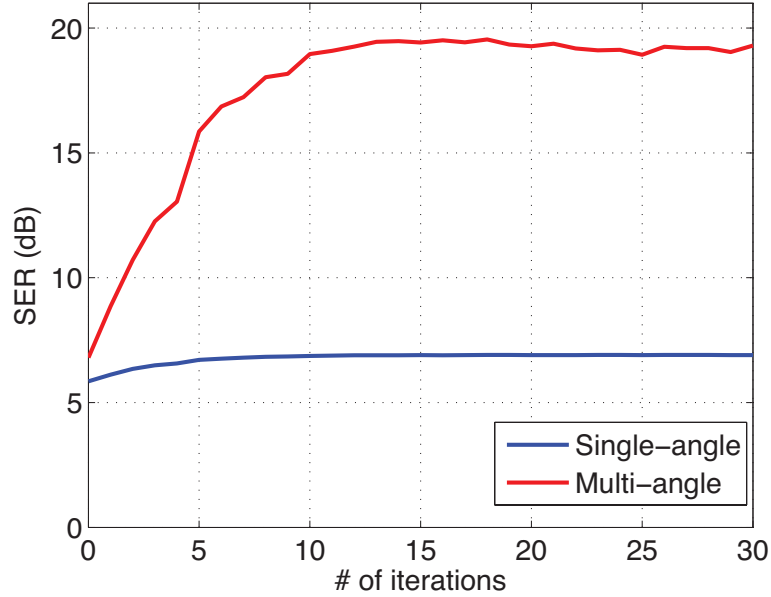
Figure 4.3: Comparison of the evolution of the SER values with the number of iterations corresponding to single-view and multi-view FISTA deconvolution. Even though both cases achieve convergence within 10 iterations, multi-view FISTA has a steeper rise in SER due to the relatively less ill-posed nature of the deconvolution problem.

at angles uniformly-spaced over 180°, about the x-axis, the *multi-channel* fast TL deconvolution yields the result shown in Fig. 4.4(c), with evidently better axial resolution than Fig. 4.4(b). For a quantitative comparison of the results, we next calculated the *signal-to-error* ratio (SER), defined as:

$$\mathrm{SER}(\mathbf{f}') \stackrel{\text{def}}{=} 10 \log_{10} \left(\frac{\|\mathbf{f}\|_2^2}{\|\mathbf{f}' - \mathbf{f}\|_2^2} \right). \tag{4.45}$$

The SER values corresponding to the red channel of the datasets are shown in Fig. 4.3. Note that both the *single-channel* and *multi-channel* forms of the algorithm achieve convergence within around 10 iterations. However, since the deconvolution problem is less ill-posed in the *multi-channel* scenario, the evolution of the SER results is much steeper than the *single-channel* case, corroborating the results shown in Fig. 4.4.

Note that unless the microscope is specially designed to acquire images from multiple

angles [99], it becomes necessary to tilt the samples appropriately using an external hardware for multi-view microscopy. In our experiment, we simulate the stack rotations to arrive at $\tilde{\mathbf{g}}$, which is subsequently fed to our deconvolution algorithm.

The algorithm was run in Matlab (R2012b) on a Windows 64-bit machine, equipped with a dual-core Intel Xeon 3.4-GHz CPU and 16 GB RAM. The *coarse-to-fine* [115] update strategy was followed for both *single-channel* and *multi-channel* deconvolution, which each took around 4 minutes for 10 iterations in our experiment involving $256 \times 256 \times 256$ data stacks.

4.5   Conclusion

In this work, we have presented a multi-channel variation of the fast thresholded Landweber algorithm for wavelet-regularized deconvolution. We have discussed the applicability of the framework in particular significance to multi-view 3D deconvolution microscopy, where the filter in each channel can be interpreted as the microscope PSF at a different angle. This was shown to improve upon the ill-posed nature of the conventional deconvolution problem, with the information lost in any one channel being compensated for in a different channel. Furthermore, we have shown that the iterative joint multi-view deconvolution and fusion algorithm can be executed with the same computational complexity as its single-view variant.
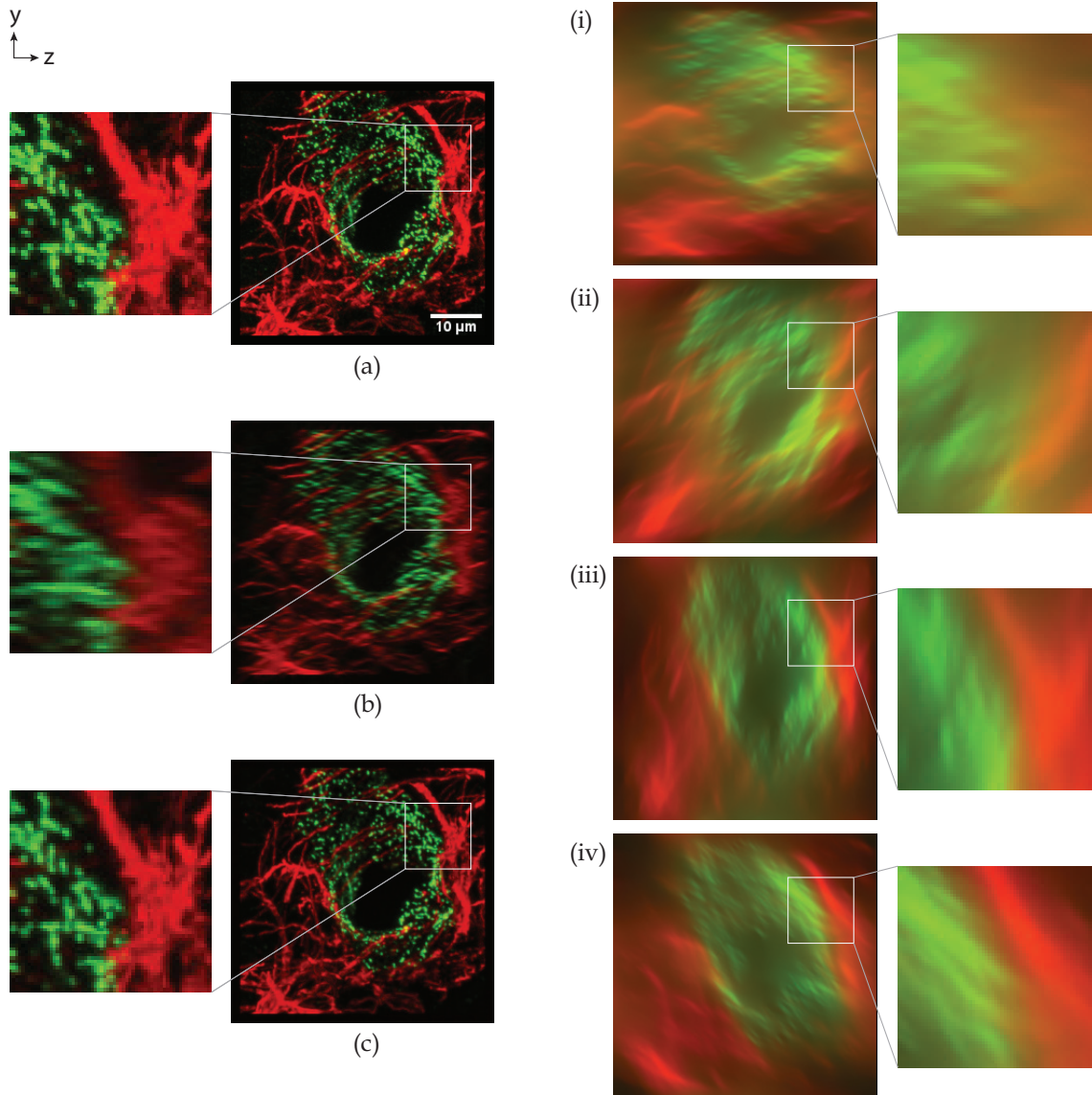
Figure 4.4: Maximum intensity projections of experimental data stacks for two channels (red and green) representing fluorescence in (a) the specimen $\mathbf{f}$, (i-iv) the $M = 4$ blurred observations $\mathbf{g}_i$, $i = 0, \ldots, M-1$, from the PSFs shown in Fig. 4.2(a) - (d), respectively, (b) *single-channel* fast TL deconvolution result from (i) after 10 iterations, and (c) *multi-channel* fast TL deconvolution result from (i-iv) after 10 iterations. The subfigures represent the zoomed forms of the regions shown. The scale bar is 10 μm.

Chapter 5

Depth-Variant Deconvolution and Fusion for Optical Microscopy

Abstract[11]

Deconvolution offers an effective way to improve the data resolution in optical microscopy. While fast algorithms are available when the point-spread-function (PSF) is shift-invariant, they are not directly applicable in thick samples, where the problem is depth-variant (DV). Here, we propose a fast iterative-shrinkage-thresholding 3D deconvolution method that uses different PSFs at every depth. This is realized by modeling the imaging system as a multi-rate filter-bank, with each channel corresponding to a distinct 3D PSF dependent on the position along the optical axis. The complexity associated with the thresholded Landweber update in each iteration of our DV algorithm is equivalent to that of an iteration in an SI algorithm, multiplied by the number of channels in the filter-bank. We have illustrated the effectiveness of our algorithm with simulated images of a set of beads embedded in an aqueous gel and varying PSFs along the optical axis.

---

[11]This chapter is based on the reference [18] co-authored with M. Liebling.
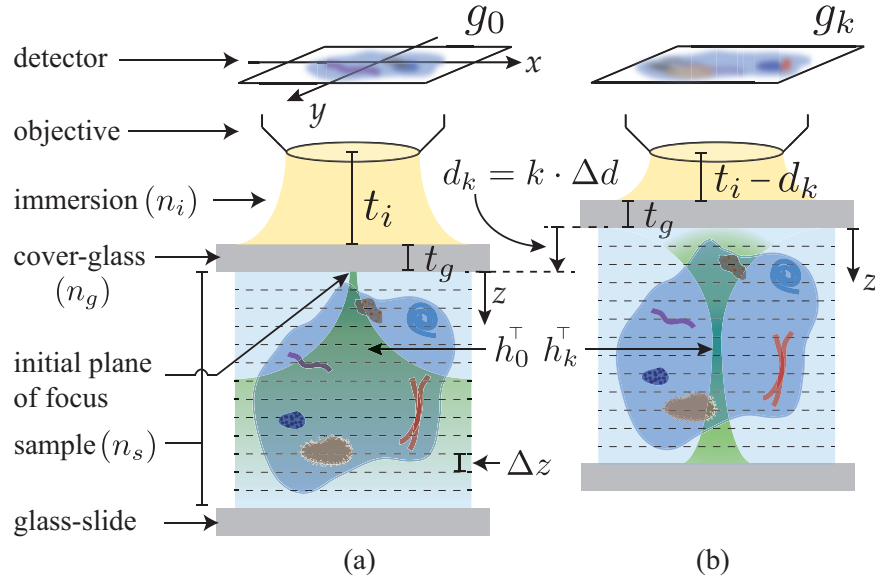
Figure 5.1: Each 2D plane imaged with optical sectioning, g_i, is an inner-product (along z) between the original 3D data f and the depth-varying PSF $h_i^\top$.

5.1 Introduction

Optical microscopy is an important tool for imaging live samples. Volumetric 3D imaging is possible in weakly-scattering objects by collecting a stack of images while focusing the microscope objective at different depths in the sample. In wide-field microscopy, images are contaminated by out-of-focus light from planes above and below the examined plane. This results in a spatial blur, particularly in the axial direction. The image formation process is usually modeled as a linear space-invariant (SI) operation, where the 3D object is magnified and convolved with the point-spread-function (PSF). The 3D object can then be restored via suitable deconvolution algorithms [1], including the classical Landweber deconvolution [57]. While the space-invariance assumption is reasonable for relatively thin samples, when imaging thick samples, the shape of the PSF varies with depth, particularly when there is a mismatch between the refractive indices of the immersion medium (n_i), any cover-slip (n_g) and sample (n_s) (Fig. 5.1).

To restore images obtained with depth-dependent PSFs, several algorithms have been proposed that involve breaking the dataset into smaller blocks on which efficient SI deconvolution algorithms can be applied [67, 104]. The quality of such approaches depends on the size of the blocks and the careful design of transition masks to merge them once deconvolved. Other approaches approximate the depth-varying blur as a spatially weighted combination of SI convolutions [81, 7]. In this work, we present an approach that directly considers a depth-variant PSF deconvolution problem, yet preserves the form of a highly efficient SI deconvolution method. Specifically, we model the imaging system as a multi-rate filter bank, where each plane along the optical axis is assigned to a channel with a different PSF; the filter bank structure leads to a Landweber deconvolution that uses an iterative-shrinkage-thresholding algorithm (ISTA).

This chapter is organized as follows. In Section 5.2, we introduce the image formation model and the inverse problem. In Section 5.3, we describe the proposed method. In Section 5.4, we characterize the algorithm on simulated images. In Section 5.5, we finally offer our conclusions.

5.2 Problem Statement

We consider a 3D object with local intensity $f(\mathbf{x}, z)$, $\mathbf{x} = (x, y) \in \mathbb{R}^2, z \in \mathbb{R}$, imaged with a system characterized by 3D PSFs $h_i(\mathbf{x}, z)$ that are dependent on the axial position (depth) of the microscope stage $d_i = i\Delta d$, where Δd is the uniform step by which the stage is moved between the acquisition of each slice during optical sectioning. The 2D blurred image acquired by the camera for stage position $d = d_i$ can then be modeled as:

$$g_i(\mathbf{x}) \overset{\text{def}}{=} \iiint_{\mathbb{R}^3} f(\boldsymbol{\xi}, \eta) \cdot h_i^\top(\boldsymbol{\xi} - \mathbf{x}, \eta) \, \mathrm{d}\boldsymbol{\xi}\mathrm{d}\eta + n_i(\mathbf{x}), \qquad i = 0, \dots, M-1 \quad (5.1)$$
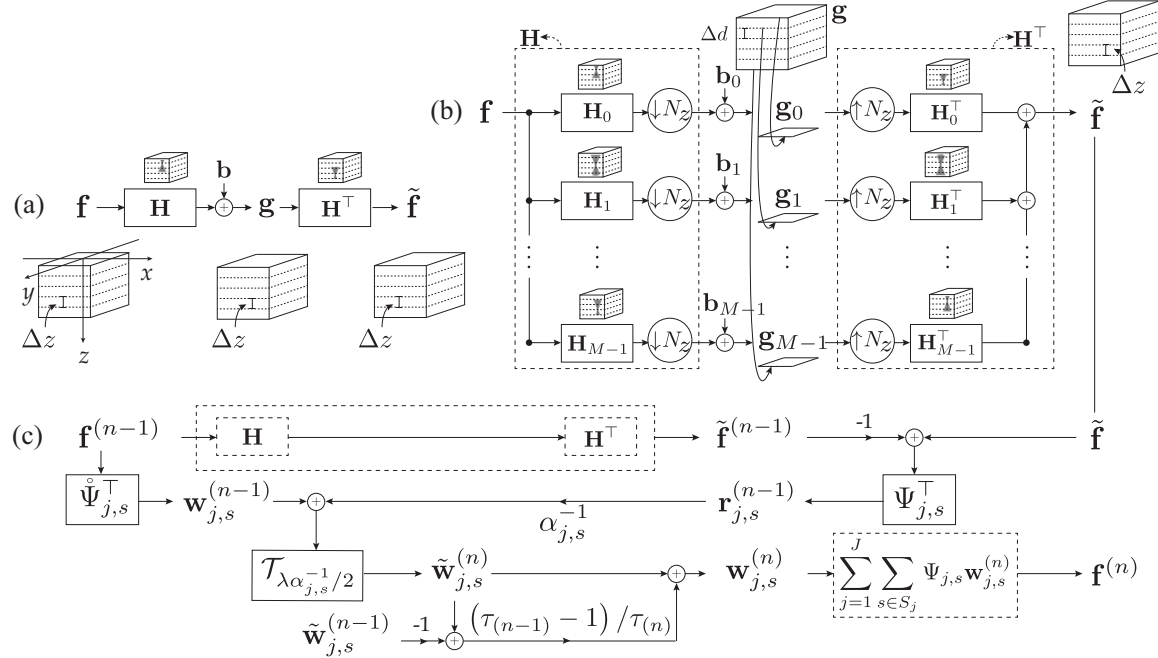
Figure 5.2: Block diagram of shift-invariant FISTA deconvolution (SI-FISTA, (a)+(c)) and proposed depth-variant FISTA deconvolution (DV-FISTA = (b) + (c)). Both algorithms are based on a *reblurring* operation and Landweber iterations: (a) reblurring in SI-FISTA [114, 115]; (b) reblurring in proposed DV-FISTA; (c) thresholded Landweber deconvolution: the structure and complexity of the thresholding stage remains the same for SI-FISTA and DV-FISTA.

for the i-th measured slice, where $h_i^\top(\mathbf{x}, z) \stackrel{\text{def}}{=} h_i(-\mathbf{x}, -z)$, and n_i denotes additive measurement noise. Note that this model is laterally shift-invariant and axially shift-variant, since we do not require $h_i(\mathbf{x}, z) = h_0(\mathbf{x}, d_i + z)$.

We sample f and h_i on a discrete 3D grid with $N_x \times N_y \times N_z$ voxels, with lateral and axial sampling steps $\Delta\mathbf{x}$ and Δz, respectively. Similarly, we sample g_i to form an $N_x \times N_y$ image, with lateral sampling step $\Delta\mathbf{x}$. Note that the stage position $i\Delta d$ (associated to image g_i) can be different from $i\Delta z$ (the position of the i-th slice in f) [112]. This mismatch is captured by the space variant PSF model, which we assume is known a priori. After discretization, Eq. (5.1) can be rewritten in terms of matrices as:

$$\mathbf{g}_i \stackrel{\text{def}}{=} \mathbf{D}\mathbf{H}_i\mathbf{f} + \mathbf{n}_i, \tag{5.2}$$

where $\mathbf{H}_i$ are $(N_x \cdot N_y \cdot N_z) \times (N_x \cdot N_y \cdot N_z)$-sized block-circulant matrices (for 3D circular convolution with h_i), $\mathbf{D}$ is the $(N_x \cdot N_y) \times (N_x \cdot N_y \cdot N_z)$-sized down-sampling matrix that selects only the first z-plane of $\mathbf{H}_i\mathbf{f}$, and where $\mathbf{g}_i, \mathbf{f}$ and $\mathbf{n}_i$ are vectors containing lexicographically arranged samples of g_i, f and n_i, respectively. The individual slices can then be grouped together to be represented as:

$$\mathbf{g} \stackrel{\text{def}}{=} \begin{pmatrix} \mathbf{g}_0 \\ \vdots \\ \mathbf{g}_{M-1} \end{pmatrix} = \begin{pmatrix} \mathbf{DH}_0 \\ \vdots \\ \mathbf{DH}_{M-1} \end{pmatrix} \mathbf{f} + \begin{pmatrix} \mathbf{n}_0 \\ \vdots \\ \mathbf{n}_{M-1} \end{pmatrix} \stackrel{\text{def}}{=} \mathbf{Hf} + \mathbf{n}. \tag{5.3}$$

The inverse problem that we wish to solve is to find an estimate $\bar{\mathbf{f}}$ of $\mathbf{f}$, given $\mathbf{g}$ and $\mathbf{H}$. We follow a transform-domain sparsity-based reconstruction approach [28, 114, 115] that assumes $\mathbf{f}$ has a sparse wavelet representation $\mathbf{f} = \Psi\mathbf{w}$, where Ψ is the synthesis matrix whose columns are the elements of the wavelet basis and $\mathbf{w}$ is a set of (sparse) wavelet coefficients. The estimate $\bar{\mathbf{f}} = \Psi\bar{\mathbf{w}}$ is found via minimization of the cost function:

$$\mathcal{C}(\mathbf{w}) \stackrel{\text{def}}{=} \|\mathbf{g} - \mathbf{H}\Psi\mathbf{w}\|_{\ell_2}^2 + \lambda\|\mathbf{w}\|_{\ell_1}, \tag{5.4}$$

$$= \sum_{i=0}^{M-1} \|\mathbf{g}_i - \mathbf{DH}_i\Psi\mathbf{w}\|_{\ell_2}^2 + \lambda\|\mathbf{w}\|_{\ell_1}, \tag{5.5}$$

where λ is a non-negative scalar quantity controlling wavelet regularization. Efficient solutions to this problem have been proposed for the shift-invariant case when $\mathbf{H}$ is block circulant using Shannon [114] and generic wavelet bases [115] with the sub-band dependent ISTA (Fig. 5.2 (a) and (c)). We have previously showed that this method remained applicable in the context of multi-view microscopy with an equivalent computational complexity as single-view processing [17]. Although our axially depth-variant (DV) deconvolution problem also has the similar form of a multi-channel filter-bank, the

95

down- and up-sampling operations (Fig. 5.2 (b)) require additional adjustments for the implementation to be efficient, as detailed in the section below.

5.3 Method

Vonesch and Unser [114, 115] have introduced an efficient multi-level sub-band dependent ISTA solution to the minimization problem defined in Eq. (5.5) by considering the wavelet decomposition $\mathbf{f} = \Psi\mathbf{w} = \sum_{j=1}^{J} \sum_{s \in S_j} \Psi_{j,s}\mathbf{w}_{j,s}$, where $\mathbf{w}_{j,s} = \mathring{\Psi}_{j,s}^{\top}\mathbf{f}$ denotes the wavelet coefficients in the sub-band $s \in S_j$ at scale j that is characterized by its analysis and synthesis matrices $\mathring{\Psi}_{j,s}$ and $\Psi_{j,s}$, respectively. These notations are similar to those described in Chapter 4. The ISTA solution involves alternating between two steps: (i) a Landweber update of the wavelet coefficients from the previous iteration, and (ii) wavelet sub-band weighted soft-thresholding of the coefficients computed in (i). The performance of ISTA can be further sped up by computing the next iterate based not only on the previous one, but also on two or more previously computed iterates (fast ISTA, (FISTA) [5]). The steps of the minimization scheme can be outlined as follows:

$$\mathbf{w}_{j,s}^{(n)} \stackrel{\text{def}}{=} \tilde{\mathbf{w}}_{j,s}^{(n)} + \left(\frac{\tau_{(n-1)} - 1}{\tau_{(n)}} \right) \left(\tilde{\mathbf{w}}_{j,s}^{(n)} - \tilde{\mathbf{w}}_{j,s}^{(n-1)} \right), \tag{5.6}$$

where $\mathbf{w}_{j,s}^{(n)}$ are the wavelet coefficients in the sub-band s at scale j during the n-th iteration, and the temporary coefficients:

$$\tilde{\mathbf{w}}_{j,s}^{(n)} \stackrel{\text{def}}{=} \mathcal{T}_{\lambda\alpha_{j,s}^{-1}/2} \left\{ \mathbf{w}_{j,s}^{(n-1)} + \alpha_{j,s}^{-1}\mathbf{r}_{j,s}^{(n-1)} \right\}, \tag{5.7}$$

are obtained via the soft-thresholding operation defined in Eq. (4.32), with the subband dependent residuals defined as:

$$\mathbf{r}_{j,s}^{(n-1)} \stackrel{\text{def}}{=} \Psi_{j,s}^{\top} \mathbf{H}^{\top} \left(\mathbf{g} - \mathbf{H} \sum_{j=1}^{J} \sum_{s' \in S_j} \Psi_{j,s'} \mathbf{w}_{j,s'}^{(n-1)} \right), \tag{5.8}$$

with the weighing factors defined as:

$$\tau_{(n)} \stackrel{\text{def}}{=} \frac{1 + \sqrt{1 + 4\tau_{(n-1)}^2}}{2}, \tag{5.9}$$

$$\alpha_{j,s} \geq \sum_{s' \in S_j} \rho \left(\Psi_{j,s'}^{\top} \mathbf{H}^{\top} \mathbf{H} \Psi_{j,s} \right), \qquad \forall s \in S_j. \tag{5.10}$$

The weights $\alpha_{j,s}$ for the subband $s \in S_j$ at scale j are obtained from the spectral radius operator ρ [37] which greatly accelerate convergence [115]. Commonly used initial conditions include $\tau_{(0)} = 1$ and $\tilde{\mathbf{w}}_{j,s}^{(0)} = \mathbf{w}_{j,s}^{(0)} = \mathring{\Psi}_{j,s}^{\top} \mathbf{g}$. The block diagram of this minimization approach is summarized in Fig. 5.2.

We emphasize that the matrix formulation is only formal as the matrices' large sizes are computationally prohibitive in practice. Efficient implementations of this algorithm have been derived when $\mathbf{H}^{\top}\mathbf{H}$ is block circulant [114, 115, 17], which, however, is not the case for the DV problem at hand (due to the axial downsampling-upsampling operations). Therefore, we have derived efficient ways to compute (a) $\mathbf{H}^{\top}\mathbf{H}$, and (b) the sub-band dependent constants $\alpha_{j,s}$. Note that although $\mathbf{H}^{\top}\mathbf{H}$ is not block-circulant, each $\mathbf{H}_i$ is block-circulant and all operations executed in the analysis and synthesis side of the filter-bank can still be computed using only point-wise multiplications and additions using 3D discrete Fourier transforms (DFT). Specifically, the equivalent implementation

of $\tilde{\mathbf{f}} = \mathbf{H}^\top \mathbf{g}$ and $\tilde{\mathbf{f}}^{(n)} = \mathbf{H}^\top \mathbf{H} \mathbf{f}^{(n)}$ using 2D/3D DFTs is given by:

$$\hat{\tilde{f}}[\mathbf{u}, w] = \sum_{k=0}^{M-1} \hat{g}_k[\mathbf{u}] \cdot \hat{h}_k^*[\mathbf{u}, w], \tag{5.11}$$

$$\hat{\tilde{f}}^{(n)}[\mathbf{u}, w] = \sum_{k=0}^{M-1} \left(\sum_{\ell=0}^{N_z-1} \frac{\hat{h}_k[\mathbf{u}, \ell] \cdot \hat{f}^{(n)}[\mathbf{u}, \ell]}{N_z} \right) \hat{h}_k^*[\mathbf{u}, w], \tag{5.12}$$

where $\hat{a}$ (and $\hat{a}^*$) denotes the 2D/3D DFT (and its complex-conjugate) of discrete image/volume a, $\mathbf{u} = [u, v]$, for $0 \leq u < N_x$, $0 \leq v < N_y$, and $0 \leq w < N_z$. Using similar expressions, we determine the sub-band dependent weights $\alpha_{j,s}$ in Eq. (5.10) using the power method [37] for an undecimated wavelet decomposition as:

$$\alpha_{j,s} = \lim_{m \to \infty} \sum_{s' \in S_j} \frac{\sum_{\mathbf{u}, w} \left(\hat{b} \cdot \hat{a}_{j,s',s}^{(m)} \right)[\mathbf{u}, w]}{\sum_{\mathbf{u}', w'} \left(\hat{b} \cdot \hat{a}_{j,s',s}^{(m-1)} \right)[\mathbf{u}', w']}, \tag{5.13}$$

$$\hat{a}_{j,s',s}^{(m)}[\mathbf{u}, w] = \sum_{i=0}^{M-1} \left(\sum_{\ell=0}^{N_z-1} \frac{\left(\hat{h}_i \cdot \hat{\psi}_{j,s} \cdot \hat{a}_{j,s',s}^{(m-1)} \right)[\mathbf{u}, \ell]}{N_z} \right) \cdot \left(\hat{\psi}_{j,s'}^* \cdot \hat{h}_i^* \right)[\mathbf{u}, w], \tag{5.14}$$

where $\hat{\psi}_{j,s}$ denotes the DFT of the wavelet (or scaling function) that spans the subspace associated with sub-band s at scale j, while $\hat{b}$ and $\hat{a}_{j,s',s}^{(0)}$ are random (nonzero) signals. This can be readily extended for a wavelet decomposition scheme with dyadic sub-sampling by aliasing the frequency components of $\hat{a}_{j,s',s}^{(m)}$ ($s', s \in S_j$) in Eq. (5.14) to be periodic by $N_x/2^j, N_y/2^j$ and $N_z/2^j$, along x, y and z, respectively. Good estimates of $\alpha_{j,s}$ can be obtained from as few as 10 iterations in Eq. (5.13).

5.4   Experimental Results

In order to illustrate the performance of our algorithm, we considered a 3D stack $(64 \times 64 \times 64)$ with 15 point sources located at different axial positions (Fig. 5.3(a-b)).

We next generated $M = 64$ blurred 2D observations using the following PSF parameters (Fig. 5.1): objective NA $= 0.9$, $n_i = 1$, working distance $t_i = 1.9$mm, $n_g = 1.515$, thickness of cover-glass $t_g = 175\mu$m, $n_s = 1.33$, $\Delta x = \Delta y = 0.5\mu$m, $\Delta z = 0.8\mu$m, $\Delta d = 0.59\mu$m. We added Gaussian white noise to the blurred result (Fig. 5.3(c)) with noise variance set such that the blurred signal-to-noise ratio (BSNR) [114] was 40 dB.

We conducted two independent deconvolution experiments with the blurred observations. In the first case, we applied spatially-invariant FISTA deconvolution (SI-FISTA, adapted from [115] using a Level-1 cubic spline dyadic wavelet decomposition and $\lambda = 0.1$), where we used only a single 3D PSF at a time (either h_0, h_{20}, h_{40}, h_{60}, or the mean of all 64 PSFs h_{mean}, after compensating for axial-shift). Since the PSF shape varies with depth, none is appropriate as is evident from the deconvolved volume estimated with h_{mean} after 50 iterations (Fig. 5.3(d)). Next, we used our proposed depth-variant FISTA deconvolution (DV-FISTA) to estimate the deconvolved volume using 64 different PSFs (Fig. 5.3(e)), with all other parameters set similar to the SI-FISTA experiment. As illustrated in Fig. 5.3(e), the reconstructed volume has fewer artifacts when compared to Fig. 5.3(d). The evolution of the *signal-to-error* gain (SERG) in both experiments is shown in (Fig. 5.3(f)), where

$$\mathrm{SERG}(\mathbf{f}') \overset{\text{def}}{=} 20 \log_{10} \left(\frac{\|\mathbf{g} - \mathbf{f}\|_{\ell_2}}{\|\mathbf{f}' - \mathbf{f}\|_{\ell_2}} \right). \tag{5.15}$$

We implemented the algorithm in Matlab (R2011b) and ran the experiments on a Windows 64-bit machine, equipped with a dual-core Intel Xeon 3.4-GHz CPU and 16 GB RAM. The pre-computation of the sub-band dependent weight constants ($\alpha_{j,s}$) for the given set of parameters was done using 10 iterations of the power method in Eq. (5.13), which took about 1 minute per iteration. Note that computation of these weights is only required once for a given imaging setup (i.e. all frames of a time-lapse would use the

same weights). The iterative image reconstruction process took about 5.5 seconds per iteration, of which 5 seconds were spent computing the reblurred signal by applying $\mathbf{H}^\top\mathbf{H}$. In contrast, the shift-invariant method took about 0.55 seconds for each iteration. In both cases, updating the wavelet coefficients by soft-thresholding the Landweber update is computed in 0.5 seconds, since the DV filter-bank structure does not introduce any additional complexity (Fig. 5.2(c)). These results are in line with the theoretical complexity, whose order is M times more complex than that of the shift-invariant method. Because the computation in each of the M-channels could be done independently of that of the other channels, the workload could be delegated to a cluster of computers at each iteration to bring down the effective computation time.

5.5 Conclusion

We have presented a fast ISTA algorithm for the joint deconvolution and fusion problem with PSFs that are depth-variant. The algorithm naturally handles differing sampling steps associated with the blurred data stack (stage position step Δd) and the PSF kernel (Δz). Also, the multi-channel framework can handle a number of blurred z-slices (M) independent of the dimensions of the PSF kernel and reconstruction (in practice, we set $M \geq N_z$), which could even be non-uniformly spaced. Furthermore, since the proposed DV-FISTA is applied to the entire dataset rather than blocks, it does not require post-processing operations with suitable transition masks to fuse individually deblurred sub-regions in the data.
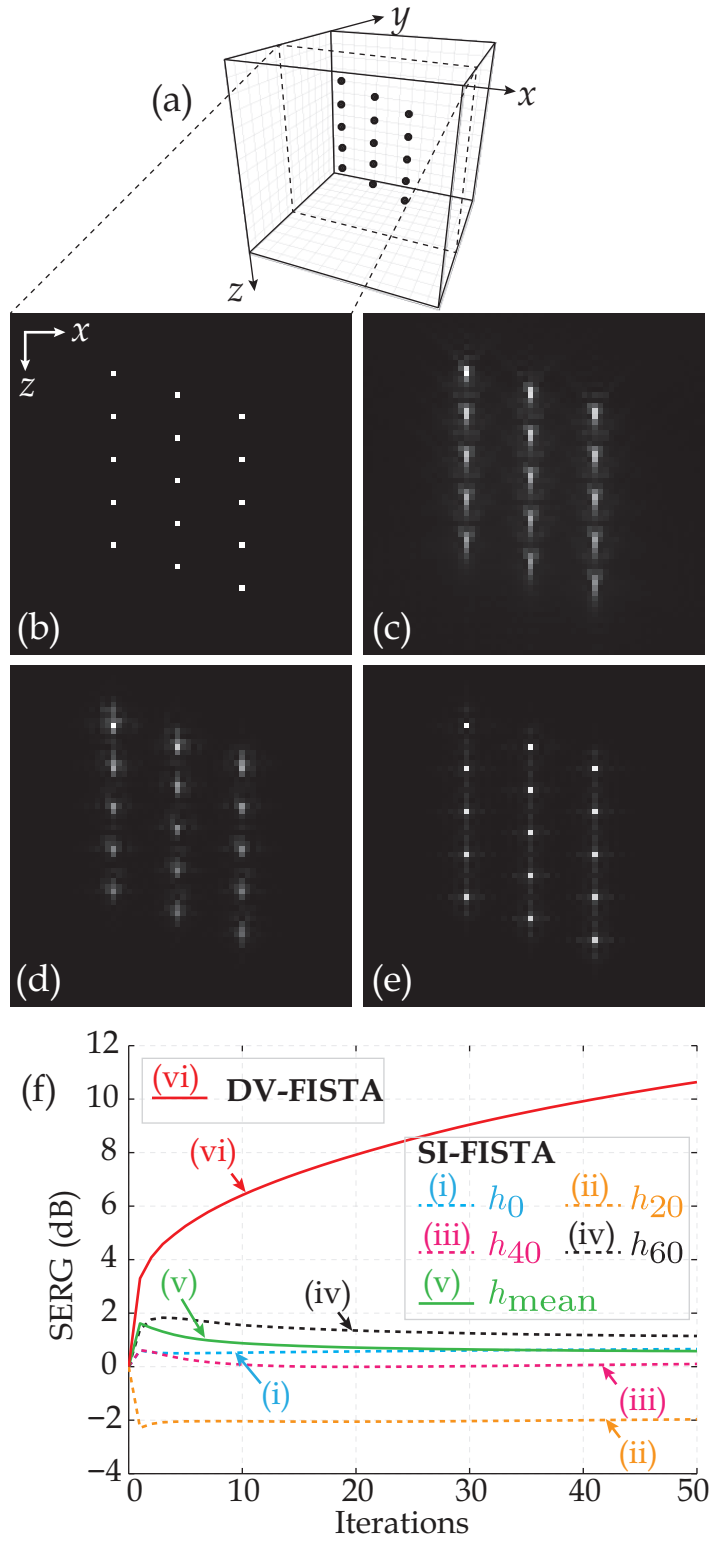
Figure 5.3: Deconvolution results: (a)-(b) f, (c) g, (d) SI-FISTA result (using h_{mean}), (e) DV-FISTA result, (f) SERG comparison of the SI-FISTA and DV-FISTA results.

Chapter 6

Non-redundant Temporal Registration for In Vivo Cardiac Microscopy

Abstract[12]

Dynamic time warping (DTW) permits the elastic alignment of an input time sequence to a reference. Here, we propose quasi-periodic dynamic time warping (QPDTW), a variant of DTW, for signals derived from quasi-periodic processes. Our method is capable of both temporally warping and wrapping the input sequence by allowing for jump discontinuities in the non-linear alignment function akin to those found in wrapped phase functions. This enables input sequences to have durations as short as a single cycle starting at any arbitrary phase, for reference sequences with any arbitrary duration. Our method is particularly useful in cardiac imaging for applications such as the synchronization of 2D + time image sequences to reconstruct 3D + time volumetric sequences, virtual frame-

---

[12]This chapter is based on the reference [14] co-authored with K. Chan, J. Ohn, S. Bhat, and M. Liebling, and is deployed in the reference [84] co-authored with C. Ramspacher *et al.* to study the implications of developmental aberrations in heart biomechanics.

rate improvement via reordering of sequences, and noise reduction by the utilization of multiple time-points with an equivalent phase. We evaluate our method via experiments on simulated 1D signals, B-spline based heart phantoms, and in vivo cardiac sequences acquired in live transgenic zebrafish embryos using fluorescence microscopy.

6.1   Introduction

The development and dynamics of the living vertebrate heart is widely studied in modern biology using model organisms such as zebrafish, mice, quails, and chicks. This typically requires imaging the beating embryonic heart as volumes using various imaging modalities at different stages of its morphological development. Several imaging techniques have been employed for this purpose such as confocal microscopy [64], optical coherence tomography (OCT) [48, 58], and light-sheet microscopy [47, 106]. However, the imaging speed of these techniques is currently not high enough to capture the dynamics of fast moving cardiovascular structures in 3D and time concurrently. Although hardware advances have allowed to effectively acquire 3D volumes of the beating heart [31], the number of optical sections that can be acquired is still limited.

The speed limitation of current imaging techniques can be mitigated by exploiting the repetitive heart motion and acquiring several 2D + time sequences separately that are finally used together to reconstruct dynamic volumes. Such approaches require either prospective or retrospective gating. Prospective gating techniques work by only triggering snapshots at a desired phase in the cardiac cycle via hardware customization [102, 101]. Retrospective gating techniques, on the other hand, rely on image processing algorithms for the temporal registration of unsynchronized sequences [64]. To ensure that a full cardiac cycle (starting at the same cardiac phase as the reference) is available within the data at the time of post-processing, retrospective gating methods often require that
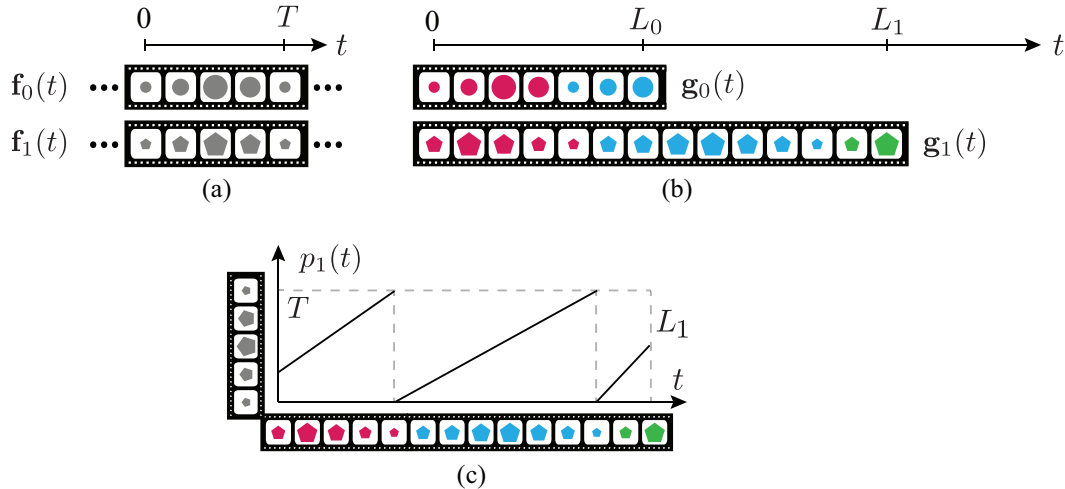
Figure 6.1: Our imaging model comprises (a) periodic sequences $\mathbf{f}_k(t) = \mathbf{f}_k(t + T)$, related to (b) quasi-periodic (measured) sequences $\mathbf{g}_k(t) = \mathbf{f}_k(p_k(t))$, $0 \leq t \leq L_k$, via (c) phase functions p_k, $k = 0, 1$.

at least two cardiac cycles be collected, which increases both collection time and size, potentially damaging the samples.

In this work, we address the limitations of (non-)rigid temporal registration algorithms used in retrospective gating by deriving a modified dynamic time warping (DTW) technique applicable for quasi-periodic signals. Our method enables the input sequence to be temporally *wrapped* (in addition to being *warped*) in order to match a reference signal, thereby alleviating the constraints on the minimal duration of the data collected. We also show how such a framework can be used when multiple cycles are available in a single quasi-periodic sequence to infer intermediary frames by rearrangement and to reduce noise by combining frames of equivalent phases.

This work is organized as follows. We introduce our imaging model in Section 6.2 and discuss the existence of functions capable of warping a quasi-periodic sequence to match a reference in Section 6.3. We describe our proposed algorithms for synchronization, re-binning, and compounding discrete-time quasi-periodic sequences in Section 6.4. We discuss practical applications of our algorithms for cardiac imaging in Section 6.5. We

present our simulations and experimental evaluations in Section 6.6. We discuss the features of our method in Section 6.7 and finally conclude in Section 6.8.

6.2   Model of Quasi-Periodic Signals

We consider two vectors $\mathbf{f}_0(t)$ and $\mathbf{f}_1(t)$, each with P time-dependent components:

$$\mathbf{f}_k(t) \overset{\text{def}}{=} \begin{pmatrix} f_{k,0}(t) \\ \vdots \\ f_{k,P-1}(t) \end{pmatrix} \in \mathbb{R}^P, \qquad t \in \mathbb{R}, \quad k = 0, 1. \quad (6.1)$$

The signals are T-periodic:

$$\mathbf{f}_k(t) \overset{\text{def}}{=} \mathbf{f}_k(t + T), \qquad\qquad t \in \mathbb{R}, \quad k = 0, 1. \quad (6.2)$$

We will further assume that $\mathbf{f}_0$ and $\mathbf{f}_1$ are in synchrony, and that time-shifts by an integer number of periods $s = nT$, $n \in \mathbb{Z}$, in $\mathbf{f}_0$ minimize the following quantity:

$$\mathcal{Q}(s) \overset{\text{def}}{=} \int_0^T \Psi\left(\mathbf{f}_0(t + s), \mathbf{f}_1(t)\right) \mathrm{d}t, \qquad\qquad (6.3)$$

where $\Psi : \mathbb{R}^P \times \mathbb{R}^P \to \mathbb{R}$ is a dissimilarity function such as the ℓ_1-norm of the difference of the input vectors:

$$\Psi_{\ell_1}\left(\mathbf{a}, \mathbf{b}\right) \overset{\text{def}}{=} \|\mathbf{a} - \mathbf{b}\|_1, \qquad\qquad \mathbf{a}, \mathbf{b} \in \mathbb{R}^P. \quad (6.4)$$

We next define two quasi-periodic sequences $\mathbf{g}_0$ (reference) and $\mathbf{g}_1$ (input) by warping the time axis of the periodic sequences $\mathbf{f}_0$ and $\mathbf{f}_1$ via phase functions ϕ_0 and ϕ_1,

respectively:

$$\mathbf{g}_k(t) \overset{\text{def}}{=} \mathbf{f}_k(\phi_k(t)), \qquad\qquad 0 \le t \le L_k, \quad k = 0, 1, \quad (6.5)$$

where $\phi_0(0) \overset{\text{def}}{=} 0$ and $\phi_1(0) \in [0, T)$. We only consider phase functions $\phi_k : [0, L_k] \to [\phi_k(0), \phi_k(L_k)]$ that are continuous, differentiable, and monotonically increasing. We also assume that their derivatives are bounded by $\alpha_{\min}$ and $\alpha_{\max}$:

$$\alpha_{\min} \le \frac{\mathrm{d}}{\mathrm{d}t}\phi_k(t) \le \alpha_{\max}, \qquad\qquad 0 \le t \le L_k, \quad (6.6)$$

where $0 < \alpha_{\min} \le 1 \le \alpha_{\max}$. The duration of the shortest and longest cycles possible in $\mathbf{g}_0$ and $\mathbf{g}_1$ can then be inferred as $T_{\min} = T/\alpha_{\max}$ and $T_{\max} = T/\alpha_{\min}$, respectively.

We define $\eta_k \in \mathbb{R}^+$, the (possibly non-integer) number of cycles in $\mathbf{g}_k$, as:

$$\eta_k \overset{\text{def}}{=} \frac{\phi_k(L_k) - \phi_k(0)}{T}, \qquad\qquad (6.7)$$

which lies in the range:

$$\frac{L_k}{T_{\max}} \le \eta_k \le \frac{L_k}{T_{\min}}. \qquad\qquad (6.8)$$

We define $p_k : [0, L_k] \to [0, T)$, the T-wrapped phase function of ϕ_k, as:

$$p_k(t) \overset{\text{def}}{=} \mathcal{W}_T\left(\phi_k(t)\right), \qquad\qquad 0 \le t \le L_k, \quad k = 0, 1, \quad (6.9)$$

where $\mathcal{W}_T : \mathbb{R} \to [0, T)$ represents the T-wrapping operator:

$$\mathcal{W}_T(x) \overset{\text{def}}{=} x - \left\lfloor \frac{x}{T} \right\rfloor T, \qquad\qquad (6.10)$$

with $\lfloor \cdot \rfloor$ denoting the floor operator. Since $\mathbf{f}_k$ is T-periodic, the relation between $\mathbf{f}_k$ and
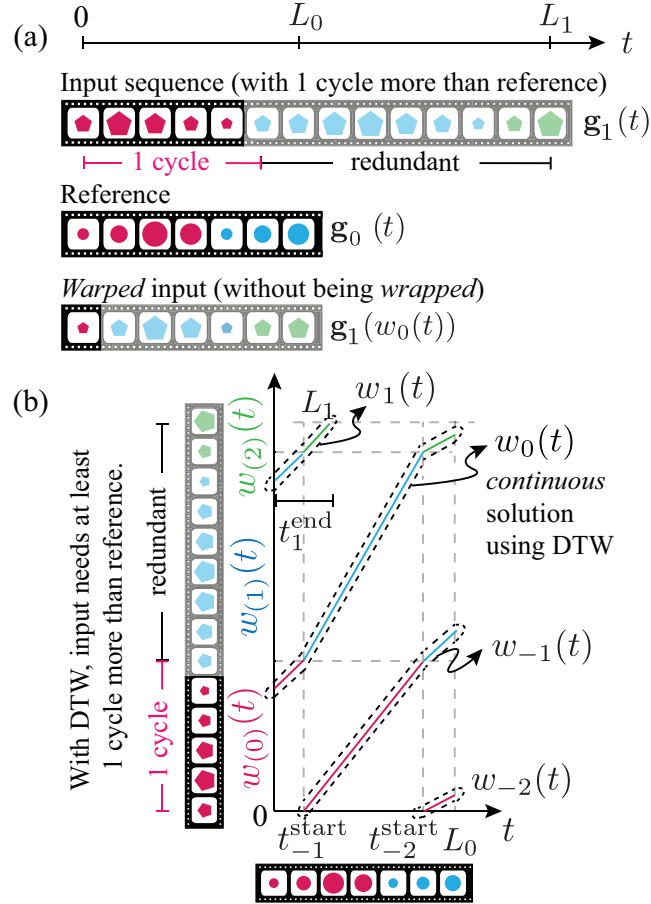
Figure 6.2: We seek a temporal re-warping function that warps $\mathbf{g}_1$ to match the phase of $\mathbf{g}_0$. (a-b) If $\mathbf{g}_1$ spans at least one cycle more than $\mathbf{g}_0$ ($\eta_1 \geq \eta_0 + 1$), there exists at least one *continuous* and monotonically increasing re-warping function w_0. (c-d) If $\mathbf{g}_1$ spans at least one cycle ($\eta_1 \geq 1$), there exists at least one *piece-wise continuous* re-warping function $w_{(0)}$. The colors represent different cycles in the sequences.

$\mathbf{g}_k$, expressed in Eq. (6.5), can also be written using p_k as:

$$\mathbf{g}_k(t) \stackrel{\text{def}}{=} \mathbf{f}_k\left(p_k(t)\right), \qquad\qquad 0 \leq t \leq L_k, \quad k = 0, 1, \quad (6.11)$$

which is illustrated in Fig. 6.1.

Table 6.1: Notations used in the quasi-periodic imaging model.

| Symbol	Meaning
$\mathbf{f}_0(t), \mathbf{f}_1(t)$	T-periodic & pre-synchronized time-sequences
$\mathbf{g}_0(t), \mathbf{g}_1(t)$	Quasi-periodic time-sequences
L_k	Time-length of $\mathbf{g}_k$, $k = 0, 1$
η_k	No. of quasi-periodic cycles in $\mathbf{g}_k$, $k = 0, 1$
$\phi_k(t)$	Phase function for $\mathbf{g}_k$, $k = 0, 1$
$p_k(t)$	T-wrapped form of ϕ_k, $k = 0, 1$
$w_j(t)$	Continuous re-warping functions
$w_{(j)}(t)$	Piece-wise continuous re-warping functions
$w_{\min}, w_{\max}$	Min., max. value of $\mathrm{d}w_j(t)/\mathrm{d}t$
$T_{\min}, T_{\max}$	Min., max. time-period of cycles in $\mathbf{g}_0$ & $\mathbf{g}_1$
$\mathbf{g}_k[n] = \mathbf{g}_k(n\Delta t)$	Temporally sampled $\mathbf{g}_k$, $k = 0, 1$
$\tilde{\mathbf{g}}_k[n] \approx \mathbf{g}_k(n\Delta t/\rho)$	Temporally over-sampled $\mathbf{g}_k$, $k = 0, 1$
N_k	No. of discrete time points in $\mathbf{g}_k$, $k = 0, 1$
$\tilde{N}_k$	No. of discrete time points in $\tilde{\mathbf{g}}_k$, $k = 0, 1$
$\tilde{w}_j[n]$	Discrete estimate of w_j
$\tilde{w}_{(j)}[n]$	Discrete estimate of $w_{(j)}$
$\Delta w_{\min}, \Delta w_{\max}$	Min., max. value of $\tilde{w}_j[n] - \tilde{w}_j[n-1]$
$\tilde{T}_{\min}, \tilde{T}_{\max}$	Min., max. discrete time-period of cycles in $\tilde{\mathbf{g}}_k$
Ψ	Dissimilarity function in objective function
Γ	Regularization function in objective function
ξ	Max. no. of discontinuities allowed in solution
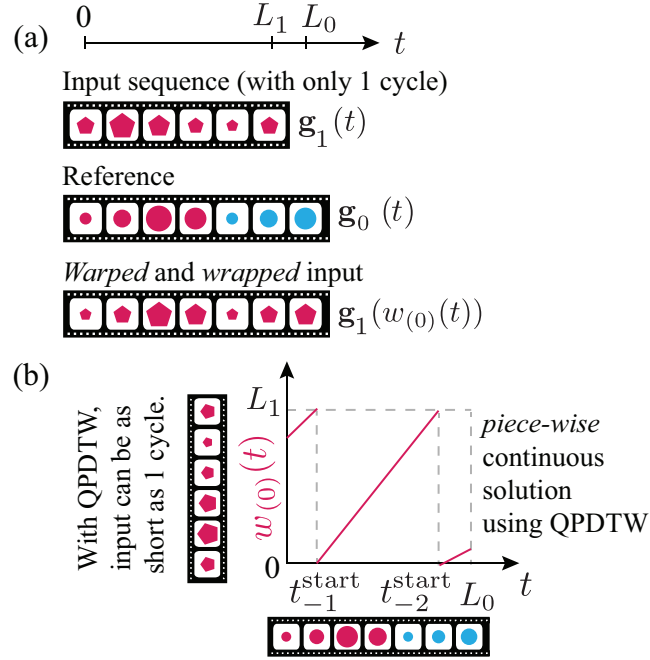
Figure 6.3: We seek a temporal re-warping function that warps $\mathbf{g}_1$ to match the phase of $\mathbf{g}_0$. (a-b) If $\mathbf{g}_1$ spans at least one cycle more than $\mathbf{g}_0$ ($\eta_1 \geq \eta_0 + 1$), there exists at least one *continuous* and monotonically increasing re-warping function w_0. (c-d) If $\mathbf{g}_1$ spans at least one cycle ($\eta_1 \geq 1$), there exists at least one *piece-wise continuous* re-warping function $w_{(0)}$. The colors represent different cycles in the sequences.

6.3   Existence of Re-warping Functions

We examine the existence of functions w that satisfy:

$$p_1\left(w(t)\right) \stackrel{\text{def}}{=} p_0(t), \tag{6.12}$$

so that applying w to $\mathbf{g}_1$ re-warps it as:

$$\mathbf{g}_1\left(w(t)\right) = \mathbf{f}_1\left(p_0(t)\right), \tag{6.13}$$

matching the phase of the input $\mathbf{g}_1$ to that of the reference $\mathbf{g}_0$. We recall that, by definition, $\mathbf{f}_1$ is in synchrony with $\mathbf{f}_0$ and $\mathbf{g}_0(t) = \mathbf{f}_0\left(p_0(t)\right)$ [see Eq. (6.11)]. Re-warping

functions w that satisfy Eq. (6.12) for any $t \in [0, L_0]$ are guaranteed to exist when $\mathbf{g}_1$ spans at least one period, i.e. $\eta_1 \geq 1$, or, equivalently, when $L_1 \geq T_{\max}$, which ensures that all phases potentially contained in $\mathbf{g}_0$ are also contained in $\mathbf{g}_1$.

In the following subsections, we will explore the conditions for the existence of re-warping functions $w(t)$ valid over all or part of the interval $t \in [0, L_0]$ and that are either *continuous* or *piece-wise continuous*.

6.3.1   Continuous Re-warping Functions

If $\mathbf{g}_1$ spans at least one cycle more than $\mathbf{g}_0$, i.e. $\eta_1 \geq \eta_0 + 1$ (which is guaranteed when $L_1 \geq L_0 T_{\max}/T_{\min} + T_{\max}$), then there exist $J \geq 1$ *continuous* and monotonically increasing re-warping functions that satisfy Eq. (6.12) for all $t \in [0, L_0]$. These functions are obtained as:

$$w_j(t) \stackrel{\text{def}}{=} \begin{cases} \phi_1^{-1} \left(\phi_0(t) + jT \right), & \text{if } p_1(0) = 0 \\[2mm] \phi_1^{-1} \left(\phi_0(t) + (j+1)T \right), & \text{otherwise,} \end{cases} \tag{6.14}$$

for $j = 0, \ldots, J - 1$, where J is given by:

$$J \stackrel{\text{def}}{=} \begin{cases} \left\lfloor \frac{\phi_1(L_1) - \phi_0(L_0)}{T} \right\rfloor + 1, & \text{if } p_1(0) = 0 \\[2mm] \left\lfloor \frac{\phi_1(L_1) - \phi_0(L_0)}{T} \right\rfloor, & \text{otherwise.} \end{cases} \tag{6.15}$$

In addition, there also exist I *continuous* and monotonically increasing re-warping functions $w_j(t)$, $j = -1, -2, \ldots, -I$, defined as in Eq. (6.14), that satisfy Eq. (6.12) for

only $t \in [t_j^{\text{start}}, L_0]$, with:

$$
t_j^{\text{start}} \stackrel{\text{def}}{=}
\begin{cases}
\phi_0^{-1}\left(p_1(0) - jT\right), & \text{if } p_1(0) = 0 \\[2ex]
\phi_0^{-1}\left(p_1(0) - (j+1)T\right), & \text{otherwise,}
\end{cases}
\tag{6.16}
$$

and

$$
I \stackrel{\text{def}}{=}
\begin{cases}
\left\lfloor \frac{\phi_0(L_0) - p_1(0)}{T} \right\rfloor, & \text{if } p_1(0) = 0 \\[2ex]
\left\lfloor \frac{\phi_0(L_0) - p_1(0)}{T} \right\rfloor + 1, & \text{otherwise.}
\end{cases}
\tag{6.17}
$$

Additionally, there exist K *continuous* and monotonically increasing re-warping functions $w_j(t)$, $j = J, J+1, \ldots, J+K-1$, defined as in Eq. (6.14), and that satisfy Eq. (6.12) for only $t \in [0, t_j^{\text{end}}]$, with:

$$
t_j^{\text{end}} \stackrel{\text{def}}{=} \phi_0^{-1}\left(p_1(L_1) + (J + K - 1 - j)T\right),
\tag{6.18}
$$

and

$$
K \stackrel{\text{def}}{=} \left\lceil \frac{\phi_0(L_0) - p_1(L_1)}{T} \right\rceil,
\tag{6.19}
$$

where $\lceil \cdot \rceil$ denotes the ceiling operator.

These *continuous* and monotonically increasing re-warping functions are shown in Fig. 6.2(a-b). Note that for a given pair of integers k and ℓ, where $k < \ell$, we have (i) $w_k(t) < w_\ell(t)$, (ii) $t_k^{\text{start}} > t_\ell^{\text{start}}$, and (iii) $t_k^{\text{end}} > t_\ell^{\text{end}}$, when they are each defined.

Using the relations in Eqs. (6.6) and (6.14), the minimum and maximum values of the derivatives of re-warping functions w_j are given by $w_{\min}$ and $w_{\max}$:

$$
w_{\min} = \frac{\alpha_{\min}}{\alpha_{\max}} \leq \frac{\mathrm{d}}{\mathrm{d}t} w_j(t) \leq w_{\max} = \frac{\alpha_{\max}}{\alpha_{\min}}.
\tag{6.20}
$$

When the quasi-periodic sequences $\mathbf{g}_0$ and $\mathbf{g}_1$ are identical to each other, there is only

one *continuous* and monotonically increasing re-warping function that satisfies Eq. (6.12) for all $t \in [0, L_0]$ (i.e. $J = 1$), namely the identity function $w_0(t) = t$, $0 \le t \le L_0$. Interestingly, in this special case, the functions w_j and w_{-j} are symmetric about the diagonal (Fig. 6.4):

$$w_j(t) = w_{-j}^{-1}(t), \qquad 0 \le t \le t_j^{\text{end}}, \quad j = 1, \ldots, K, \quad (6.21)$$

where $t_j^{\text{end}} = w_{-j}(L_0)$. In this case, note that $K = I = \lfloor \eta_1 \rfloor$.

6.3.2   Piece-wise Continuous Re-warping Functions

If $\mathbf{g}_1$ spans at least one cycle, i.e. $\eta_1 \ge 1$ (which is guaranteed when $L_1 \ge T_{\max}$), then there exists at least one *piece-wise continuous* re-warping function $w_{(0)}$ that satisfies Eq. (6.12) for all $t \in [0, L_0]$. We define this and a family of related *piece-wise continuous* functions as:

$$w_{(j)}(t) \stackrel{\text{def}}{=} \begin{cases} \phi_1^{-1}\left(p_0(t) + jT\right), & \text{if } p_0(t) \ge p_1(0) \\ \phi_1^{-1}\left(p_0(t) + (j+1)T\right), & \text{otherwise,} \end{cases} \qquad (6.22)$$

for $j = 0, \ldots, \lfloor \eta_1 \rfloor - 1$. Each $w_{(j)}$ is monotonically increasing except when jump discontinuities occur at $t_{-1}^{\text{start}}, \ldots, t_{-I}^{\text{start}}$. Additionally, if the number of cycles in $\mathbf{g}_1$ is non-integer, i.e $\eta_1 \in [1, \infty) \setminus \{1, 2, \ldots\}$, there exists an extra piece-wise continuous re-warping function $w_{(\lfloor \eta_1 \rfloor)}(t)$ defined only for a disconnected set of sub-intervals of $t \in [0, L_0]$ that satisfy:

$$\phi_1\left(w_{(\lfloor \eta_1 \rfloor - 1)}(t)\right) < \phi_1(w_{(0)}(t)) + \lfloor \eta_1 \rfloor T \le \phi_1\left(L_1\right). \qquad (6.23)$$

The *continuous* solutions w_j defined in Eq. (6.14) can be constructed by combining the *piece-wise continuous* solutions $w_{(j)}$ in Eq. (6.22), as depicted in Fig. 6.2(b).
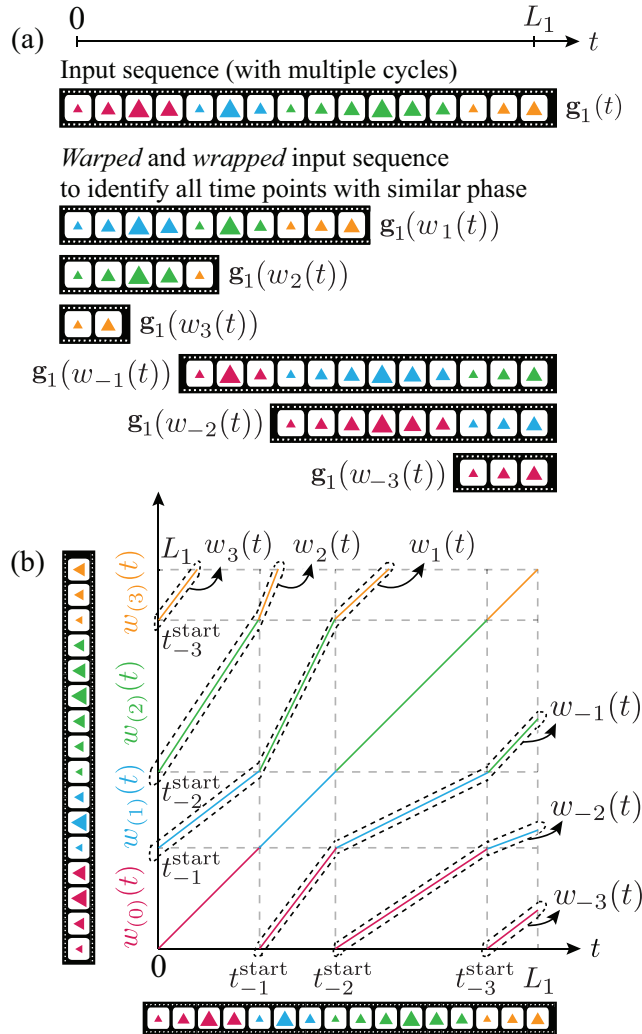
Figure 6.4: (a-b) When $\mathbf{g}_0 = \mathbf{g}_1$, there only exists one *continuous* and monotonically increasing re-warping function $w_0(t) = t$, valid for all $t \in [0, L_0]$. The other *continuous* warping functions w_j and w_{-j} have a symmetric nature about the identity function for $j = 1, \ldots, K$. The colors represent different cycles in the sequence.

If $\mathbf{g}_1$ spans exactly one cycle ($\eta_1 = 1$), then $w_{(0)}$ represents the unique *piece-wise continuous* and monotonically increasing solution that satisfies Eq. (6.12), as shown in Fig. 6.3(a-b). A summary of the notations introduced so far is summarized in Table 6.1.

113

Excessive
dilation and contraction
is generally penalized.

Discrete equivalent of
jump discontinuities are permitted
when necessary.

(a) For $w[n] \geq \Delta w_{\max}$ (b) For $w[n] < \Delta w_{\max}$
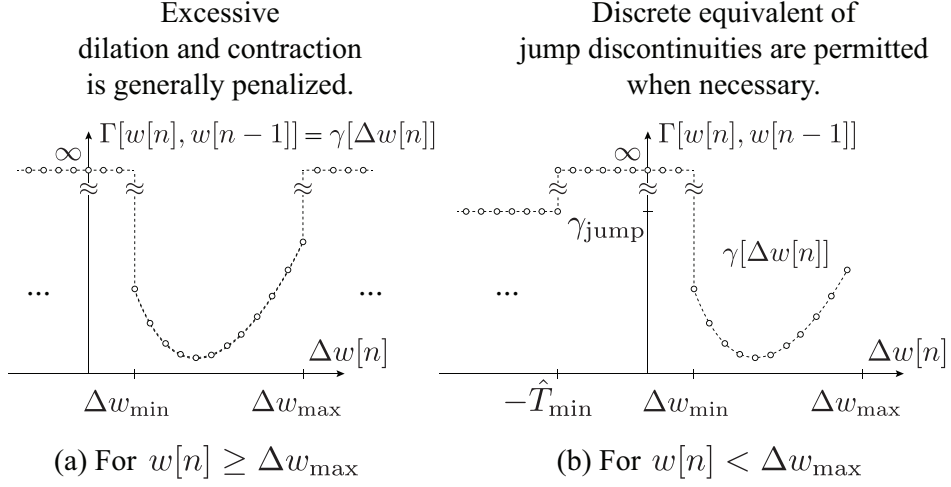
Figure 6.5: The regularization function used for QPDTW. The regularization function serves to penalize excessive dilation/contraction of the input sequence and to also allow jump discontinuities (from monotonicity) in the re-warping solution, when necessary.

6.4 Algorithms for Synchronizing, Re-binning, and Compounding Discrete-Time Sequences

We now present two discrete-time algorithms to (A) synchronize a pair of quasi-periodic sequences, and (B) identify all time points in a single quasi-periodic sequence with an equivalent phase by comparing the sequence to itself.

6.4.1 Discrete-time Re-warping for Sequence Synchronization

We consider two discrete-time sequences $\mathbf{g}_0[n]$ and $\mathbf{g}_1[n]$ that are obtained by sampling $\mathbf{g}_0(t)$ and $\mathbf{g}_1(t)$ in time as:

$$\mathbf{g}_k[n] \stackrel{\text{def}}{=} \mathbf{g}_k(n\Delta t), \quad 0 \leq n < N_k, \quad k = 0, 1, \tag{6.24}$$

Figure 6.6: An example of the discrete re-warping function $\tilde{w}$ returned by QPDTW for the quasi-periodic signals shown. Note that the maximum number of discontinuities in the estimated solution shown here is set as $\xi = 1$.

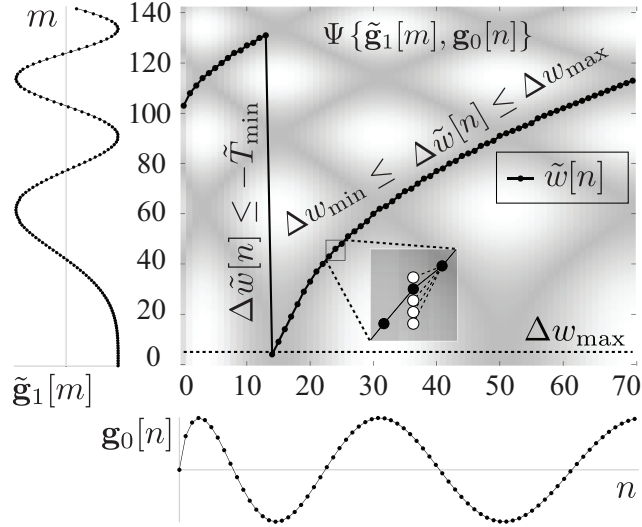where Δt refers to the temporal sampling step. We also consider $\tilde{\mathbf{g}}_1$, a temporally over-sampled version of $\mathbf{g}_1$ estimated via temporal interpolation:

$$\tilde{\mathbf{g}}_1[n] \approx \mathbf{g}_1(n\Delta t/\rho), \qquad 0 \leq n < \tilde{N}_1 \stackrel{\text{def}}{=} \rho(N_1 - 1) + 1, \quad (6.25)$$

where $\rho \in \mathbb{N}$ denotes the over-sampling factor. We then consider the problem of estimating a discrete-time re-warping function $\tilde{w} : \{0, \ldots, N_0 - 1\} \to \{0, \ldots, \tilde{N}_1 - 1\}$, a discrete equivalent of w in Eq. (6.12), such that $\tilde{\mathbf{g}}_1[\tilde{w}[n]]$ is synchronized to $\mathbf{g}_0[n]$, $0 \leq n < N_0$. We solve for $\tilde{w}$ by finding the global minimum to the following objective function:

$$\mathcal{O}\{w\} \stackrel{\text{def}}{=} \sum_{n=0}^{N_0-1} \Psi\left(\tilde{\mathbf{g}}_1[w[n]], \mathbf{g}_0[n]\right) + \lambda \sum_{i=1}^{N_0-1} \Gamma[w[i], w[i-1]], \qquad (6.26)$$

subject to the constraint that the number of jump discontinuities in w does not exceed a chosen value of ξ. This constraint provides the end-user with the additional flexibility to choose solutions that have limited number of discontinuities. However, if inconsequential

for an application, this number can be set to $\xi \to \infty$ with no significant repercussions, since, as we shall discuss shortly, we regularize the objective function to allow for discontinuities only when they are reasonable.

Here, the first term compares a temporally warped form of $\mathbf{g}_1$ (using a candidate discrete warping function $w[\cdot]$) with $\mathbf{g}_0$ and rewards similarity. The second term comprises a regularization function Γ whose influence is controlled by a non-negative scalar λ. The regularization term serves to (i) prevent the warping function from excessively distorting (contracting or dilating) the signal, and (ii) ensure the warping function is monotonically increasing except at a few time points (equivalent to t_j^{start}), that join partial solutions. We fulfill these requirements expected of the regularization in two steps.

To realize (i), we employ a polynomial function of the form:

$$\gamma\,[m] \stackrel{\text{def}}{=} \begin{cases} a\,|m - \rho|^b + c, & \Delta w_{\text{min}} \leq m \leq \Delta w_{\text{max}} \\ \infty, & \text{otherwise}, \end{cases} \tag{6.27}$$

where $a, b, c \geq 0$ are three constants (empirically set to $a = b = c = 1$), and $\Delta w_{\text{min}} = \lfloor \rho \cdot T_{\text{min}}/T_{\text{max}} \rfloor$ and $\Delta w_{\text{max}} = \lceil \rho \cdot T_{\text{max}}/T_{\text{min}} \rceil$ are the minimum and maximum possible values for the finite difference $\Delta w[n] = w[n] - w[n-1]$, $n = 1, \ldots, N_0 - 1$. The function γ penalizes slopes that differ from identity (after taking into account the over-sampling factor ρ) and forbids slopes gentler than Δw_{min} (excessive dilation) or steeper than Δw_{max} (excessive contraction), as shown in Fig. 6.5(a).

Though the concept of jump discontinuities for re-warping functions no longer applies in a discrete setting, the requirement represented in (ii) for the regularization term is essential since it relaxes the strict requirement on the slope given in Eq. (6.27) and allows for the discrete equivalent of jump discontinuities (finite differences outside the bounds of Δw_{min} and Δw_{max}) found in *piece-wise continuous* re-warping functions. We

116

achieve this by assigning a fixed cost γ_{jump} to the finite difference $\Delta w[n]$ when:

$$0 \leq w[n] < \Delta w_{\text{max}}, \qquad\qquad 1 \leq n < N_0, \quad (6.28)$$

and require that the discontinuities, when they occur, be of a minimum amount $\tilde{T}_{\text{min}}$ [see Fig. 6.5(b)]:

$$w[n-1] \geq w[n] + \tilde{T}_{\text{min}}, \qquad\qquad 1 \leq n < N_0, \quad (6.29)$$

where $\tilde{T}_{\text{min}} = T_{\text{min}} \cdot \rho / \Delta t$ represents the discrete equivalent of T_{min}. Similarly, we will use $\tilde{T}_{\text{max}} = T_{\text{max}} \cdot \rho / \Delta t$ to denote the discrete equivalent of T_{max}.

We finally define the function Γ used in Eq. (6.26) as:

$$\Gamma\left[w[n], w[n-1]\right] \overset{\text{def}}{=} \begin{cases} \gamma_{\text{jump}}, & \text{if Eqs. (6.28) and (6.29) hold} \\ \gamma\left[\Delta w[n]\right], & \text{otherwise.} \end{cases} \qquad (6.30)$$

When the similarity and regularization terms are normalized to unity, setting $\lambda \geq 0.5$ is a typical choice when the sequences are nearly periodic in nature. On the other hand, if there is significant quasi-periodicity in the sequences, we set $0 < \lambda < 0.5$ to avoid excessive penalization of the dilation and contraction necessary in the temporal warping function. As long as the values of λ are varied within these limits, there is no notable effect on the results estimated. Furthermore, in order to allow for jump discontinuities (only when necessary) in an otherwise monotonically increasing temporal re-warping function, we assign $\gamma_{\text{jump}} = \max(\gamma(\Delta w_{\text{min}}), \gamma(\Delta w_{\text{max}}))$ in our model. Albeit, assigning $0 < \gamma_{\text{jump}} \leq \max(\gamma(\Delta w_{\text{min}}), \gamma(\Delta w_{\text{max}}))$ does not significantly affect the accuracy of the re-warping functions estimated owing to the conditional safeguards placed by Eqs. (6.28) and (6.29) in the regularization function defined in Eq. (6.30).

We minimize the objective function in Eq. (6.26) by using a dynamic programming framework since it conforms to a Hidden Markov Model (see Appendix 6.A.1). Our approach will be similar to the DTW technique [76]. Since it extends it by accounting for quasi-periodicity and phase wrappings (that account for select discontinuities), we refer to our method as quasi-periodic dynamic time warping (QPDTW). We start by forming a cumulative cost matrix $\mathcal{C}$ defined as:

$$\mathcal{C}[m,0] \stackrel{\text{def}}{=} \Psi\left(\tilde{\mathbf{g}}_1[m], \mathbf{g}_0[0]\right), \tag{6.31}$$

$$\mathcal{C}[m,n] \stackrel{\text{def}}{=} \mathcal{C}[\mathcal{I}[m,n], n-1] + \Psi\left(\tilde{\mathbf{g}}_1[m], \mathbf{g}_0[n]\right) + \lambda \cdot \Gamma[m, \mathcal{I}[m,n]] \cdot \mathcal{M}[m, \mathcal{I}[m,n], n-1], \tag{6.32}$$

where $\mathcal{I}[m,n]$ is a matrix entry that records the best index in the preceding column $n-1$ defined as:

$$\mathcal{I}[m,n] \stackrel{\text{def}}{=} \arg\min_i \mathcal{C}[i, n-1] + \lambda \cdot \Gamma[m,i] \cdot \mathcal{M}[m,i,n-1], \tag{6.33}$$

for $m = 0, \ldots, \tilde{N}_1 - 1$, and $n = 1, \ldots, N_0 - 1$. Here, $\mathcal{M}$ is a mask matrix that ensures the number of discrete discontinuities in the solution does not exceed ξ and is defined as:

$$\mathcal{M}[m,i,n] = \begin{cases} \infty, & \text{if } \mathcal{D}[i,n] > \xi \\ 1, & \text{otherwise,} \end{cases} \tag{6.34}$$

for $i, m = 0, \ldots, \tilde{N}_1 - 1$, and $n = 0, \ldots, N_0 - 1$. The number of discontinuities in the path found by back-propagating from the reference time index $0 \leq n < N_0$ and the

interpolated time index $0 \leq i < \tilde{N}_1$ is entered in the matrix $\mathcal{D}$ cumulatively as:

$$\mathcal{D}[i, n] \stackrel{\text{def}}{=} \begin{cases} 0, & \text{if } n = 0 \\ \mathcal{D}[\mathcal{I}[i, n], n - 1], & \text{if } \Delta w_{\min} \leq i - \mathcal{I}[i, n] \leq \Delta w_{\max} \\ \mathcal{D}[\mathcal{I}[i, n], n - 1] + 1, & \text{otherwise}, \end{cases} \tag{6.35}$$

for $i = 0, \ldots, \tilde{N}_1 - 1$, and $n = 0, \ldots, N_0 - 1$. The optimal function $\tilde{w}$ can be traced back as in the Viterbi algorithm [82]:

$$\tilde{w}[n] = \mathcal{I}[\tilde{w}[n + 1], n + 1], \tag{6.36}$$

for $n = N_0 - 2, \ldots, 1, 0$ with the initial condition:

$$\tilde{w}[N_0 - 1] = \arg \min_{i \in \{0, \ldots, \tilde{N}_1 - 1\}} \mathcal{C}\left[i, N_0 - 1\right]. \tag{6.37}$$

The solution $\tilde{w}$ estimated with QPDTW is a discrete approximation with sections that coincide with the discrete equivalent of re-warping functions w_j and $w_{(j)}$ defined in Eqs. (6.14) and (6.22), respectively, with discontinuities (if any) only occurring at time points where $w_{(0)}$ has discontinuities, as illustrated in the example shown in Fig. 6.6, where the maximum number of discontinuities (from monotonicity) is chosen as $\xi = 1$.

6.4.2   Intra-sequence Processing

We now adapt our QPDTW framework to estimate intermediary time points of a single quasi-periodic sequence by using other cycles in the same sequence—an approach we term self-QPDTW. Since only one sequence is involved, we drop the subscripts for brevity, i.e. $\mathbf{g} = \mathbf{g}_1$ and $N = N_1$.

We aim to find discrete-time warping functions that act as discrete estimates of w_j, which we denote as $\tilde{w}_j$, for $j = -1, -2, \ldots, -I$ defined in the range $\tilde{n}_j^{\text{start}} \leq n < \tilde{N}$, and for $j = 1, 2, \ldots, I$, defined in the range $0 \leq n \leq \tilde{n}_j^{\text{end}}$. Starting with $\tilde{w}_0[n] = n$, $0 \leq n < \tilde{N}$, we proceed to determine the I sequences $\tilde{w}_j$ recursively, $j = -1, -2, \ldots, -I$, by repeatedly minimizing the objective function:

$$\mathcal{O}\{w\} \overset{\text{def}}{=} \sum_{n=0}^{\tilde{N}-1} \Psi\left(\tilde{\mathbf{g}}[w[n]], \tilde{\mathbf{g}}[n]\right) + \lambda \sum_{i=1}^{\tilde{N}-1} \Gamma\left[w[i], w[i-1]\right], \tag{6.38}$$

subject to the following constraints:

$$\tilde{T}_{\min} \leq |n - w[n]| < \tilde{N} \tag{6.39}$$

$$\tilde{T}_{\min} \leq \tilde{w}_{j+1}[\tilde{N}-1] - \tilde{w}_j[\tilde{N}-1] \leq \tilde{T}_{\max}. \tag{6.40}$$

Given the function $\bar{w}[n]$ that minimizes the criterion $\mathcal{O}$ with conditions given in Eqs. (6.39) and (6.40), for $n = 0, \ldots, \tilde{N}-1$, we define $\tilde{w}_j[n]$ as the last jump-free sub-sequence:

$$\tilde{w}_j[n] \overset{\text{def}}{=} \begin{cases} \bar{w}[n], & \tilde{n}_j^{\text{start}} \leq n < \tilde{N} \\ \text{undefined}, & \text{otherwise}, \end{cases} \tag{6.41}$$

where we define $\tilde{n}_j^{\text{start}}$, the discrete equivalent of t_j^{start}, as the minimum time index n such that:

$$\Delta w_{\min} \leq \tilde{w}[n+1] - \tilde{w}[n] \leq \Delta w_{\max}. \tag{6.42}$$

Since the objective function for self-QPDTW in Eq. (6.38) is similar to that for QPDTW in Eq. (6.26), by substituting $\mathbf{g}_0 = \tilde{\mathbf{g}}$ and $\mathbf{g}_1 = \mathbf{g}$, we minimize it using the same dynamic programming framework as described in the previous subsection. However, in order to account for the constraints placed for self-QPDTW in Eqs. (6.39) and (6.40), we redefine

the mask matrix $\mathcal{M}$ used in Eq. (6.34) as:

$$\mathcal{M}[m, i, n] = \begin{cases} 1, & \tilde{T}_{\min} \leq |m - n| < \tilde{N} \\ \infty, & \text{otherwise,} \end{cases} \tag{6.43}$$

for $0 \leq m, n < \tilde{N}$. We then recursively find the I local minima and trace back using the Viterbi algorithm [82] as:

$$\tilde{w}_j[\tilde{N} - 1] = \arg \min_{\tilde{w}_{j+1}[\tilde{N}-1] - \tilde{T}_{\max} \leq i \leq \tilde{w}_{j+1}[\tilde{N}-1] - \tilde{T}_{\min}} \mathcal{C}[i, \tilde{N} - 1], \tag{6.44}$$

$$\tilde{w}_j[n] = \mathcal{I}[\tilde{w}_j[n + 1], n + 1], \tag{6.45}$$

for $j = -1, -2, \ldots, -I$ and for $n = \tilde{N} - 2, \ldots, \tilde{n}_j^{\text{start}}$. Recalling Eq. (6.21), we estimate the discrete equivalent of $w_j(t) = w_{-j}^{-1}(t)$, $j = 1, \ldots, I$, as:

$$\tilde{w}_j\left[\tilde{n}_j^{\text{end}}\right] = \tilde{N} - 1, \tag{6.46}$$

$$\tilde{w}_j[n] = \mathcal{I}[\tilde{w}_j[n + 1], n + 1], \tag{6.47}$$

where $\tilde{n}_j^{\text{end}} = \tilde{w}_{-j}[\tilde{N} - 1]$ and $n = \tilde{n}_j^{\text{end}} - 1, \ldots, 0$.

We denote $\mathcal{S}_n^- = \{\tilde{w}_{-1}[n], \ldots, \tilde{w}_j[n], \ldots, \tilde{w}_{-I}[n] \,|\, \tilde{n}_j^{\text{start}} \leq n < \tilde{N}\}$, as the set of all time indices anterior to n that have an equivalent phase as n [see Fig. 6.9(a-b)]. Similarly, we denote $\mathcal{S}_n^+ = \{\tilde{w}_1[n], \ldots, \tilde{w}_j[n], \ldots, \tilde{w}_I[n] \,|\, 0 \leq n \leq \tilde{n}_j^{\text{end}}\}$, as the set of all time indices posterior to n that have an equivalent phase as n [see Fig. 6.9(a-b)]. Finally, we denote $S_n = S_n^- \cup S_n^+$ as the collection of all time indices that have an equivalent phase as n.
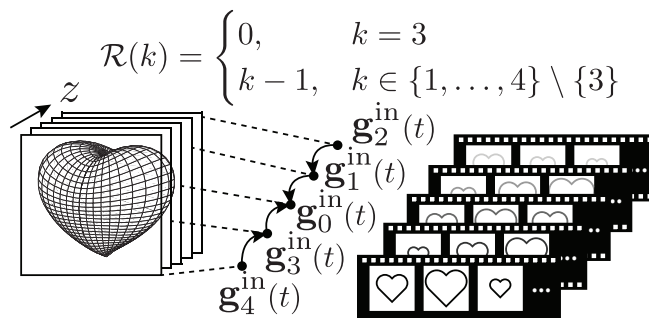
$$\mathcal{R}(k) = \begin{cases} 0, & k = 3 \\ k - 1, & k \in \{1, \dots, 4\} \setminus \{3\} \end{cases}$$

Figure 6.7: For each sequence $\mathbf{g}_k^{\mathrm{in}}$, the reference index $\mathcal{R}(k) \in \{0, \dots, k - 1\}$ defines which sequence (that has already been synchronized) acts as its intermediary reference.

6.5   Applications in Cardiac Imaging

In this section, we describe how the algorithms described in Section 6.4 can be used for applications in cardiac imaging.

6.5.1   Synchronization of Multi-dimensional Cardiac Sequences

When using QPDTW for the temporal synchronization of multi-dimensional cardiac sequences, multiple quasi-periodic sequences $\mathbf{g}_k^{\mathrm{in}}$, $k = 0, \dots, M - 1$, are involved, where they may each represent measurements at a different axial location, imaging modality, or age. All these sequences need to be mutually synchronized before they can be meaningfully visualized. For each input sequence $\mathbf{g}_k^{\mathrm{in}}$, $k = 1, \dots, M - 1$, a reference index, $\mathcal{R}(k) \in \{0, \dots, k - 1\}$, can be chosen according to the manner in which the synchronization is to be performed. For instance, if every sequence $\mathbf{g}_k^{\mathrm{in}}$ is to be compared with a common reference $\mathbf{g}_0^{\mathrm{in}}$, then $\mathcal{R}(k) = 0$, for $k = 1, \dots, M - 1$ (such a geometry would apply to the method described in [59]). Alternatively, given a set of parallel sections acquired sequentially at different axial positions, each sequence can be synchronized to its neighbor, starting from the center and proceeding recursively towards both ends [64]. On numbering the sequences following the example shown in Fig. 6.7, the reference index

sequence would then be $\mathcal{R}(k) = k - 1$, for $k \in \{1, \ldots, M - 1\} \setminus \{\lceil M/2 \rceil\}$ and $\mathcal{R}(k) = 0$, for $k = \lceil M/2 \rceil$. The general registration algorithm is described below.

Algorithm 6.1 Sequential synchronization of multiple sequences

---

1: For each sequence index $k = 1, \ldots, M - 1$, designate a reference index $\mathcal{R}(k) \in \{0, \ldots, k - 1\}$.
2: $\mathbf{g}_0^{\text{out}} \leftarrow \mathbf{g}_0^{\text{in}}$.
3: **for** $k \leftarrow 1$ **to** $M - 1$ **do**
4:     $\mathbf{g}_1 \leftarrow \mathbf{g}_k^{\text{in}}$.
5:     $\mathbf{g}_0 \leftarrow \mathbf{g}_{\mathcal{R}(k)}^{\text{out}}$.
6:     Given $\mathbf{g}_0$ and $\mathbf{g}_1$, use QPDTW to find $\tilde{w}$.
7:     $\tilde{w}_k^{\text{out}} \leftarrow \tilde{w}$.
8:     $\mathbf{g}_k^{\text{out}}[n] \leftarrow \tilde{\mathbf{g}}_k[\tilde{w}_k^{\text{out}}[n]], \quad 0 \leq n < N_0$.
9: **end for**

6.5.2   Temporal Over-sampling using Multiple Cycles

Self-QPDTW can be used to temporally rearrange frames belonging to multiple cycles in a quasi-periodic cardiac sequence to yield an output sequence with higher frame-rate, as illustrated in Fig. 6.8. This is in contrast with techniques that assume perfect periodicity and attempt to estimate the time-period of the cycles to subsequently rearrange and re-sample the sequence with a higher frame-rate [35, 66]. Specifically, given a quasi-periodic sequence $\mathbf{g}$, the self-QPDTW technique can be used to find multiple warping functions $\tilde{w}_j$, $j = \pm 1, \pm 2, \ldots, \pm I$. Using this information, the best estimate of the intermediary frame at n, denoted as $\mathring{w}[n]$, can be found among all the warping functions returned by self-QPDTW as:

$$\mathring{w}[n] \overset{\text{def}}{=} \arg\min_{i \in S_n} \Psi\left(\mathbf{g}\left[\text{round}\left(i/\rho\right)\right], \tilde{\mathbf{g}}[n]\right), \qquad 0 \leq n < \tilde{N}, \quad (6.48)$$

Figure 6.8: (a-b) The multiple warping functions found using self-QPDTW for a sequence, $\mathbf{g}$, with $\eta = 7.5$ cycles, $T = 10.125$, $\Delta t = 1$, $\alpha_{\min} = 0.65$, $\alpha_{\max} = 1.35$, and $\rho = 2$, overlaid with $\mathring{w}[n]$ shown as red dots for each n. (c) The time points in $\mathbf{g}$ are rearranged to yield (d) $\mathring{\mathbf{g}}$ with the frame-rate increased by $\rho = 2$. The orange dots in (d) represent the new time-points added as a result of temporal rearrangement.

and the temporally rearranged sequence can be estimated as:

$$\mathring{\mathbf{g}}[n] \stackrel{\text{def}}{=} \mathbf{g}\left[\text{round}\left(\mathring{w}[n]/\rho\right)\right], \qquad\qquad 0 \leq n < \tilde{N}. \quad (6.49)$$

6.5.3 Multi-cycle Noise Reduction

The self-QPDTW framework can be used to find all frames with the same cardiac phase as any given frame in the sequence. Given such a set of same-phase frames, techniques ranging from pixel-wise median filtering [9] to non-local-means [4] can be used to reduce noise. Our algorithm relieves limitations of past algorithms that require pre-cutting the sequence into multiple pieces [9] and that are limited to noise removal on a subset of the entire sequence.

Considering the example of point-wise averaging for noise reduction, the denoised output can be estimated as:

$$\bar{\mathbf{g}}[n] \stackrel{\text{def}}{=} \frac{1}{\text{card}\left(S_{n\rho}\right)+1}\left(\mathbf{g}[n] + \sum_{i \in S_{n\rho}} \mathbf{g}\left[\text{round}\left(i/\rho\right)\right]\right), \qquad\qquad (6.50)$$

for $0 \leq n < N$, where $\text{card}(S)$ denotes the number of frames in the set S. This is illustrated in Fig. 6.9 using a noisy quasi-periodic sinusoidal signal.
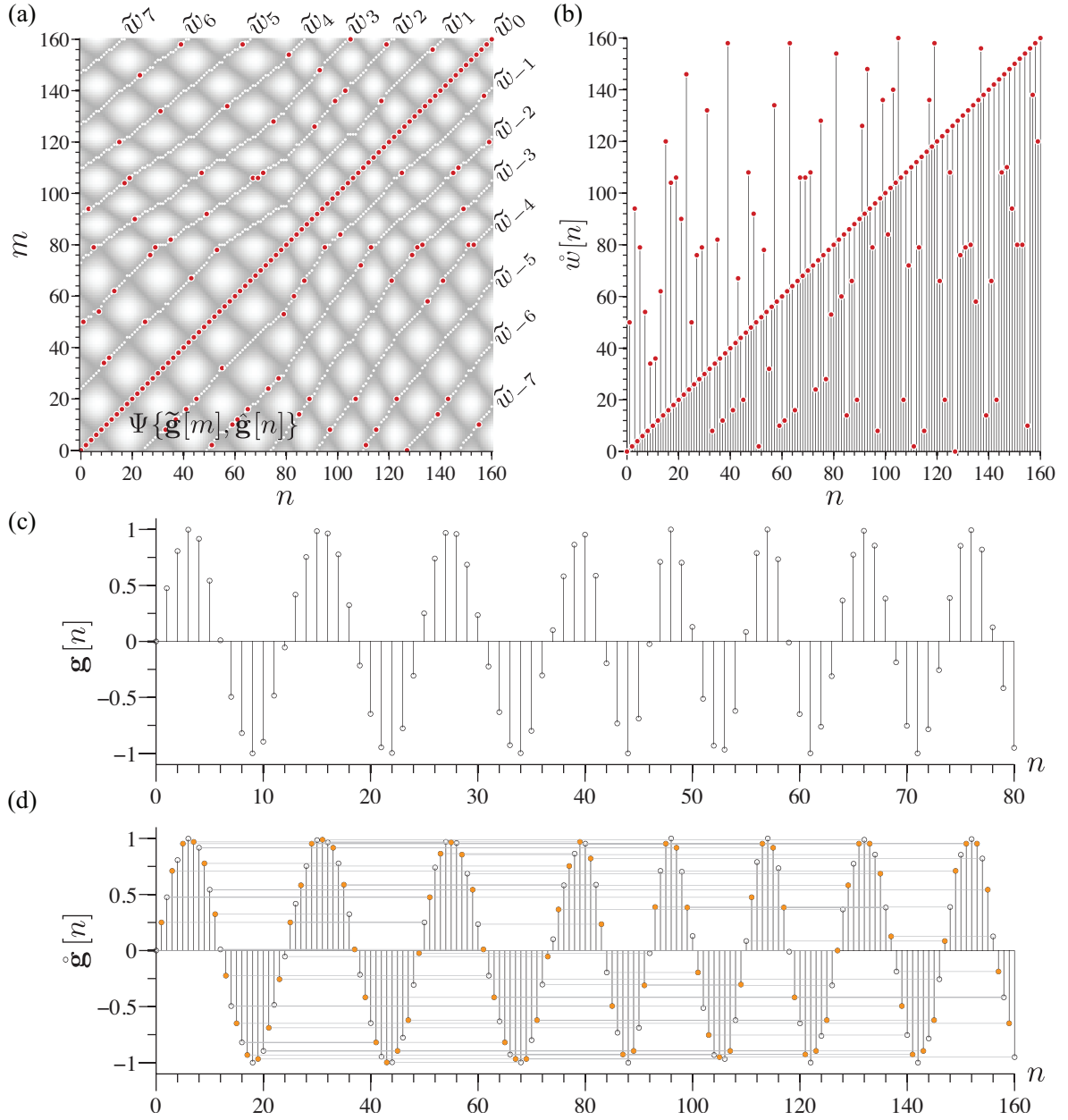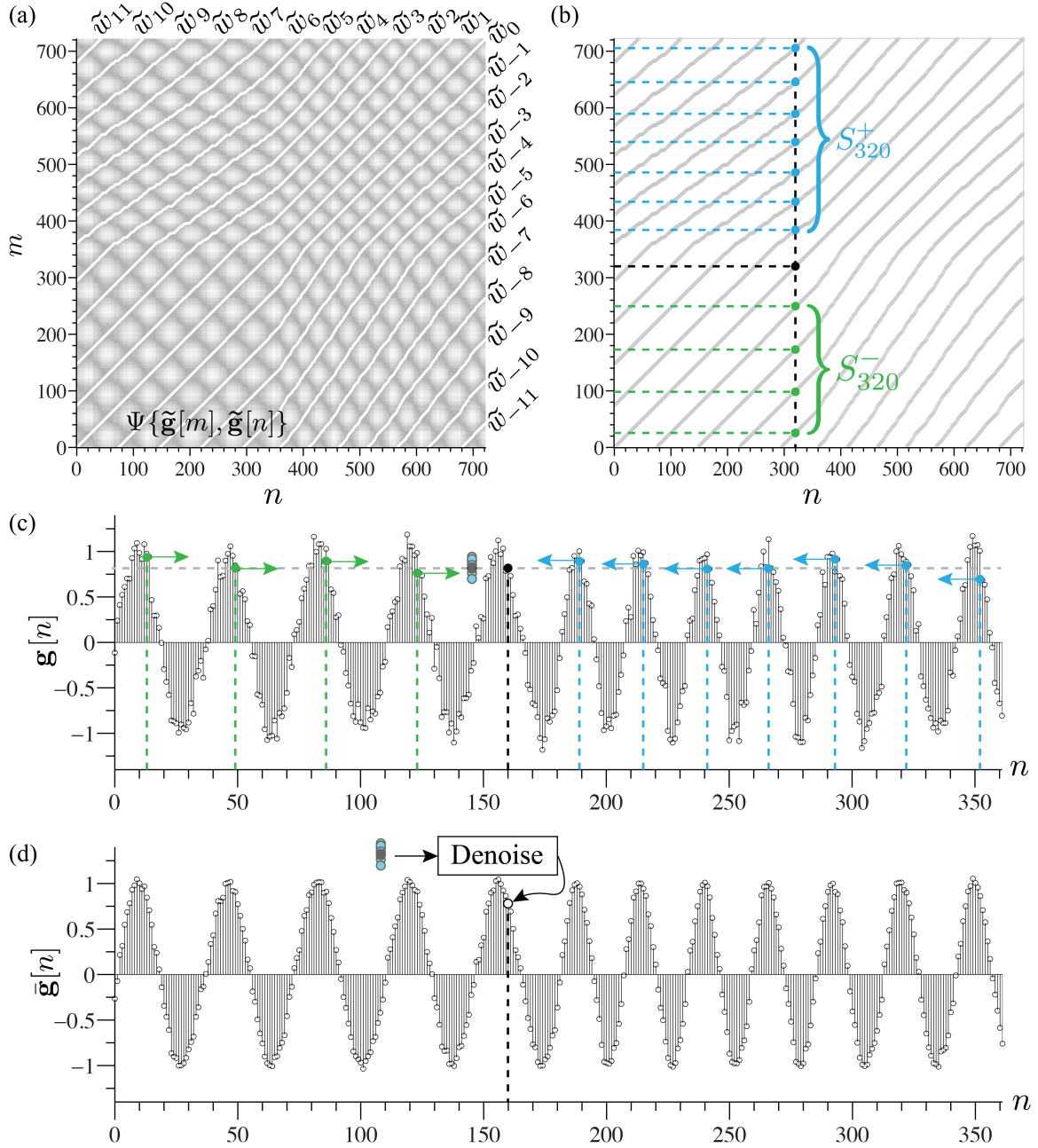
Figure 6.9: (a-b) The multiple warping functions found using self-QPDTW for a sequence, $\mathbf{g}$, with $\eta = 12.5$ cycles, $T = 30.125$, $\Delta t = 1$, $\alpha_{\min} = 0.65$, $\alpha_{\max} = 1.35$, and $\rho = 2$. The set $S = S_n^- \cup S_n^+$ consist of all time points that have an equivalent phase as n. (c) The time points with an equivalent phase in the noisy input sequence $\mathbf{g}$ can be used with a suitable denoising algorithm to yield (d) $\bar{\mathbf{g}}$. Point-wise averaging is the denoising algorithm used for the results shown in (d).

126

6.6 Validation

6.6.1 Performance Evaluation on Simulated Datasets

6.6.1.1 Sinusoidal Signals $(0D + \text{time})$

We first evaluated the performance of QPDTW using two quasi-periodic sinusoidal signals defined as:

$$\mathbf{g}_k[n] \stackrel{\text{def}}{=} \sin\left(\frac{2\pi}{T}\phi_k(n\Delta t)\right), \qquad 0 \leq n < N_k, \quad k = 0, 1, \quad (6.51)$$

where ϕ_k is modeled with linear B-splines [108] β^1 as:

$$\phi_k(t) \stackrel{\text{def}}{=} \sum_{m=0}^{N_k-1} \phi_k[m] \cdot \beta^1\left(\frac{t}{\Delta t} - m\right). \qquad (6.52)$$

We chose the coefficients defining the phase function ϕ_k as:

$$\phi_k[n] \stackrel{\text{def}}{=} \begin{cases} 0, & k = n = 0 \\ \phi \sim \mathcal{U}(0, T), & n = 0 \\ \phi_k[n-1] + \phi', & 1 \leq n < N_k, \end{cases} \qquad (6.53)$$

where $\phi' \sim \mathcal{U}\left(\alpha_{\min}\Delta t, \alpha_{\max}\Delta t\right)$ and $\mathcal{U}(a, b)$ denotes a uniform distribution between a and b. For clarity, we assigned $\alpha_{\min} = 1/(1 + \delta)$ and $\alpha_{\max} = 1/(1 - \delta)$, where $0 \leq \delta \leq 0.5$, so that $T_{\min} = (1 - \delta)T$ and $T_{\max} = (1 + \delta)T$. We then varied the values of δ and Δt, and estimated the discrete warping function $\tilde{w}$ using the following three techniques: (a) string length method (SLM) [96] to estimate the period of the sequence and cross-correlation to find the best time-shift for temporal alignment [64, 35, 66], (b) our previously proposed form of DTW [65], and (c) our proposed method, QPDTW. For a fair comparison, the
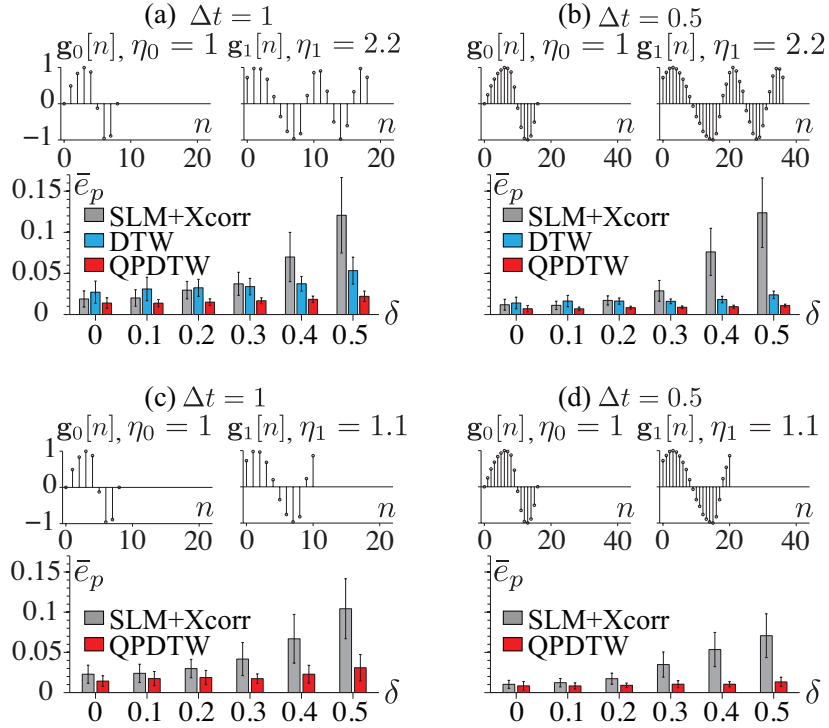
Figure 6.10: (a-d) The experimental phase errors $\bar{e}_p$ calculated for sinusoidal signals with varying levels of quasi-periodicity (δ), sampling step (Δt), and number of cycles (η_0 and η_1), are consistently lowest with QPDTW. Since $\eta_1 < \eta_0 + 1$ in (c-d), conventional DTW (not shown) is inapplicable.

sequences were interpolated using the same over-sampling factor ρ in each method. We evaluated the performance of each algorithm by calculating the phase error as:

$$\bar{e}_p \stackrel{\text{def}}{=} \frac{1}{TN_0} \sum_{n=0}^{N_0-1} \min_{s \in \{0,1\}} sT + (-1)^s \left| p_1 \left(\tilde{w}[n] \frac{\Delta t}{\rho} \right) - p_0 \left(n \Delta t \right) \right|. \tag{6.54}$$

We first considered the case where temporal wrapping is not necessary by setting $\eta_0 = 1$ and $\eta_1 = 2.2$. Using parameters $T = 10.2$ and $\Delta t = 1$, the root-mean-square (RMS) and standard deviation values of the phase error $\bar{e}_p$ observed over 100 different instances are shown in Fig. 6.10(a). The first technique, which involves using SLM and cross-correlation is, by design, unable to apply any non-uniform warping function other than a linear function for synchronization. Therefore, as expected, it was only reliable

when the two sequences differed by a pure phase-offset ($\delta = 0$), and its performance deteriorated rapidly for higher values of δ. On the other hand, our previously proposed DTW performed reasonably well for high values of δ, but failed to the first approach for relatively low values of δ. This can be attributed to a design flaw in the DTW technique proposed in [65] that involves two steps of interpolation, thereby causing the errors incurred during interpolation to accrue. This problem is mitigated in QPDTW, which uses only a single step of interpolation for synchronization. Our algorithm thus yielded lower phase errors for all values of δ considered. The performance of all the three algorithms improved when the temporal sampling rate was increased using $\Delta t = 0.5$, as shown in Fig. 6.10(b). We next considered the case where temporal wrapping was necessary by choosing $\eta_0 = 1$ and $\eta_1 = 1.1$, and repeated the same set of experiments using the only two compliant methods: (a) SLM + cross-correlation, and (b) QPDTW, yielding the results shown in Fig. 6.10(c) and (d). The consistently low errors obtained with QPDTW confirm the latter's effectiveness even when temporal wrapping is necessary for alignment.

6.6.1.2   B-spline Based Quasi-Periodic Heart Phantom (3D + time)

We next considered a simplified B-spline based periodically deforming model of the heart (see Appendix 6.A.2) to validate the QPDTW recursive volume registration described in subsection 6.5.1. Using phase functions similar to Eqs. (6.52) and (6.53), we generated $2D$ + time quasi-periodic sequences $\mathbf{g}_k^{\text{in}}$, $k = 0, \dots, M - 1$, corresponding to $M = 25$ different axial locations of the heart model. Specifically, we treated the sequence at the center axial location as $\mathbf{g}_0^{\text{in}}$, and proceeded in both axial directions to recursively synchronize each slice $\mathbf{g}_k^{\text{in}}$, $k = 1, \dots, M-1$ to its reference $\mathbf{g}_{\mathcal{R}(k)}^{\text{out}}$, where $\mathcal{R}(k) = k-1$, for $k \in \{1, \dots, M - 1\} \setminus \{\lceil M/2 \rceil\}$ and $\mathcal{R}(k) = 0$, for $k = \lceil M/2 \rceil$, as illustrated in Fig. 6.11.

As in the previous experiments, we evaluated the performance of the algorithms when

All z-slices are recursively synchronized, starting from the center z-slice ($k = 0$)

$$\mathcal{R}(k) = \begin{cases} 0, & k = 13 \\ k - 1, & k \in \{1, \ldots, 24\} \setminus \{13\} \end{cases}$$

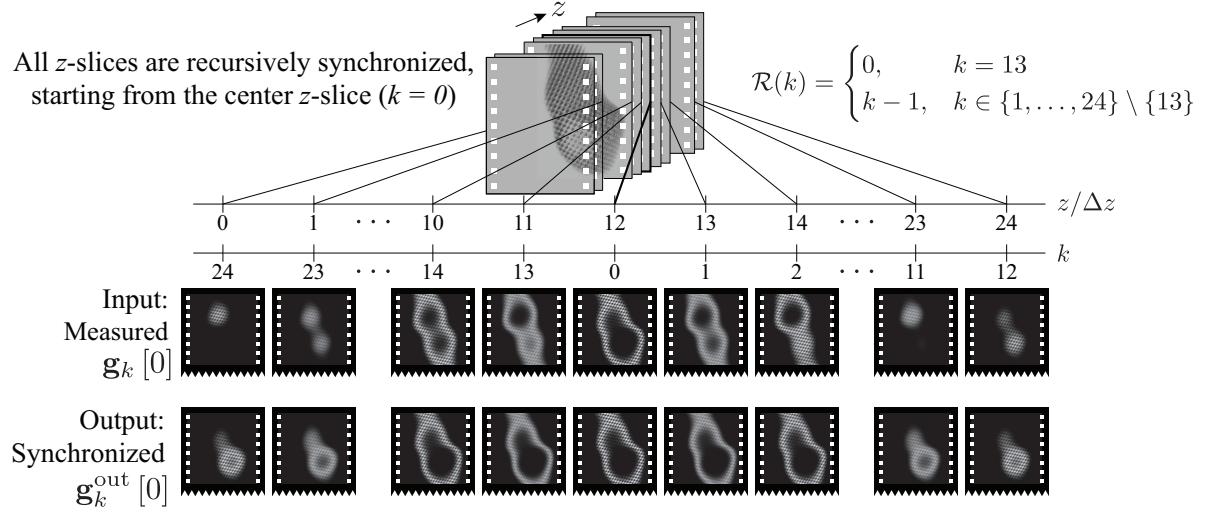Figure 6.11: Quasi-periodic sequences $\mathbf{g}_k^{\text{in}}$, $k = 0, \ldots, 24$, correspond to unsynchronized measurements at different axial locations of the heart phantom.
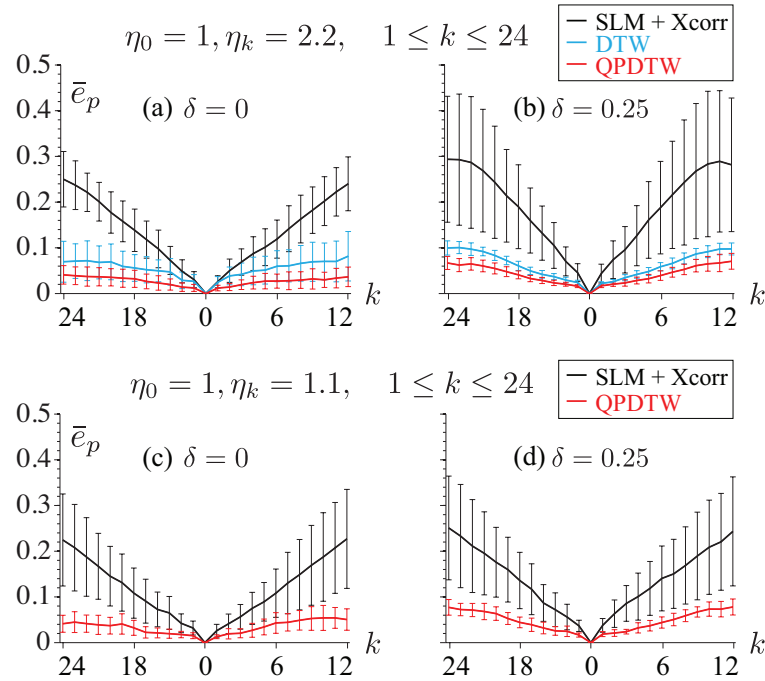

Figure 6.12: Following recursive synchronization beginning from the center for the data shown in Fig. 6.11, the phase error $\bar{e}_p$ tends to accrue towards both ends. For all cases considered, the error accumulation is least with QPDTW.

strictly monotonically increasing re-warping solutions existed, using $\eta_0 = 1, \eta_k = 2.2$, as well as when temporal wrapping was necessary, using $\eta_0 = 1, \eta_k = 1.1$, for $k = 1, \ldots, M - 1$. Furthermore, in order to test robustness against quasi-periodicity, we ran experiments for both $\delta = 0$ and $\delta = 0.25$, where $\alpha_{\min} = 1/(1+\delta)$ and $\alpha_{\max} = 1/(1-\delta)$, as in the previous experiment. The RMS and standard deviation values of the phase error $\bar{e}_p$ [see Eq. (6.54)] calculated for each of the $M = 25$ sequences over 25 different instances of this experiment are shown in Figs. 6.12(a-d). Since we followed a recursive order of synchronization, the errors made during synchronization accrued as we proceeded from the center towards the sequences at both the first and last axial position. As evident in Figs. 6.12(a-d), the errors accrued using QPDTW were lowest for all cases considered, corroborating its relatively higher robustness against error accumulation.

Note that the errors made during synchronization do not accumulate if all input sequences $\mathbf{g}_k^{\text{in}}$ are compared to a common reference $\mathbf{g}_0^{\text{in}}$ by choosing the reference indices as $\mathcal{R}(k) = 0$, for $k = 1, \ldots, M - 1$. However, in problems such as the synchronization of sequences acquired at multiple focal positions, a common reference that is comparable to all input sequences does not exist. Therefore, this requires a recursive synchronization procedure, as followed in the experiment here, relying on the assumption that the sequences at adjacent focal positions are sufficiently comparable.

We then proceeded to evaluate the performance of the temporal re-binning algorithm using multiple cycles of the single quasi-periodic sequence $\mathbf{g}_0$. We varied the number of frames available for each cycle $(T/\Delta t)$, the number of cycles (η_0), the amount of quasi-periodicity (δ), and increased the frame-rate of the sequence by a factor of ρ. We estimated the intermediary frames by solving for $\mathring{w}$ in Eq. (6.48) and evaluated performance by calculating the ratio of the phase errors after and before temporal re-

binning as:

$$
\mathring{e}_p \overset{\text{def}}{=} \frac{\displaystyle\sum_{m=0}^{\tilde{N}-1} \min_{s\in\{0,1\}} sT + (-1)^s \left| p\left(\mathring{w}[m]\frac{\Delta t}{\rho}\right) - p\left(m\frac{\Delta t}{\rho}\right)\right|}{\displaystyle\sum_{n=0}^{\tilde{N}-1} \min_{s\in\{0,1\}} sT + (-1)^s \left| p\left(\text{round}\left(n\frac{\Delta t}{\rho}\right)\right) - p\left(n\frac{\Delta t}{\rho}\right)\right|}. \tag{6.55}
$$

The value of this ratio averaged over 50 different experiments is shown in Table 6.2. The ratio of the phase errors was found to decrease with an increase in the number of cycles η_0, frames per cycle $(T/\Delta t)$, and with a decrease in the factor of temporal re-binning (ρ). This follows from the observation that with higher number of cycles and frames per cycle, there are more frames available that potentially have an intermediate phase and can hence be used favorably for temporal re-binning. Also, lower values of ρ lead to more accurate estimates of intermediate phases and higher probability for a frame with an equivalent phase to exist in a different cycle in the sequence.

6.6.2   Performance Evaluation on In Vivo Acquired Datasets

For evaluating our algorithm in practice, we used a wide-field microscope (Leica DMI 6000B) to collect movies of the beating heart in transgenic zebrafish larvae (see Table 6.3), wherein cardiac tissues produce fluorescent proteins [Fig. 6.13(a)-(j)].

For each fish sample, we sequentially collected movies at $Z > 1$ different axial locations. Note that since the movies at the different focal depths were collected serially, they each depict different cardiac cycles. Moreover, since these movies were acquired at arbitrary times, the movies were not mutually synchronized. To match our notation, we denote these movie frames as P-dimensional vectors $\mathbf{I}_k[n] \in \mathbb{R}^P$, $0 \leq n < N$, $0 \leq k < Z$, where P is the total number of pixels in each frame and N is the number of frames.

Since the ground-truth phase functions of these experimentally-acquired sequences

Table 6.2: The ratio of the phase errors $\mathring{e}_p$ for different experimental parameters in the temporal re-binning experiment.

δ	η_0	ρ	Frames per cycle $(T/\Delta t)$		
			10.2	20.2	30.2
0	4	2	0.3333	0.2533	0.2533
		4	0.3867	0.3133	0.2956
		8	0.4639	0.3655	0.3647
	8	2	0.3333	0.2530	0.2356
		4	0.4067	0.2990	0.2733
		8	0.4274	0.3033	0.2932
	12	2	0.3333	0.2432	0.2213
		4	0.3333	0.2733	0.2667
		8	0.3560	0.2790	0.2760
0.25	4	2	0.3820	0.3369	0.2788
		4	0.5363	0.4461	0.4373
		8	0.5931	0.5089	0.4792
	8	2	0.2537	0.1916	0.1857
		4	0.3907	0.2671	0.2402
		8	0.4316	0.3087	0.2866
	12	2	0.2379	0.1474	0.1409
		4	0.3406	0.2112	0.1971
		8	0.4175	0.2577	0.2225

Table 6.3: The database of transgenic zebrafish lines used in our experiments along with its age in hours-post-fertilization (hpf) and spatial resolution $(\Delta x, \Delta y, \Delta z)$. Every sequence was acquired at a frame-rate of 30 frames-per-second, and the period of the cardiac cycles lies in the range $1/3 \leq T \leq 1/2$.

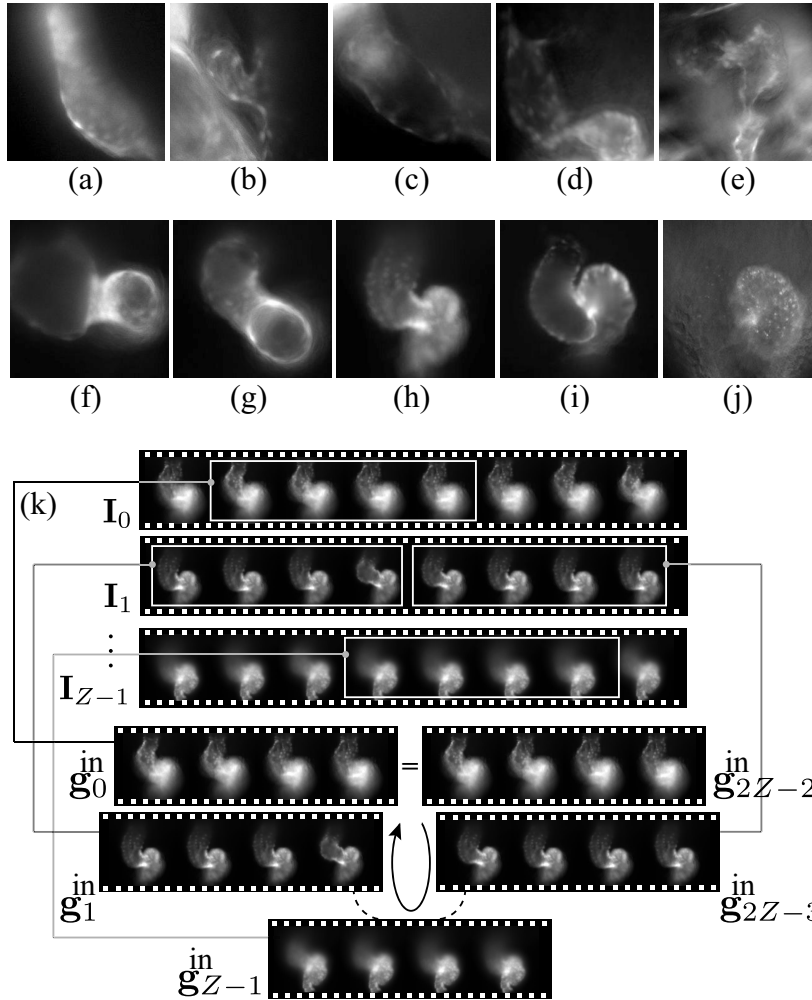|	Transgenic zebrafish	hpf	$\Delta x, \Delta y, \Delta z$ (μm)
1.	Tg(fli1a:EGFP)	27	0.8, 0.8, 5.0
2.	Tg(fli1a:EGFP)	30	0.8, 0.8, 4.0
3.	Tg(fli1a:EGFP)	57	0.8, 0.8, 4.0
4.	Tg(fli1a:EGFP)	78	1.6, 1.6, 5.3
5.	Tg(fli1a:EGFP)	96	0.8, 0.8, 5.0
6.	Tg(cmlc2:EGFP)	51	0.8, 0.8, 5.0
7.	Tg(cmlc2:EGFP)	55	0.8, 0.8, 5.0
8.	Tg(cmlc2:EGFP)	81	0.8, 0.8, 4.5
9.	Tg(cmlc2:EGFP)	100	1.6, 1.6, 4.4
10.	$Gt(desma:mCherry)^{ct122aR}$	82	0.8, 0.8, 5.0

133

Figure 6.13: (a)-(j) Examples of frames depicting the cardiac cycle in 10 different in vivo datasets used for evaluation. (k) Validation using circular registration: shorter sequences $\mathbf{g}_k^{\text{in}}$ generated from the actual measurements $\mathbf{I}_{\min(k,2Z-2-k)}$, $k = 0, \ldots, 2Z-2$, with $\mathbf{g}_{2Z-2}^{\text{in}} = \mathbf{g}_0^{\text{in}}$, are recursively synchronized to check for error accumulation.

were unknown, we implemented a circular registration validation experiment, where we recursively synchronized the sequences from first to last and then continued backward to the first sequence to quantify the synchronization error cumulated from multiple recursive synchronizations. (In practice, for 3D + time reconstruction, the registration is typically carried out starting from the central axial location, with the sequences recursively registered while proceeding towards the top and bottom positions [64], as shown in Fig. 6.7.)
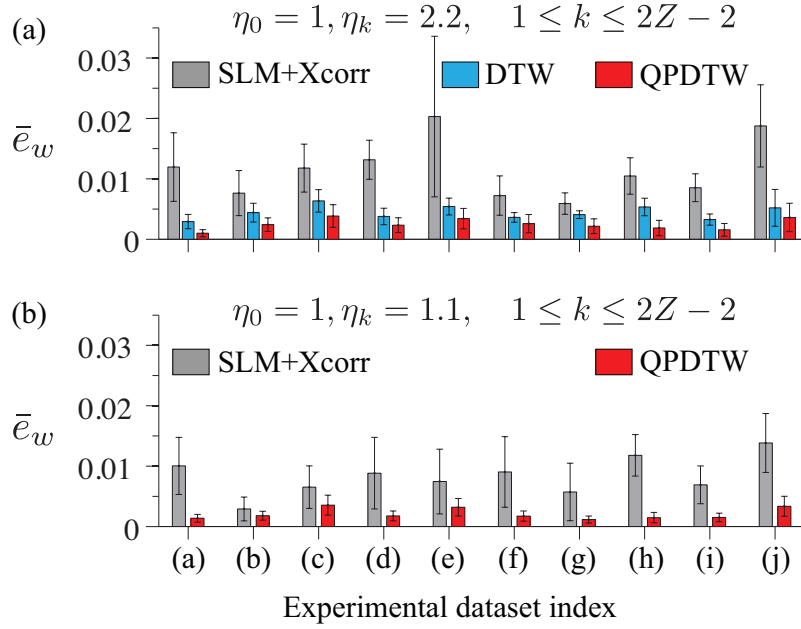
134

Figure 6.14: Experimental results for the temporal synchronization of in vivo cardiac sequences when the number of cycles in the test sequences are (a) redundant and (b) non-redundant. For all cases considered, the errors in the estimated re-warping function are least with the proposed QPDTW algorithm.

Specifically, for each evaluation experiment, we extracted $2Z - 1$ shorter sequences $\mathbf{g}_k^{\mathrm{in}}[n]$ $\in \mathbb{R}^P$, $0 \le n < N_k < N$, $0 \le k < 2Z - 1$, from the sequences $\mathbf{I}_{\min(k,2Z-2-k)}$, starting at a randomly chosen frame $n_k \in \mathbb{Z}$:

$$\mathbf{g}_k^{\mathrm{in}}[n] \stackrel{\mathrm{def}}{=} \begin{cases} \mathbf{I}_0 \left[\mathcal{W}_{\tilde{T}}(n + n_0) \right], & k = 0 \text{ or } 2Z - 2 \\ \mathbf{I}_{\min(k,2Z-2-k)} \left[n + n_k \right], & 1 \le k < 2Z - 2 \end{cases} \tag{6.56}$$

for $0 \le n < N_k$, where $\tilde{T}$ denotes the number of frames belonging to the first cycle in $\mathbf{I}_0$ and with the offsets $n_k \in \mathbb{Z}$ chosen from a discrete uniform distribution, $n_k \sim \mathcal{U}\{0, N - N_k\}$, to assign a random starting phase in $\mathbf{g}_k^{\mathrm{in}}$. We purposefully assigned $\mathbf{g}_{2Z-2}^{\mathrm{in}} = \mathbf{g}_0^{\mathrm{in}}$ so that, using the reference indices $\mathcal{R}(k) = k - 1$, for $k = 1, \ldots, 2Z - 2$, it was possible to evaluate the performance of our algorithm by comparing the recursively

estimated solution $\tilde{w}_{2Z-2}^{\text{out}}$ to the identity function $\tilde{w}_0^{\text{out}}[n] = n$, $0 \leq n < N_0$. Furthermore, we also made $\mathbf{g}_{2Z-2}^{\text{in}}$ periodic by $\tilde{T}$, so that we could also treat $\tilde{w}_{2Z-2}^{\text{out}}$ to be periodic by $\tilde{T}$, and hence ensure that whole-period offsets were not wrongfully penalized. This is illustrated in Fig. 6.13(k).

We then evaluated the performance of different algorithms by checking whether the estimated warping function for the last sequence was equivalent to identity (or full-period offsets) as captured by the following error metric:

$$\bar{e}_w \overset{\text{def}}{=} \frac{1}{(2Z-2)\tilde{T}N_0} \sum_{n=0}^{N_0-1} \min_{s \in \{0,1\}} s\tilde{T} + (-1)^s \left| \mathcal{W}_{\tilde{T}} \left(\frac{\tilde{w}_{2Z-2}^{\text{out}}[n]}{\rho} \right) - \mathcal{W}_{\tilde{T}}(n) \right|. \tag{6.57}$$

Similar to the simulations in Section 6.6.1, we assigned the first sequence $\mathbf{g}_0^{\text{in}}$ to span one cycle ($\eta_0 = 1$), and considered the number of cycles in each of the subsequent sequences $\mathbf{g}_k^{in}$ to be either $\eta_k = 2.2$ or $\eta_k = 1.1$, for $1 \leq k < 2Z - 1$. The RMS and standard deviation values of $\bar{e}_w$ observed over 25 experimental instances for the cardiac sequences depicted in the in vivo datasets in our database are shown in Fig. 6.14. While the error in the warping function for each synchronization was found to be around 1-2% of the cardiac cycle duration using SLM and cross-correlation, it was around 0.1-0.4% using DTW and QPDTW, with QPDTW having the added advantage that it needed only one cycle of the cardiac sequence for synchronization.

6.6.3 Multi-cycle Denoising: DTW vs. QPDTW

The idea of noise reduction by exploiting the redundant nature in quasi-periodic sequences was earlier presented by Bhat *et al.* [9]. The work presented therein involved extracting shorter sequences from the measured sequence and synchronizing them to a template that spans one cycle in order to finally arrive at a denoised cycle. However, since DTW is not capable of seeking *piece-wise* continuous solutions, it was necessary
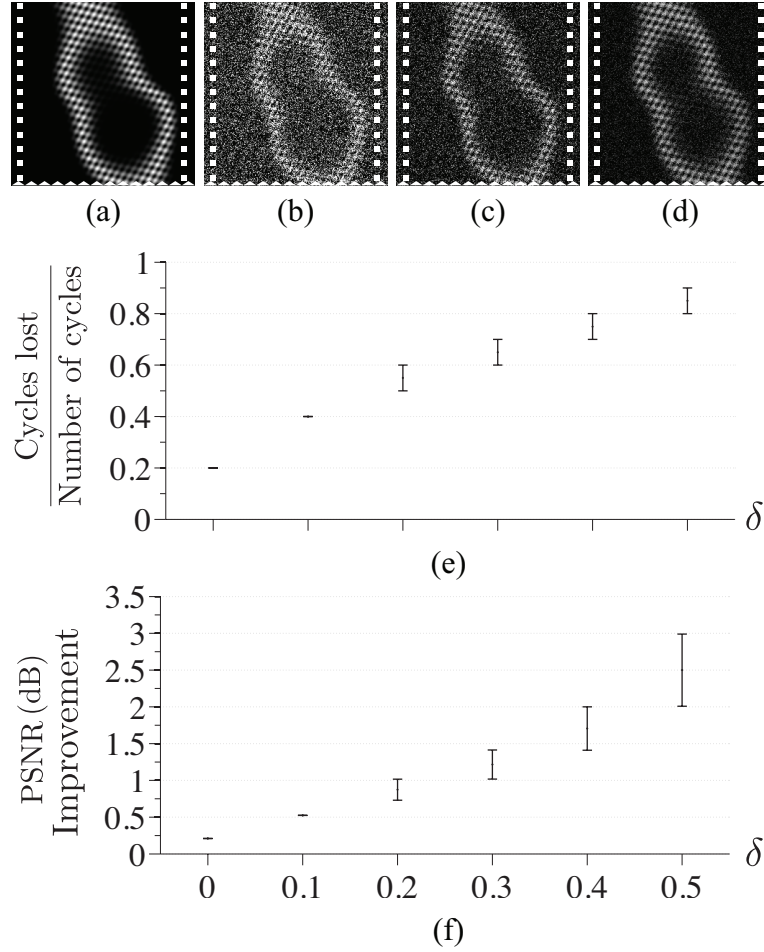
Figure 6.15: Example of frames belonging to (a) original, (b) noisy, (c) denoised sequence after cutting and multi-cycle averaging [9], and (d) using self-QPDTW. The plots shows the lower- and upper-limit of (e) the ratio of cycles lost by cutting the sequence using [9] and (f) the PSNR improvement (in dB) gained by self-QPDTW over [9], for $\eta = 10$ and varying levels of quasi-periodicity δ.

that each of the extracted sequences had at least two cycles. This subsequently meant that some data were sacrificed for the sole purpose of accommodating synchronization using DTW. Given a quasi-periodic sequence, $\mathbf{g}$, spanning multiple cycles, the procedure proposed by Bhat *et al.* [9] requires creating multiple shorter sequences defined as:

$$\mathbf{g}_0(t) = \mathbf{g}(t), \qquad\qquad 0 \leq t \leq L_0, \quad (6.58)$$

137

$$\mathbf{g}_k(t) = \mathbf{g}(t + L_0 + (k-1)(L_{k-1} - T_{\min} + \epsilon T)), \qquad (6.59)$$

for $1 \leq k \leq M_{\mathrm{cut}}$, $0 \leq t \leq L_k$, where ϵ is a small positive quantity, $\mathbf{g}_0$ is the reference template that spans $\eta_0 = 1$ cycle, and with the rest of $\mathbf{g}$ spanning a total of η cycles. The extracted sequences $\mathbf{g}_k$, $k = 1, \ldots, M_{\mathrm{cut}}$, need to be of a duration $L_k \geq L_0 \cdot T_{\max}/T_{\min} + T_{\max}$, so that $\eta_k \geq \eta_0 + 1$, for synchronization using DTW. Since $\mathbf{g}$ is of finite duration, the number of such sequences M_{cut} that can be extracted is restricted to lie in the following range:

$$M_{\mathrm{cut}} \geq \left\lfloor \frac{\eta/\alpha_{\min} - 1/\alpha_{\max} + \epsilon}{(\alpha_{\max} + \alpha_{\min})/\alpha_{\min}^2 - 1/\alpha_{\max} + \epsilon} \right\rfloor, \qquad (6.60)$$

$$M_{\mathrm{cut}} \leq \left\lfloor \frac{(\eta - 1)/\alpha_{\max} + \epsilon}{2/\alpha_{\min} - 1/\alpha_{\max} + \epsilon} \right\rfloor, \qquad (6.61)$$

which is always less than η, leading to a loss of $\eta - M_{\mathrm{cut}}$ cycles from $\mathbf{g}$. Note that this loss increases as the cycles in the sequence $\mathbf{g}$ become more quasi-periodic (that is, less regular). On the other hand, our proposed technique of self-QPDTW avoids this loss of cycles since there is no need for extracting shorter sequences, thereby making it possible to use all the cycles constructively.

To illustrate this, we used our B-spline based heart phantom to generate a sequence, $\mathbf{g}$, spanning 11 cycles with varying levels of quasi-periodicity defined by $\alpha_{\min} = 1/(1+\delta)$ and $\alpha_{\max} = 1/(1-\delta)$ [see Fig. 6.15(a)]. We next added additive white Gaussian noise (AWGN) of variance $\sigma = 0.3$ to generate a noisy sequence [see Fig. 6.15(b)]. We then proceeded to denoise the first cycle in $\mathbf{g}$ by multi-cycle averaging (and hard-thresholding) using both the procedure given in [9] (using $\epsilon = 0.1$) and self-QPDTW. An example of these denoised results for $\delta = 0.5$ is shown in Fig. 6.15(c-d). The number of cycles lost in [9] increases as the quasi-periodicity in the sequence increases, as given by the ratio of $1 - M_{\mathrm{cut}}/\eta$ in Eqs. (6.60) and (6.61), and illustrated in Fig. 6.15(e). The increase in the

peak signal-to-noise ratio (PSNR) calculated in the denoised results using self-QPDTW compared to that using [9] is shown in Fig. 6.15(f), which shows improvements of up to 3 dB for a quasi-periodicity of 50% simply because more frames from the same sequence can now be combined to reduce noise.

6.7 Discussion

6.7.1 Computation Time and Complexity

The computation of the similarity term Ψ has $\mathcal{O}(P \times N_0 \times \tilde{N}_k)$ complexity. To reduce the complexity as well as to increase robustness against noise and brightness in the sequences, we use only the high-frequency components of the coarse-scale 2D-wavelet coefficients of each frame (identical to [64]) in the input sequences to compute Ψ. For $P = 32 \times 32$, $N_0 = N_k = 100$, $\rho = 2$, our Matlab (R2013b) MEX routine takes around 1.7 seconds to compute Ψ_{ℓ_1} on a Windows 64-bit machine, equipped with a dual-core Intel Xeon 3.4-GHz CPU and 16 GB RAM. The dynamic programming approach to estimate the warping function using QPDTW has $\mathcal{O}(N_0 \times ((\tilde{N}_k - \Delta w_{\max}) \times (\Delta w_{\max} - \Delta w_{\min} + 1) + \Delta w_{\max} \times (\tilde{N}_k - \tilde{T}_{\min})))$ complexity. For $N_0 = N_k = 100$, $\rho = 2$, $\Delta w_{\min} = 1$, $\Delta w_{\max} = 3$, and $\tilde{T}_{\min} = 10$, our Matlab MEX routine for dynamic programming takes less than 5 milliseconds. The final temporal interpolation of the sequences has $\mathcal{O}(P \times N_0 \times \rho)$ complexity. For $P = 256 \times 256$, $N_0 = 100$, and $\rho = 2$, Matlab takes less than 0.5 seconds for nearest neighbor interpolation.

6.7.2 Features and Limitations

The primary advantage of QPDTW is its ability to account for both warping and wrapping operations, thereby eliminating the need for redundancies in input sequences.

This is especially significant for multi-dimensional datasets, where data size and efficient memory management bears high importance. Moreover, since we perform comparisons between quasi-periodic sequences themselves (without estimating their underlying periodic forms), an accurate calculation of the phase function or the time period of the cycles is not necessary to successfully deploy our techniques. Finally, as we use the framework of dynamic programming for all our algorithms, they are fast and have low complexity.

Our approach is limited by the assumption that the sequences are not sparsely sampled in time. This is to ensure that each sequence has at least few key frames that are close to those in the reference. Our experiments (not shown here) have indicated that the algorithm consistently gives good results as long as there are at least 10 time points representing a cardiac cycle in zebrafish embryos. This is based on the knowledge that the heart beats at the rate of 2-3 Hz in zebrafish embryos and the frequency content in each cardiac cycle is typically well represented within the first five harmonics of the base frequency, where the fifth harmonic frequency acts as the Nyquist frequency in the Nyquist-Shannon sampling theorem. This allows the temporal registration algorithms to be used as long as the frame-rate of acquisition is at least 20-30 frames-per-second, which is well within the standard configuration of acquisitions used in cardiac imaging. We emphasize that only a single non-redundant cycle is required to be acquired at this rate for temporal registration, although the acquisition of multiple cycles is conducive to applications such as frame-rate improvement and noise reduction. We also assume that the (spatial) changes between successive time points are not large enough to cause significant artifacts when the sequences are interpolated in time.

While developed for other purposes, our method bears some resemblance to algorithms previously used for phase estimation [68], cyclic motion detection [26], and gait analysis [75]. The main difference between QPDTW and these approaches designed for their respective applications remains that QPDTW avoids the need for expensive com-

putations of the time period and phase functions, owing to the relatively higher frame rates typically available in cardiac imaging.

6.8   Conclusion

We have presented a fast and efficient dynamic programming algorithm that is capable of both temporally warping and wrapping a quasi-periodic sequence to match the phase of a reference, lifting the need for redundant cycles in the former. This has significant consequences especially for the temporal registration of multiple 2D + time sequences taken at hundreds of different focal positions in order to finally allow a 3D + time analysis, common in cardiac microscopy. The non-redundant nature of the proposed algorithm allows reductions in the required data acquisition size and computational complexity by more than 50%. Moreover, this alleviates the problem of signal deterioration over time due to photo-bleaching in techniques such as fluorescence microscopy, which otherwise poses a major challenge for multi-dimensional registration during post-processing. Furthermore, the non-redundant acquisition protocol also minimizes the duration for which the samples are subjected to illumination in fluorescence microscopy, which has been shown to be favorable for the medical health of samples, which in turn allows long term imaging protocols for purposes such as time-lapse imaging. When multiple cycles are indeed available, we have also shown how these redundancies can be used constructively towards frame-rate improvement and noise reduction.

6.A   Appendix

6.A.1   Hidden Markov Model Analogy

Consider a hidden Markov model [82] (HMM) where the observed sequence is represented by the sequence $\mathbf{g}_0[n]$, $0 \leq n < N_0$, and the most probable sequence of states is given by the best warping function $\tilde{w}_1[n] \in \mathbf{S}$, $n = 0, \ldots, N_0 - 1$, $\mathbf{S} = \{0, \ldots, \tilde{N}_1 - 1\}$. Given the first n observations $\mathbf{g}_0[k]$, $k = 0, \ldots, n-1$, we use $\mathcal{P}[m, n]$ to denote the probability of the most probable sequence of states $w[i]$, $i = 0, \ldots, n$ that has a state $w[n] = m$ as its nth state. This can be formulated (up to a multiplicative constant) using the rules of conditional independence in HMM as:

$$\mathcal{P}[m, n] = p\left(\mathbf{g}_0[n]\middle|\tilde{\mathbf{g}}_1[m]\right) \max_{i \in \mathbf{S}} \sigma_{i,m} \cdot \mathcal{P}[i, n-1] \tag{6.62}$$

for $m = 0, \ldots, \tilde{N}_k - 1$, $n = 1, \ldots, N_0 - 1$, where $\sigma_{i,m}$ refers to the transition probability from state i to state m and, assuming equally probable initial states,

$$\mathcal{P}[m, 0] = p\left(\mathbf{g}_0[n]\middle|\tilde{\mathbf{g}}_1[m]\right). \tag{6.63}$$

The most probable state sequence $\tilde{w}_1$ can then be retrieved using the Viterbi algorithm [82] as:

$$\tilde{w}[N_0 - 1] = \arg\max_{i \in \mathbf{S}} \mathcal{P}\left(i, N_0 - 1\right) \tag{6.64}$$

$$\tilde{w}[n] = \arg\max_{i \in \mathbf{S}} \sigma_{i, \tilde{w}[n+1]} \cdot \mathcal{P}[i, n], \tag{6.65}$$

for $n = N_0 - 2, \ldots, 0$. In comparison to our notations, we can infer the following relations (up to an additive constant):

$$-\log \left\{ \mathcal{P}[m, n] \right\} = \mathcal{C}[m, n], \tag{6.66}$$

$$-\log \left\{ p \left(\mathbf{g}_0[n] \middle| \tilde{\mathbf{g}}_1[m] \right) \right\} = \Psi \left\{ \tilde{\mathbf{g}}_1[m], \mathbf{g}_0[n] \right\}, \tag{6.67}$$

$$-\log \left\{ \sigma_{w[n-1], w[n]} \right\} = \lambda \cdot \Gamma \left[w[n], w[n-1] \right] \cdot \mathcal{M}[w[n], w[n-1], n-1]. \tag{6.68}$$

6.A.2   B-spline Based Quasi-Periodic Heart-Tube Phantom

Our heart-tube phantom is a periodically varying structure with intensity:

$$f(x, y, z, t) = I_0 \cdot \beta^3 \left(\frac{y^2 + z^2 - d(x, t)}{w} \right) \cdot \left[1 + A \cos(S_x x) \cos(S_y y) \cos(S_z z) \right], \tag{6.69}$$

$$d(x, t) = d_0 + \sum_{m=0}^{K-1} x^m \left(a_m \sin \left(Gx \right) + b_m \sin \left(\frac{2\pi}{T} t \right) \right), \tag{6.70}$$

where I_0 denotes the magnitude of the intensity, β^3 is the cubic B-spline function [108], w is the wall thickness, d is the space- and time-dependent diameter of the tube, G, d_0, a_m, b_m are $2K$ constant parameters that determine tube geometry, and A is the amplitude of the regular spatial pattern of frequency S_x, S_y, S_z along x, y, z, respectively.

Chapter 7

Conclusion

7.1 Summary of Contributions

We have developed a set of imaging models and reconstruction tools tailored for optical microscopy. We emphasize the novelties of our proposed methods with respect to other contemporary techniques in the following paragraphs.

To model light propagation using a well-defined digital model, we have extended techniques from the area of generalized sampling and reconstruction in the signal processing community and used it in conjunction with the scalar diffraction theory [11, 38]. This was made possible since the phenomenon of light propagation between two parallel planes in a homogeneous and isotropic medium can be modeled as an analog convolution operation between the spherical waves emanating from the object plane and a filter kernel [11]. The digital model for this operation requires a discrete representation of the spherical waves at both the object and image plane. Unser *et al.* [110] had shown that an analog signal of finite energy can be optimally approximated in a shift-invariant spline space via pre-filtering, sampling, and post-filtering, which is similar to the pipeline of operations in the classical sampling theory and is yet not limited to bandlimited signals. This allowed the

Table 7.1: Overview of the methods for generalized sampling and reconstruction.

Discretization of Analog Convolution Operators (Chapter 2)	
References	*Main Contribution*
Unser *et al.* [110]	The least-squares spline approximation of analog signals via pre-filtering, sampling, and post-filtering.
Aldroubi *et al.* [3]	The least-squares reconstruction of analog signals from discrete samples recorded by non-ideal acquisition devices.
Unser [107]	The discretization of analog signal processing operators using a Hilbert space framework.
Eldar *et al.* [30]	The minimax-regret reconstruction of analog signals from discrete samples recorded by non-ideal acquisition devices.
Ramani *et al.* [83]	The estimation of the best shift-invariant space for reconstruction of analog signals from discrete samples recorded by non-ideal acquisition devices.
Chacko *et al.* [19]	The *multi-rate* discretization of analog convolution operators using a Hilbert space framework and the reconstruction of analog (*deconvolved*) signals from samples of the analog *convolved* signals recorded by non-ideal acquisition devices.

unique representation of non-bandlimited signals using a finite number of discrete samples acquired at sub-Nyquist rates. Other researchers [3, 30, 83] had later shown that such discrete samples representing the approximation of the signal in a known non-ideal shift-invariant space can be subjected to a digital filtering operation to estimate the discrete samples representing the analog signal in a different shift-invariant space that is more appropriate. The approximation of continuous signal processing operators in a Hilbert space framework was first introduced by Unser [107]. Extending this framework, we have shown that an analog convolution operation can be characterized by a multi-rate digital filtering protocol that relates the discrete samples representing the analog input and convolved signals in shift-invariant spaces with different sampling rates (see Table 7.1). Building on the purely mathematical treatment that the methodology has been given in the past, we have provided efficient implementations of our proposed techniques [16] for reproducibility and easy adaptation to other applications that involve analog convolution operators such as the computation of derivatives from discrete samples of a signal.

To solve the problem of spatially registering the anisotropically blurred volumes ac-

Table 7.2: Overview of the spatial registration methods for multi-view optical microscopy.

Spatial Registration for Multi-View Optical Microscopy (Chapter 3)					
Method	*Assumes Isotropic PSF?*	*Requires Manual Supervision?*	*Requires Data-Specific Landmarks?*	*Requires Fiducial Markers?*	*References*
Conventional intensity-based (cross-correlation)	Yes	**No**	**No**	**No**	Shaw *et al.* [90] Cogswell *et al.* [22] Heintzmann *et al.* [43] Swoger *et al.* [99, 100] Remmele *et al.* [85]
Manual-based	**No**	Yes	**No**	**No**	Heintzmann *et al.* [44]
Nuclei-based	**No**	**No**	Yes	**No**	Keller *et al.* [50]
Bead-based	**No**	**No**	**No**	Yes	Preibisch *et al.* [79] T.-Ott *et al.* [103] Krzic *et al.* [56]
PSF-based	**No**	**No**	**No**	**No**	**Chacko *et al.*** [15]

quired in multi-view optical microscopy, we have proposed an automatic PSF-aware intensity- and pyramid-based registration algorithm. Our algorithm consists of re-blurring the measured volumes with geometrically transformed forms of the PSF in order to make them comparable during the process of spatial registration. This is partly reminiscent of techniques used in multi-channel blind deconvolution techniques, where re-blurred forms of the measurements are used to determine the blurring filter kernel corresponding to each channel [93]. A wide array of techniques have been used for the spatial registration problem in multi-view microscopy. The early approaches were based on the naive assumption that the datasets have isotropic spatial resolution and used simple techniques such as cross-correlation to align one dataset to another [90, 22, 43, 100, 85]. However, such approaches generally lead to inaccuracies as they ignore the anisotropy inherent in the image formation process. Conventional moment-based registration techniques also fail for this class of problems since the anisotropic PSF shifts the optical center of mass (and other moments), leading traditional pixel-based matching methods (which would match the center of mass) to yield a biased solution. Heintzmann *et al.* [44] had presented a mostly manual registration algorithm that relies on an interactive selection of

salient points in the input volumes, which are used as an alignment aid. However, such a manual technique tends to be both laborious and inaccurate. Following a data-specific approach, Keller *et al.* [50] had used a method to automatically detect cell nuclei and treat them as landmarks for multi-view registration. Other researchers [79, 103] have proposed a different class of algorithms that can be considered automatic, which relies on fiducial markers, such as fluorescent beads, added in moderate concentration to the prepared sample, which are subsequently detected and used for registration. Although these approaches have been shown to be accurate, they require a special method of sample preparation. Moreover, the markers added can interfere with the visibility of the sample being imaged. To alleviate this problem, Krzic *et al.* [56] designed an imaging system where such fiducial markers are only used for hardware calibration, thereby averting the need to add beads along with the sample during imaging. To work around the shortcomings of these previous approaches, we have proposed an automatic and data-independent spatial registration technique that is capable of handling anisotropic PSFs and is free of fiducial markers (see Table 7.2). Furthermore, since we have employed a multi-resolution approach by using a dyadic pyramid (based on cubic B-splines) to represent the volumes at multiple scales, the algorithm first achieves a quick registration based on the large-scale features in the data, and subsequently makes changes for progressively finer details. This is advantageous with respect to both computation time and robustness against local minima, especially since computations (and convolutions during re-blurring) are in 3D.

To deconvolve the volumes acquired using multi-view optical microscopy, we have proposed a multi-view fast iterative-shrinkage-thresholding algorithm that models the imaging setup as a filter-bank structure, where each filter corresponds to a geometrically transformed of the PSF for the microscope. We have shown how such a framework can be used to jointly deconvolve and fuse the multi-view measurements. Furthermore, we have shown that the computational complexity of our proposed multi-view deconvolu-

Table 7.3: Overview of the deconvolution methods for multi-view optical microscopy.

Deconvolution for Multi-View Optical Microscopy (Chapter 4)				
Method	*Single-View Deconv. and Fusion?*	*Iterative?*	*Iteration Complexity Increases with No. of Views?*	*References*
Max. Freq. Content Retention (no explicit deconvolution)	**No**	No	-	Satzler *et al.* [88]
Weighted Frequency Avg. (no explicit deconvolution)	**No**	No	-	Swoger *et al.* [99]
Tikhonov Filtering	Yes	No	-	Shaw *et al.* [90]
Iterative Constrained Wiener, Maximum A Posterioi with Gaussian Noise & Prior	Yes	**Yes**	Yes	Swoger *et al.* [100]
Modified Richardson-Lucy	Yes	**Yes**	Yes	Remmele *et al.* [85] T.-Ott *et al.* [104]
Multi-View Richardson-Lucy	**No**	**Yes**	Yes	Preibisch *et al.* [78]
Multi-View FISTA	**No**	**Yes**	**No**	**Chacko *et al.* [17]**

tion algorithm is equivalent to its single-view counterpart. This is in contrast to previous techniques that only rely on fusing the multi-view measurements without an explicit step of deconvolution [88, 99]. Other researchers have resorted to deconvolving each of the measurements separately before applying suitable fusion algorithms [100, 85, 104]. However, recently, a multi-view extension of the Richardson-Lucy deconvolution technique (analogous to our multi-view extension of FISTA) was proposed that is capable of both deconvolving and fusing the measurements [78] (see Table 7.3).

To solve the depth-variant deconvolution problem arising due to spherical aberrations encountered during the imaging of thick samples in optical microscopy, we have modeled the imaging setup as a multi-rate filter-bank structure, where each filter corresponds to the PSF at a different focal depth in the sample. We have used such a model to propose a depth-variant form of the FISTA deconvolution technique that uses depth-dependent PSFs to reconstruct a 3D deblurred version of the imaged thick specimen. We have shown that our technique is capable of deconvolving the measurements without having to apply shift-invariant deconvolution techniques in sub-regions within the sample or rely

Table 7.4: Overview of the depth-variant deconvolution methods for optical microscopy.

Depth-Variant Deconvolution for Optical Microscopy (Chapter 5)		
Method	*Requires Deconv. in Sub-Regions?*	*References*
Expectation-Maximization	Yes	Preza *et al.* [81]
Linear Least-Squares Minimization	Yes	Maalouf *et al.* [67]
Total-Variation Minimization	Yes	Hadj *et al.* [7]
Modified Richardson-Lucy	Yes	T.-Ott *et al.* [104]
Depth-Variant FISTA	**No**	**Chacko *et al.* [18]**

on suitable fusion algorithms to alleviate blocking artifacts [81, 67, 7, 104] (see Table 7.4).

To solve the temporal registration problem of aligning cardiac sequences acquired sequentially, we have proposed a quasi-periodic variant of the DTW algorithm based on an HMM. Unlike prospective techniques that rely on external gating signals based on hardware customization [48, 101], we have proposed a retrospective technique that only relies on the information contained in the acquired sequences for non-rigid temporal registration. Our method is general enough to accommodate for quasi-periodicities in the acquired cardiac sequences as opposed to previous algorithms that assume perfect periodicity for registration [64, 35, 66]. Our method is capable of both temporally warping and wrapping an input sequence by allowing for jump discontinuities in the non-linear temporal alignment function akin to those found in wrapped phase functions. We have shown that this averts the need for redundant cycles in the acquired data, thereby reducing the computational complexity and the data to be collected by more than 50% compared to previous algorithms [65]. When redundant cycles are indeed available, we show how such redundancies can be used constructively towards frame-rate improvement and noise reduction without the need to extract sub-sequences (which potentially leads to data loss) for multi-cycle processing [9]. Furthermore, since we have used a dynamic programming framework, our algorithms have been implemented in a fast and efficient manner for multi-dimensional cardiac sequences [84] (see Table 7.5).

Table 7.5: Overview of the temporal registration methods for in vivo cardiac microscopy.

Temporal Registration for In Vivo Cardiac Microscopy (Chapter 6)						
Method	*Requires Gating Signal?*	*Assumes Perfect Periodicity?*	*Leads to Data Loss?*	*No. of Cycles Required*	*Acquired: Denoised Cycle Ratio*	*References*
Prospective*	Yes	**No**	-	-	-	Jenkins *et al.* [48] Taylor [101]
Retrospective	**No**	Yes	**No**	> 1	-	Liebling *et al.* [64] Gargesha *et al.* [35] Liu *et al.* [66]
	No	**No**	Yes	> 2	-	Liebling *et al.* [65]
	No	**No**	Yes	> 2	5 : 1	Bhat *et al.* [9]
	No	**No**	**No**	> 1	**1 : 1**	**Chacko *et al.** [14]

∗ Prospective gating techniques rely on gating signals and hardware customization to trigger the acquisition of snapshots at specific cardiac phases. Acquisition of whole cardiac cycles either require the assumption of perfect periodicity or repeated acquisitions of images at explicit intermediate phases.

7.2 Future Outlook

The series of tools described here have allowed us to model and mitigate artifacts typically encountered in optical microscopy. Future directions of work might include exploring the possibility of using multi-view microscopy to analyze dynamically changing structures such as the beating heart from different views. This would be possible by utilizing the tools developed for spatial and temporal registration described in Chapters 3 and 6, respectively, together with the multi-view deconvolution technique described in Chapter 4. In addition to in vivo cardiac microscopy, the use of the temporal registration tool could also be explored for other applications in pattern recognition such as cyclic motion detection [26] and gait analysis [75]. Similarly, the use of the multi-view spatial registration tool could also be investigated for potential applications in computer vision such as the spatial alignment of multiple images affected by camera-shake blur [119, 122] or video frames having different types of motion blur. In addition to other potential uses for optical microscopy, exploring such applications would greatly enhance the practical relevance of the techniques developed in this thesis for a much wider research community.

Bibliography

[1] D. A. Agard, Y. Hiraoka, P. Shaw, and J. W. Sedat, "Fluorescence microscopy in three dimensions," *Methods In Cell Biology*, vol. 30, pp. 353–377, 1989.

[2] I. Aizenberg and J. Astola, "Discrete generalized Fresnel functions and transforms in an arbitrary discrete basis," *IEEE Trans. Signal Process.*, vol. 54, no. 11, pp. 4261–4270, Nov. 2006.

[3] A. Aldroubi and M. Unser, "Sampling procedures in function spaces and asymptotic equivalence with shannon's sampling theory," *Numerical functional analysis and optimization*, vol. 15, no. 1-2, pp. 1–21, 1994.

[4] J. M. Batikian and M. Liebling, "Multicycle non-local means denoising of cardiac image sequences," in *IEEE 11th Intl. Symp. on Biomed. Imaging (ISBI)*, Apr 2014, pp. 1071–1074.

[5] A. Beck and M. Teboulle, "A fast iterative shrinkage-thresholding algorithm for linear inverse problems," *SIAM J. Img. Sci.*, vol. 2, no. 1, pp. 183–202, Mar. 2009.

[6] J. Bect, L. Blanc-Féraud, G. Aubert, and A. Chambolle, "A ℓ_1-unified variational framework for image restoration," in *Computer Vision - ECCV 2004*, ser. Lecture Notes in Computer Science.   Springer Berlin Heidelberg, 1-13, 2004, vol. 3024.

[7] S. Ben Hadj and L. Blanc-Féraud, "Modeling and removing depth variant blur in 3D fluorescence microscopy," in *IEEE Intl. Conf. on Acoustics, Speech and Signal Process. (ICASSP)*, 2012, pp. 689–692.

[8] M. Bertero and P. Boccacci, *Introduction to Inverse Problems in Imaging*.   IOP Publishing, 1998.

[9] S. Bhat, I. V. Larina, K. V. Larin, M. E. Dickinson, and M. Liebling, "Multiple-cardiac-cycle noise reduction in dynamic optical coherence tomography of the embryonic heart and vasculature," *Opt. Lett.*, vol. 34, no. 23, pp. 3704–3706, Dec 2009.

[10] T. Blu and M. Unser, "Quantitative Fourier analysis of approximation techniques: Part I – Interpolators and projectors," *IEEE Trans. Signal Process.*, vol. 47, no. 10, pp. 2783–2795, Oct 1999.

[11] M. Born and E. Wolf, *Principles of Optics: Electromagnetic Theory of Propagation, Interference and Diffraction of Light*, 7th ed. Cambridge University Press, 1999.

[12] R. N. Bracewell, K. Y. Chang, A. K. Jha, and Y. H. Wang, "Affine theorem for two-dimensional Fourier transform," *Electronics Lett.*, vol. 29, no. 3, 1993.

[13] C. M. Brislawn, "Classification of nonexpansive symmetric extension transforms for multirate filter banks," *App. Comp. Harm. Anal.*, vol. 3, no. 4, pp. 337–357, 1996.

[14] N. Chacko, K. G. Chan, S. Bhat, J. Ohn, and M. Liebling, "Quasi-periodic dyanamic time warping for temporal registration of cardiac signals," *IEEE Trans. Med. Imag.*, submitted.

[15] N. Chacko, K. G. Chan, and M. Liebling, "Intensity-based point-spread-function-aware registration for multi-view applications in optical microscopy," in *IEEE 12th Intl. Symp. on Biomed. Imaging (ISBI)*, April 2015, pp. 306–309.

[16] N. Chacko and M. Liebling, http://sybil.ece.ucsb.edu/gcvfft, [Online].

[17] ——, "Fast thresholded multi-channel Landweber algorithm for wavelet-regularized multi-angle deconvolution," in *Proc. SPIE*, 2013, pp. 885 819 1–10.

[18] ——, "Fast spatially variant deconvolution for optical microscopy via iterative shrinkage thresholding," in *IEEE Intl. Conf. on Acoustics, Speech and Signal Process. (ICASSP)*, May 2014, pp. 2838–2842.

[19] N. Chacko, M. Liebling, and T. Blu, "Discretization of continuous convolution operators for accurate modeling of wave propagation in digital holography," *J. Opt. Soc. Am. A*, vol. 30, no. 10, pp. 2012–2020, Oct 2013.

[20] M. Chalfie, Y. Tu, G. Euskirchen, W. W. Ward, and D. C. Prasher, "Green fluorescent protein as a marker for gene expression," *Science*, vol. 263, no. 5148, pp. 802–805, 1994.

[21] C. Chaux, P. L. Combettes, J. Pesquet, and V. R. Wajs, "A variational formulation for frame-based inverse problems," *Inverse Problems*, pp. 1495–1518, 2007.

[22] C. J. Cogswell, K. G. Larkin, and H. U. Klemm, "Fluorescence microtomography: multiangle image acquisition and 3D digital reconstruction," in *Electr. Imag.*, 1996, pp. 109–115.

[23] T. Collins, http://imagej.nih.gov/ij/images/confocal-stack.zip, [Online].

[24] A. F. Coskun, I. Sencan, T.-W. Su, and A. Ozcan, "Lensless wide-field fluorescent imaging on a chip using compressive decoding of sparse objects," *Opt. Express*, vol. 18, no. 10, pp. 10 510–10 523, May 2010.

[25] E. Cuche, P. Marquet, and C. Depeursinge, "Aperture apodization using cubic spline interpolation: application in digital holographic microscopy," *Opt. Commun.,*, vol. 182, pp. 59–69, 2000.

[26] R. Cutler and L. Davis, "Robust real-time periodic motion detection, analysis, and applications," *IEEE Trans. Pattern Analysis Mach. Intell.*, vol. 22, no. 8, pp. 781–796, Aug 2000.

[27] I. Daubechies, *Ten lectures on wavelets.* SIAM, 1992, vol. 61.

[28] I. Daubechies, M. Defrise, and C. De Mol, "An iterative thresholding algorithm for linear inverse problems with a sparsity constraint," *Communications on Pure and Applied Mathematics*, vol. 57, no. 11, pp. 1413–1457, 2004.

[29] D. L. Donoho and J. M. Johnstone, "Ideal spatial adaptation by wavelet shrinkage," *Biometrika*, vol. 81, no. 3, pp. 425–455, 1994.

[30] Y. Eldar and T. Dvorkind, "A minimum squared-error framework for generalized sampling," *IEEE Trans. Signal Process.*, vol. 54, no. 6, pp. 2155–2167, June 2006.

[31] F. O. Fahrbach, F. F. Voigt, B. Schmid, F. Helmchen, and J. Huisken, "Rapid 3D light-sheet microscopy with a tunable lens," *Opt. Express*, vol. 21, no. 18, pp. 21 010–21 026, Sep 2013.

[32] P. Ferraro, S. D. Nicola, G. Coppola, A. Finizio, D. Alfieri, and G. Pierattini, "Controlling image size as a function of distance and wavelength in Fresnel-transform reconstruction of digital holograms," *Opt. Lett.*, vol. 29, no. 8, pp. 854–856, Apr 2004.

[33] A. Fertner, "Computationally efficient methods for analysis and synthesis of real signals using FFT and IFFT," *IEEE Trans. Signal Process.*, vol. 47, no. 4, pp. 1061–1064, Apr 1999.

[34] M. A. T. Figueiredo and R. Nowak, "An EM algorithm for wavelet-based image restoration," *IEEE Trans. Image Process.*, vol. 12, no. 8, pp. 906–916, 2003.

[35] M. Gargesha, M. W. Jenkins, D. L. Wilson, and A. M. Rollins, "High temporal resolution OCT using image-based retrospective gating," *Opt. Express*, vol. 17, no. 13, pp. 10 786–10 799, Jun 2009.

[36] S. F. Gibson and F. Lanni, "Experimental test of an analytical model of aberration in an oil-immersion objective lens used in three-dimensional light microscopy," *JOSA A*, vol. 8, no. 10, pp. 1601–1613, 1991.

[37] G. H. Golub and C. F. Van Loan, *Matrix computations.* Baltimore, MD, USA: Johns Hopkins University Press, 1996.

[38] J. W. Goodman, *Introduction to Fourier Optics.* 2nd ed. New York: McGraw-Hill, 1996.

[39] J. W. Goodman and R. W. Lawrence, "Digital image formation from electronically detected holograms," *Applied Physics Letters*, vol. 11, no. 3, pp. 77–79, 1967.

[40] F. Gori, "Fresnel transform and sampling theorem," *Opt. Commun.*, vol. 39, no. 5, pp. 293–297, 1981.

[41] A. Griffa, N. Garin, and D. Sage, http://bigwww.epfl.ch/deconvolution/?p=bars, [Online].

[42] J. J. Healy and J. T. Sheridan, "Sampling and discretization of the linear canonical transform," *Signal Process.*, vol. 89, no. 4, pp. 641–648, Apr. 2009.

[43] R. Heintzmann and C. Cremer, "Axial tomographic confocal fluorescence microscopy," *J. of Microscopy*, vol. 206, no. 1, pp. 7–23, 2002.

[44] R. Heintzmann, G. Kreth, and C. Cremer, "Reconstruction of axial tomographic high resolution data from confocal fluorescence microscopy: a method for improving 3D fish images," *Analytical Cellular Pathology*, vol. 20, no. 1, pp. 7–15, 2000.

[45] B. M. Hennelly and J. T. Sheridan, "Generalizing, optimizing, and inventing numerical algorithms for the fractional Fourier, Fresnel, and linear canonical transforms," *J. Opt. Soc. Am. A*, vol. 22, no. 5, pp. 917–927, May 2005.

[46] S. Horbelt, M. Liebling, and M. Unser, "Discretization of the Radon transform and of its inverse by spline convolutions," *IEEE Trans. Med. Imag.*, vol. 21, no. 4, pp. 363–376, 2002.

[47] J. Huisken and D. Y. R. Stainier, "Selective plane illumination microscopy techniques in developmental biology," *Development*, vol. 136, no. 12, pp. 1963–1975, 2009.

[48] M. W. Jenkins, O. Q. Chughtai, A. N. Basavanhally, M. Watanabe, and A. M. Rollins, "In vivo gated 4D imaging of the embryonic heart using optical coherence tomography," *J. Biomed. Opt.*, vol. 12, no. 3, pp. 030 505 (1–3), 2007.

[49] V. Katkovnik, A. Migukin, and J. Astola, "Backward discrete wave field propagation modeling as an inverse problem: toward perfect reconstruction of wave field distributions," *Appl. Opt.*, vol. 48, no. 18, pp. 3407–3423, Jun 2009.

[50] P. J. Keller, A. D. Schmidt, J. Wittbrodt, and E. H. K. Stelzer, "Reconstruction of zebrafish early embryonic development by scanned light sheet microscopy," *Science*, vol. 322, no. 5904, pp. 1065–1069, 2008.

[51] D. P. Kelly and D. Claus, "Filtering role of the sensor pixel in Fourier and Fresnel digital holography," *Appl. Opt.*, vol. 52, no. 1, pp. A336–A345, Jan 2013.

[52] H. Kirshner, F. Aguet, D. Sage, and M. Unser, "3-D PSF fitting for fluorescence microscopy: Implementation and localization application," *J. of Microscopy*, vol. 249, no. 1, pp. 13–25, Jan 2013.

[53] H. Kirshner, D. Sage, and M. Unser, "3D PSF models for fluorescence microscopy in ImageJ," in *Proc. of the 12 Intl. Conf. on Methods and Applications of Fluorescence Spectroscopy, Imaging and Probes, 154*, 2011.

[54] T. M. Kreis, M. Adams, and W. P. O. Jueptner, "Methods of digital holography: a comparison," *Proc. SPIE*, vol. 3098, pp. 224–233, 1997.

[55] E. Kreyszig, *Introductory functional analysis with applications.* New York: Wiley, 1989, vol. 81.

[56] U. Krzic, S. Gunther, T. E. Saunders, S. J. Streichan, and L. Hufnagel, "Multiview light-sheet microscope for rapid *in toto* imaging," *Nature Methods*, vol. 9, no. 7, pp. 730–733, 2012.

[57] L. Landweber, "An iteration formula for Fredholm integral equations of the first kind," *American Journal of Mathematics*, vol. 73, no. 3, pp. 615–624, 1951.

[58] K. V. Larin, I. V. Larina, M. Liebling, and M. E. Dickinson, "Live imaging of early developmental processes in mammalian embryos with optical coherence tomography," *J. Innovative Optical Health Sciences*, vol. 2, no. 3, pp. 253–259, Sep 2009.

[59] I. V. Larina, K. V. Larin, M. E. Dickinson, and M. Liebling, "Sequential turning acquisition and reconstruction (STAR) method for four-dimensional imaging of cyclically moving structures," *Biomed. Opt. Express*, vol. 3, no. 3, pp. 650–660, Mar 2012.

[60] C. A. Laury-Micoulaut, "The n-th centered moment of a multiple convolution and its applications to an intercloud gas model," *Astronomy and Astrophysics*, vol. 51, pp. 343–346, 1976.

[61] J. W. Lichtman and J.-A. Conchello, "Fluorescence microscopy," *Nature methods*, vol. 2, no. 12, pp. 910–919, 2005.

[62] M. Liebling, "Fresnelab: Sparse representations of digital holograms," *Proc. SPIE*, vol. 8138, 2011.

[63] M. Liebling, T. Blu, and M. Unser, "Fresnelets: new multiresolution wavelet bases for digital holography," *IEEE Trans. Image Process.*, vol. 12, no. 1, pp. 29–43, Jan 2003.

155

[64] M. Liebling, A. S. Forouhar, M. Gharib, S. E. Fraser, and M. E. Dickinson, "Four-dimensional cardiac imaging in living embryos via postacquisition synchronization of nongated slice sequences," *J. Biomed. Opt.*, vol. 10, no. 5, pp. 054 001 (1–10), 2005.

[65] M. Liebling, J. Vermot, A. Forouhar, M. Gharib, M. Dickinson, and S. Fraser, "Nonuniform temporal alignment of slice sequences for four-dimensional imaging of cyclically deforming embryonic structures," in *IEEE 3rd Intl. Symp. Biomed. Imaging (ISBI)*, Arlington, VA, USA, Apr 6–9, 2006, pp. 1156–1159.

[66] A. Liu, R. Wang, K. L. Thornburg, and S. Rugonyi, "Efficient postacquisition synchronization of 4-D nongated cardiac images obtained from optical coherence tomography: application to 4-D reconstruction of the chick embryonic heart," *J. Biomed. Opt.*, vol. 14, no. 4, pp. 044 020 (1–11), 2009.

[67] E. Maalouf, B. Colicchio, and A. Dieterlen, "Fast deconvolution with non-invariant PSF for 3-D fluorescence microscopy," in *Proc. SPIE*, vol. 7000, 2008, pp. 70 001K 1–8.

[68] Y. Makihara, M. Aqmar, N. T. Trung, H. Nagahara, R. Sagawa, Y. Mukaigawa, and Y. Yagi, "Phase estimation of a single quasi-periodic signal," *IEEE Trans. Signal Process.*, vol. 62, no. 8, pp. 2066–2079, Apr 2014.

[69] M. M. Marim, M. Atlan, E. Angelini, and J.-C. Olivo-Marin, "Compressed sensing with off-axis frequency-shifting holography," *Opt. Lett.*, vol. 35, no. 6, pp. 871–873, Mar 2010.

[70] D. W. Marquardt, "An algorithm for least-squares estimation of nonlinear parameters," *SIAM J. on App. Math.*, vol. 11, no. 2, pp. 431–441, 1963.

[71] D. Mas, "Fast algorithms for free-space diffraction patterns calculation," *Opt. Commun.*, vol. 164, no. 4-6, pp. 233–245, 1999.

[72] K. Matsushima and T. Shimobaba, "Band-limited angular spectrum method for numerical simulation of free-space propagation in far and near fields," *Opt. Express*, vol. 17, no. 22, pp. 19 662–19 673, Oct 2009.

[73] D. Mendlovic, Z. Zalevsky, and N. Konforti, "Computation considerations and fast algorithms for calculating the diffraction integral," *J. Modern Optics*, vol. 44, pp. 407–414, Feb. 1997.

[74] O. Michailovich and A. Tannenbaum, "Blind deconvolution of medical ultrasound images: A parametric inverse filtering approach," *IEEE Trans. Image Process.*, vol. 16, no. 12, pp. 3005–3019, 2007.

[75] A. Mori, Y. Makihara, and Y. Yagi, "Gait recognition using period-based phase synchronization for low frame-rate videos," in *20th Intl. Conf. on Pattern Recognition (ICPR)*, Aug 2010, pp. 2194–2197.

[76] C. Myers, L. Rabiner, and A. E. Rosenberg, "Performance tradeoffs in dynamic time warping algorithms for isolated word recognition," *IEEE Trans. Acoust., Speech, Signal Process.*, vol. 28, no. 6, pp. 623–635, 1980.

[77] L. Onural, "Sampling of the diffraction field," *Appl. Opt.*, vol. 39, no. 32, pp. 5929–5935, Nov 2000.

[78] S. Preibisch, F. Amat, E. Stamataki, M. Sarov, R. H. Singer, E. Myers, and P. Tomancak, "Efficient bayesian-based multiview deconvolution," *Nature methods*, vol. 11, no. 6, pp. 645–648, 2014.

[79] S. Preibisch, S. Saalfeld, J. Schindelin, and P. Tomancak, "Software for bead-based registration of selective plane illumination microscopy data," *Nature Methods*, vol. 7, no. 6, pp. 418–419, 2010.

[80] W. H. Press, S. A. Teukolsky, W. T. Vetterling, and B. P. Flannery, *Numerical recipes in C (2nd ed.): the art of scientific computing*. New York, NY, USA: Cambridge University Press, 1992.

[81] C. Preza and J. Conchello, "Depth-variant maximum-likelihood restoration for three-dimensional fluorescence microscopy," *J. Opt. Soc. Am. A*, vol. 21, no. 9, pp. 1593–1601, Sep 2004.

[82] L. Rabiner, "A tutorial on hidden Markov models and selected applications in speech recognition," *Proc. of the IEEE*, vol. 77, no. 2, pp. 257–286, Feb 1989.

[83] S. Ramani, D. V. De Ville, T. Blu, and M. Unser, "Nonideal sampling and regularization theory," *Signal Processing, IEEE Transactions on*, vol. 56, no. 3, pp. 1055–1070, 2008.

[84] C. Ramspacher, E. Steed, F. Boselli, R. Ferreira, N. Faggianelli, S. Roth, C. Spiegelhalter, N. Messaddeq, L. Trinh, M. Liebling, N. Chacko, F. Tessadori, J. Bakkers, J. Laporte, K. Hnia, and J. Vermot, "Developmental alterations in heart biomechanics and skeletal muscle function in desmin mutants suggest an early pathological root for desminopathies," *Cell Reports*, vol. 11, no. 10, pp. 1564 – 1576, 2015.

[85] S. Remmele, B. Oehm, F. Staier, H. Eipel, C. Cremer, and J. Hesser, "Reconstruction of high-resolution fluorescence microscopy images based on axial tomography," in *SPIE Medical Imaging*, 2011.

[86] Y. Rivenson, A. Stern, and B. Javidi, "Compressive fresnel holography," *J. Display Technol.*, vol. 6, no. 10, pp. 506–509, Oct 2010.

[87] P. Sarder and A. Nehorai, "Deconvolution methods for 3-D fluorescence microscopy images," *IEEE Signal Process. Magazine*, vol. 23, pp. 32–45, 2006.

[88] K. Sätzler and R. Eils, "Resolution improvement by 3-D reconstructions from tilted views in axial tomography and confocal theta microscopy," *Bioimaging*, vol. 5, no. 4, pp. 171–182, 1997.

[89] C. E. Shannon, "Communication in the presence of noise," *Proc. of the IRE*, vol. 37, no. 1, pp. 10–21, Jan 1949.

[90] P. J. Shaw, D. A. Agard, Y. Hiraoka, and J. W. Sedat, "Tilted view reconstruction in optical microscopy. Three-dimensional reconstruction of Drosophila melanogaster embryo nuclei," *Biophysical J.*, vol. 55, no. 1, pp. 101–110, 1989.

[91] J.-B. Sibarita, "Deconvolution microscopy," in *Microscopy Techniques*, ser. Advances in Biochemical Engineering, J. Rietdorf, Ed. Springer Berlin Heidelberg, 201-243, 2005, vol. 95.

[92] J. Snyman, *Practical mathematical optimization: an introduction to basic optimization theory and classical and new gradient-based algorithms.* Springer Science & Business Media, 2005, vol. 97.

[93] F. Šroubek and J. Flusser, "Multichannel blind iterative image restoration," *Image Processing, IEEE Transactions on*, vol. 12, no. 9, pp. 1094–1106, 2003.

[94] J. Starck, M. K. Nguyen, and F. Murtagh, "Wavelets and curvelets for image deconvolution: a combined approach," *Signal Process.*, vol. 83, no. 10, pp. 2279–2283, 2003.

[95] J. L. Starck, E. Pantin, and F. Murtagh, "Deconvolution in astronomy: A review," *Publications of the Astronomical Society of the Pacific*, vol. 114, no. 800, pp. 1051–1069, 2002.

[96] R. Stellingwerf, "Period determination using phase dispersion minimization," *Astrophys.J.*, vol. 224, pp. 953–960, 1978.

[97] A. Stern and B. Javidi, "Analysis of practical sampling and reconstruction from Fresnel fields," *Opt. Eng.*, vol. 43, pp. 239–250, 2004.

[98] ——, "Sampling in the light of Wigner distribution," *J. Opt. Soc. Am. A*, vol. 21, no. 3, pp. 360–366, Mar 2004.

[99] J. Swoger, J. Huisken, and E. H. K. Stelzer, "Multiple imaging axis microscopy improves resolution for thick-sample applications," *Opt. Lett.*, vol. 28, no. 18, pp. 1654–1656, 2003.

[100] J. Swoger, P. Verveer, K. Greger, J. Huisken, and E. H. K. Stelzer, "Multi-view image fusion improves resolution in three-dimensional microscopy," *Opt. Express*, vol. 15, no. 13, pp. 8029–8042, 2007.

[101] J. M. Taylor, "Optically gated beating-heart imaging," *Frontiers in Physiology*, vol. 5, no. 481, 2014.

[102] J. M. Taylor, C. D. Saunter, G. D. Love, J. M. Girkin, D. J. Henderson, and B. Chaudhry, "Real-time optical gating for three-dimensional beating heart imaging," *J. Biomed. Opt.*, vol. 16, no. 11, pp. 116 021 (1–8), 2011.

[103] M. Temerinac-Ott, M. Keuper, and H. Burkhardt, "Evaluation of a new point clouds registration method based on group averaging features," in *20th Int. Conf. on Pattern Recognition (ICPR)*, Aug. 2010, pp. 2452–2455.

[104] M. Temerinac-Ott, O. Ronneberger, P. Ochs, W. Driever, T. Brox, and H. Burkhardt, "Multiview deblurring for 3-D images from light-sheet-based fluorescence microscopy," *IEEE Trans. Image Process.*, vol. 21, no. 4, pp. 1863–1873, 2012.

[105] P. Thévenaz, U. E. Ruttimann, and M. Unser, "A pyramid approach to subpixel registration based on intensity," *IEEE Trans. Image Process.*, vol. 7, no. 1, pp. 27–41, Jan. 1998.

[106] V. Trivedi, T. V. Truong, L. A. Trinh, D. B. Holland, M. Liebling, and S. E. Fraser, "Dynamic structure and protein expression of the live embryonic heart captured by 2-photon light sheet microscopy and retrospective registration," *Biomed. Opt. Express*, vol. 6, no. 6, pp. 2056–2066, Jun 2015.

[107] M. Unser, "A general Hilbert space framework for the discretization of continuous signal process. operators," *Proc. SPIE,*, vol. 2569, pp. 51–61, 1995.

[108] ——, "Splines: a perfect fit for signal and image processing," *IEEE Signal Process. Mag.*, vol. 16, no. 6, pp. 22–38, Nov 1999.

[109] ——, "Sampling-50 years after Shannon," *Proc. IEEE*, vol. 88, no. 4, pp. 569 –587, Apr 2000.

[110] M. Unser, A. Aldroubi, and M. Eden, "Polynomial spline signal approximations: filter design and asymptotic equivalence with shannon's sampling theorem," *Information Theory, IEEE Transactions on*, vol. 38, no. 1, pp. 95–103, 1992.

[111] P. J. Verveer and T. M. Jovin, "Improved restoration from multiple images of a single object: Application to fluorescence microscopy," *Appl. Opt.*, vol. 37, no. 26, pp. 6240–6246, 1998.

[112] T. D. Visser, J. L. Oud, and G. J. Brakenhoff, "Refractive index and axial distance measurements in 3-D microscopy," *Optik*, vol. 90, no. 1, pp. 17–19, 1992.

[113] C. Vonesch, F. Aguet, J.-L. Vonesch, and M. Unser, "The colored revolution of bioimaging," *IEEE Signal Process. Magazine*, vol. 23, no. 3, pp. 20–31, 2006.

[114] C. Vonesch and M. Unser, "A fast thresholded Landweber algorithm for wavelet-regularized multidimensional deconvolution," *IEEE Trans. Image Process.*, vol. 17, no. 4, pp. 539–549, 2008.

[115] ——, "A fast multilevel algorithm for wavelet-regularized image restoration," *IEEE Trans. Image Process.*, vol. 18, no. 3, pp. 509–523, 2009.

[116] Z. Wang, A. Bovik, H. Sheikh, and E. Simoncelli, "Image quality assessment: from error visibility to structural similarity," *IEEE Trans. Image Process.*, vol. 13, no. 4, pp. 600–612, Apr 2004.

[117] T. Wilson, "Confocal microscopy," *Academic Press: London, etc*, vol. 426, pp. 1–64, 1990.

[118] L. P. Yaroslavskii and N. S. Merzlyakov, *Methods of Digital Holography.* Consultants Bureau, New York, 1980.

[119] L. Yuan, J. Sun, L. Quan, and H. Shum, "Image deblurring with blurred/noisy image pairs," in *SIGGRAPH '07, ACM*, 2007.

[120] B. Zhang, J. Zerubia, and J.-C. Olivo-Marin, "Gaussian approximations of fluorescence microscope point-spread function models," *Appl. Opt.*, vol. 46, no. 10, pp. 1819–1829, Apr 2007.

[121] F. Zhang, I. Yamaguchi, and L. P. Yaroslavsky, "Algorithm for reconstruction of digital holograms with adjustable magnification," *Opt. Lett.*, vol. 29, no. 14, pp. 1668–1670, Jul 2004.

[122] H. Zhang and L. Carin, "Multi-shot imaging: Joint alignment, deblurring, and resolution-enhancement," in *IEEE Conf. on Computer Vision and Pattern Recognition (CVPR)*, 2014, pp. 2925–2932.